TUDelft

Delft University of Technology

Modeling, design and optimization of flapping wings for efficient hovering flighth

Wang, Qi

DOI
10.4233/uuid:e6fc3865-531f-4ea9-aeff-e2ef923ae36f

Publication date
2017

Document Version
Final published version

Important note
To cite this publication, please use the final published version (if applicable).
Please check the document version above.

MODELING, DESIGN AND OPTIMIZATION OF FLAPPING WINGS FOR EFFICIENT HOVERING FLIGHT

Qi WANG

Modeling, Design and Optimization of Flapping Wings for Efficient Hovering Flight

Proefschrift

ter verkrijging van de graad van doctor
aan de Technische Universiteit Delft,
op gezag van de Rector Magnificus prof. ir. K.C.A.M. Luyben,
voorzitter van het College voor Promoties,
in het openbaar te verdedigen op maandag 26 juni 2017 om 15:00 uur

door

Qi WANG

Master of Engineering,
Northwestern Polytechnical University, Xi'an, China,
geboren te Anhui, China.

Dit proefschrift is goedgekeurd door de

promotor: Prof. dr. ir. F. van Keulen
copromotor: Dr. ir. J. F. L. Goosen

Samenstelling promotiecommissie:

Rector Magnificus	voorzitter
Prof. dr. ir. F. van Keulen	Technische Universiteit Delft
Dr. ir. J. F. L. Goosen	Technische Universiteit Delft

Onafhankelijke leden:

Prof. dr. ir. J. L. Herder	Technische Universiteit Delft
Prof. dr. S. Hickel	Technische Universiteit Delft
Prof. dr. A. J. Preumont	Université libre de Bruxelles
Prof. dr. F. O. Lehmann	Universität Rockstock
Dr. F. T. Muijres	Wageningen University & Research

Author email: wangqitop@hotmail.com

An electronic version of this dissertation is available at
http://repository.tudelft.nl/.

to my parents, my wife and two lovely boys
献给我的父母、妻子和两个可爱的儿子

SUMMARY

Inspired by insect flights, flapping wing micro air vehicles (FWMAVs) keep attracting attention from the scientific community. One of the design objectives is to reproduce the high power efficiency of insect flight. However, there is no clear answer yet to the question of how to design flapping wings and their kinematics for power-efficient hovering flight. In this thesis, we aim to answer this research question from the perspectives of wing modeling, design and optimization.

Quasi-steady aerodynamic models play an important role in evaluating aerodynamic performance and designing and optimizing flapping wings. In Chapter 2, we present a predictive quasi-steady model by including four aerodynamic loading terms. The loads result from the wing's translation, rotation, their coupling as well as the added-mass effect. The necessity of including all four of these terms in a quasi-steady model to predict both the aerodynamic force and torque is demonstrated. Validations indicate a good accuracy of predicting the center of pressure, the aerodynamic loads and the passive pitching motion for various Reynolds numbers. Moreover, compared to the existing quasi-steady models, the proposed model does not rely on any empirical parameters and, thus, is more predictive, which enables application to the shape and kinematics optimization of flapping wings.

For flapping wings with passive pitching motion, a shift in the pitching axis location alters the aerodynamic loads, which in turn change the passive pitching motion and the flight efficiency. Therefore, in Chapter 3, we investigate the optimal pitching axis location for flapping wings to maximize the power efficiency during hovering flight. Optimization results show that the optimal pitching axis is located between the leading edge and the mid-chord line, which shows a close resemblance to insect wings. An optimal pitching axis can save up to 33% of power during hovering flight when compared to optimized traditional wings used by most of the flapping wing micro air vehicles. Traditional wings typically use the straight leading edge as the pitching axis. In addition, the optimized pitching axis enables the drive system to recycle more energy during the deceleration phases as compared to their counterparts. This observation underlines the particular importance of the wing pitching axis location for energy-efficient FWMAVs when using kinetic energy recovery drive systems.

The presence of wing twist can alter the aerodynamic performance and power efficiency of flapping wings by changing the angle of attack. In order to study the optimal twist of flapping wings for hovering flight, we propose a computationally efficient fluid-structure interaction (FSI) model in Chapter 4. The model uses an analytical twist model and the quasi-steady aerodynamic model introduced in Chapter 2 for the structural and aerodynamic analysis, respectively. Based on the FSI model, we optimize the twist of a rectangular wing by minimizing the power consumption during hovering flight. The power efficiency of the optimized twistable wings is compared with corresponding optimized rigid wings. It is shown that the optimized twistable wings can not dramatically

outperform the optimized rigid wings in terms of power efficiency, unless the pitching amplitude at the wing root is limited. When this amplitude decreases, the optimized twistable wings can always maintain high power efficiency by introducing certain twist while the optimized rigid wings need more power for hovering.

Considering the high impact of the root stiffness on flapping kinematics and power consumption, we present an active hinge design which uses electrostatic force to change the hinge stiffness in Chapter 5. The hinge is realized by stacking three conducting spring steel layers which are separated by dielectric Mylar films. The theoretical model shows that the stacked layers can switch from slipping with respect to each other to sticking together when the resultant electrostatic force between layers, which can be controlled by the applied voltage, is above a threshold value. The switch from slipping to sticking will result in a dramatic increase of the hinge stiffness (about 9×). Therefore, a short duration of the sticking can still lead to a considerable change in the passive pitching motion. Experimental results successfully show the decrease of the pitching amplitude with the increase of the applied voltage. Flight control based on the electrostatic force can be very power-efficient since there is ideally no power consumption due to the control operations.

In Chapter 6, we retrospect and discuss the most important aspects related to the modeling, design and optimization of flapping wings for efficient hovering flight. In Chapter 7, the overall conclusions are drawn and recommendations for further study are provided.

SAMENVATTING

Geïnspireerd door het vliegen van insecten blijft de wetenschappelijke gemeenschap zich verdiepen in de ontwikkeling van micro-luchtvaartuigen met flappende vleugels (FWMAV). Een van de doelen is het reproduceren van de energie efficiëntie van deze insecten. Tot nu toe is er geen antwoord op de vraag: "Hoe ontwerpen we flappende vleugels voor efficiënt vliegen en zweven?" In dit proefschrift richten we ons op het beantwoorden van deze vraag vanuit het perspectief van vleugelmodellering, -ontwerp en -optimalisatie.

Tijdens het ontwerp en optimaliseren van flappende vleugels spelen quasi-statische aerodynamische modellen een belangrijke rol. In Hoofdstuk 2 presenteren we een voorspellend, quasi-statisch model op basis van vier aerodynamische belastingen. Deze belastingen worden veroorzaakt door verschillende aerodynamische componenten van de vleugel, te weten: translatie, rotatie, hun koppeling en het toegevoegde massa effect. We demonstreren de noodzaak voor het introduceren van elk van deze vier termen om een juiste voorspelling te verkrijgen van de aerodynamische krachten en momenten. Validatie toont een goede nauwkeurigheid van de voorspellingen van het drukpunt, de aerodynamische belasting, en de passieve vleugelrotatiebeweging voor verschillende Reynoldsgetallen. Bovendien, in bestaande quasi-statische modellen, is het voorgestelde model niet afhankelijk van enige empirische parameters. Dit maakt vergelijking met het model meer voorspellend en geschikt voor de optimalisatie van vorm en kinematica van flappende vleugels.

Voor flappende vleugels met een passieve rotatie, brengt een verschuiving van de locatie van de rotatie-as een verandering teweeg van de aerodynamische belasting. Dit resulteert vervolgens in een verandering van de passieve vleugel rotatie, en daarmee de efficiëntie van het vliegen. In Hoofdstuk 3 onderzoeken we de optimale locatie van de rotatie-as voor het minimaliseren van het energieverbruik tijdens het zweven (stil hangen in de lucht). De optimalisatie toont een optimale locatie voor de rotatie-as tussen de voorrand en het midden van de koorde, wat grote overeenkomst vertoont met de vleugels van insecten. In vergelijking met traditionele vleugels in FWMAVs gebruiken geoptimaliseerde vleugels 33% minder energie tijdens het vliegen. In traditionele vleugelontwerpen wordt veelal een rechte vleugel-voorrand gebruikt als rotatie-as terwijl vleugels met een geoptimaliseerde rotatie-as meer mogelijkheden, terwijl hebben voor het hergebruiken van energie tijdens de decceleratie fase van de vleugelbeweging. Deze constatering benadrukt het belang van de rotatie-as in het ontwerp van FWMAVs waarin gebruik gemaakt wordt van kinetische aandrijfsystemen met de mogelijkheid van het terugwinnen van energie.

De aanwezigheid van vleugelverdraaiing verandert de lokale invalshoek, wat een effect heeft op de aerodynamische prestatie en het verbruikte vermogen. In Hoofdstuk 4 presenteren we een efficiënt vloeistof-structuur interactie model voor de optimalisatie van de torsie in flappende vleugels. Het model maakt gebruik van een analytisch tor-

siemodel in combinatie met het quasi-statische aerodynamische model zoals gepresenteerd in Hoofdstuk 2. Met behulp van dit model minimaliseren we het energieverbruik van een rechthoekige vleugel door een optimale torsie te zoeken. Het resulterende vermogen wordt vergeleken met dat van een vergelijkbare stijve vleugel. De geoptimaliseerde torsie resulteert niet in een dramatische verbetering van de efficiëntie ten opzichte van een stijve vleugel, behalve als de maximale rotatiehoek aan de vleugelbasis wordt beperkt. Zodra deze hoek afneemt, zullen geoptimaliseerde, flexibele vleugels altijd een hogere energie-efficiëntie behalen.

In Hoofdstuk 5 presenteren we een actief scharnier op basis van elektrostatische belastingen, welke in staat is de rotatiestijfheid van de basis van de vleugel actief te veranderen. Dit is geïnspireerd op de grote invloed die de rotatiestijfheid van de vleugelbasis heeft op de kinematica en energie-efficiëntie. Het scharnier bestaat uit drie gestapelde lagen geleidend verenstaal die gescheiden zijn door een diëlektricum van Mylar. Een theoretisch model toont dat deze lagen zullen glijden of "plakken", afhankelijk van de elektrische potentiaal die aangebracht wordt op het scharnier. Door actieve regeling van het voltage is het mogelijk te wisselen tussen glijden en "plakken", hetgeen resulteert in een significante toename van de stijfheid (ongeveer negen maal). In een relatief korte periode kan het aanpassen van de stijfheid resulteren in een significante verandering van de passieve vleugelrotatie. Deze resultaten zijn bevestigd in experimenten waarbij een afname in de amplitude van de rotatiebeweging is waargenomen als gevolg van een toename in het aangebrachte voltage. Het stabiliseren en sturen van het vliegen op basis van elektrostatische belastingen maakt energie efficiënt vliegen mogelijk, aangezien er idealiter geen vermogen wordt verbruikt tijdens de aansturing.

In hoofdstuk 6 blikken we terug op het onderzoek en bespreken we de belangrijkste aspecten met betrekking tot de modelvorming, ontwerp en optimalisatie van flappende vleugels voor energiezuinig zweven. Tenslotte worden in Hoofdstuk 7 de conclusies en aanbevelingen gepresenteerd voor toekomstig onderzoek.

前 言

受到昆虫飞行的启发，扑翼飞行器正受到科学界越来越多的关注。对于扑翼飞行器的设计，其目标之一是如何实现类似昆虫的低能耗飞行。但是，目前尚不清楚如何设计扑翼及其运动方式使其在悬停时实现这一目标。本文将从悬停时扑翼的建模、设计以及优化等角度来研究这一问题。

准定常气动模型在计算扑翼的气动性能和对扑翼的设计优化中发挥着重要的作用。第二章提出了一个不依赖经验参数的准定常气动模型。该模型把扑翼在悬停时所受总气动载荷分解成四个部分。其分别来源于翅膀的拍动、俯仰、二者的耦合以及附加质量效应。验证算例表明该模型可以准确地计算在不同雷诺数下气动载荷和压心以及模拟扑翼的被动俯仰运动。此外，与已有准定常模型相比该模型不依赖于经验数据。因此，其可被广泛地应用于扑翼形状及其运动方式的优化设计。

在气动和惯性载荷的作用下，扑翼会发生被动的俯仰运动。俯仰转动轴的移动可以显著地改变气动载荷，进而带来俯仰运动自身和悬停效率的改变。因此，第三章着重研究了能使悬停时平均功耗最小化的俯仰转动轴的位置。优化结果表明俯仰转动轴的最佳位置位于扑翼前缘和中线之间。而传统的扑翼一般具有笔直的前缘并且以此为俯仰转动轴。基于最优的运动方式，具有最佳俯仰转动轴的扑翼可以比传统扑翼在悬停时节省33%的能耗。对于具有动能回收能力的扑翼系统，优化俯仰转动轴的位置还可以增加系统回收的能量。因此，在设计该类扑翼飞行器时应当考虑扑翼俯仰转动轴的位置以使其动能回收系统充分发挥作用。

扑翼沿展向的扭转会改变其攻角，进而影响其气动性能和悬停功耗。为了能够优化扑翼在悬停时的扭转方式，第四章首先提出了一种高效的流固耦合模型。与传统基于计算流体、结构力学的流固耦合模型的高昂计算代价相比，该模型可以在数分钟内完成对可扭转扑翼的整个运动模拟。该模型以解析的方式描述扑翼的扭转并对其进行结构分析，同时利用在第二章提出的准定常模型进行气动分析。基于该模型，本章对一个矩形扑翼的扭转以在悬停时平均功耗最小为目标进行了优化，并且与经过优化的刚性扑翼进行了对比。结果显示可扭转扑翼在功耗方面并不存在明显的优势。但是，如果减小翼根俯仰运动的幅度，刚性扑翼则需要更多的能量来保持悬停状态。而通过引入一定的扭转可扭转扑翼能够始终维持其效率。这也为昆虫如何利用不同柔性的翅膀实现高效飞行提供了一种解释。

考虑到翼根的扭转刚度对扑翼的俯仰运动以及悬停效率的影响，第五章介绍了一种刚度可调的翼根铰链设计。该铰链通过堆叠三层由麦拉膜包裹着的弹簧钢薄片形成类似于三明治的结构。该设计可以利用静电吸附载荷来改变铰链在弯曲时的刚度。随着在静电载荷的变化，扑翼在俯仰时，铰链的层与层之间可以处在相对滑动或者相对静止状态。理论分析显示当加载电压超过一定阈值时，其状态可以从相对滑动变为相对静止。这一切换导致铰链的刚度大幅增加(9×)，进而改变扑翼的俯仰运动。同时，在实验中也观察到扑翼俯仰运动的幅度随着电压的增加而减小。这验证了基于静电吸附作用的扑翼飞行控制技术的可行性。考虑静电作用在理想情况下不会带来能量损耗，因此它可以成为一种低能耗的控制方式。

本文在第六章回顾并讨论了以提高悬停效率为目标的扑翼的建模、设计以及优化。在最后一章对本文得到的结论进行了概括并为将来的研究给出了建议。

CONTENTS

NOMENCLATURE

AR	aspect ratio
c	chord length
$\bar{c}$	average chord length
$\hat{d}$	local-chord-normalized distance from leading edge to pitching axis
$\hat{d}_\mathrm{r}$	$\hat{d}$ at wing root
$\hat{d}_\mathrm{t}$	$\hat{d}$ at wing tip
E^h	Young's modulus of hinge material
E^w	Young's modulus of wing material
h	wing thickness
$\boldsymbol{I}$	matrix of moment of inertia
k_η	wing root stiffness
$\boldsymbol{K}^\mathrm{ela}$	stiffness matrix w.r.t the wing elastic deformation
$\boldsymbol{K}^\mathrm{rot}$	stiffness matrix w.r.t the wing rigid-body rotation
$\boldsymbol{M}^\mathrm{am}$	mass matrix due to added mass effect
$\boldsymbol{M}^\mathrm{w}$	wing mass matrix
$\boldsymbol{r}$	position vector
$\hat{r}_{m_1}$	dimensionless radius of the first moment of inertia
$\hat{r}_{m_2}$	dimensionless radius of the second moment of inertia
$\hat{r}_{s_1}$	dimensionless radius of the first moment of area
$\hat{r}_{s_2}$	dimensionless radius of the second moment of area
R	span of single wing
$\boldsymbol{R}$	rotation matrix
Re	Reynolds number
S	wing area
t	time
v	velocity
V	voltage applied to the active hinge
V^w	flapping wing volume

ABBREVIATIONS

AOA	angle of attack
BC	boundary condition
BEM	blade element method
BPDF	Beta probability density function
CFD	computational fluid dynamics
CP	center of pressure
CSD	computational structural dynamics
CWAD	chordwise area distribution
CWMD	chordwise mass distribution
DOF	degree of freedom
FSI	fluid-structure interaction
FWMAV	flapping wing micro air vehicle
LE	leading edge
PA	pitching axis
SWAD	spanwise area distribution
SWMD	spanwise mass distribution
TE	trailing edge

GREEK SYMBOLS

$\boldsymbol{\alpha}$	vector of angular acceleration
$\tilde{\alpha}$	angle of attack
$\boldsymbol{\epsilon}$	strain vector
ϵ_0	vacuum permittivity
ϵ_r	relative permittivity
η	pitching angle
θ	heaving angle
μ	friction coefficient
ν	Poisson's ratio
ρ^f	fluid density
ρ^w	wing density
σ_N	normal stress at the interface between the facings and the dielectric layers
τ_N	shear stress at the interface between the facings and the dielectric layers
$\boldsymbol{\tau}$	vector of torque
ϕ	sweeping angle
$\boldsymbol{\omega}$	vector of angular velocity

1

INTRODUCTION

1

1.1. BACKGROUND

1.1.1. FLAPPING WING MICRO AIR VEHICLE

Both biologists and engineers have been fascinated for centuries by the flight of birds and insects. One well-known example is that Leonardo da Vinci (1452-1519) designed a human-powered wing-flapping device in 1485 (Gray, 2003). Although there is no evidence that he actually built such a device, he drew detailed sketches for both the drive mechanism and the wing architecture by learning from birds. After that, many engineers also showed great interest in realizing flying with flapping wings, including Alphonse Pénaud (1850-1880) and Victor Tatin (1843-1913) from France (Chanute, 1894), Lawrence Hargrave (1850-1915) from Australia (Shaw & Ruhen, 1977), Otto Lilienthal (1848-1896) from Germany (Lilienthal, 1895), and Edward Purkis Frost (1842-1922) from England (Kelly, 2006).

In the past decades, locomotion with flapping wings has attracted much attention with the emergence of micro air vehicles (MAVs). Flapping flight owns inherent advantages for MAVs as compared to the traditional locomotion methods used by fixed wing aircrafts and rotary wing helicopters. The advantages of flapping wing micro air vehicles (FWMAVs) arise from both their unconventional aerodynamics and their great potential to reduce energy consumption. The unsteady aerodynamics exploited by flapping wings (Sane, 2003, Wei *et al.*, 2008) enables the generation of sufficient lift and thrust with the absence of fast forward speed, which gives FWMAVs the abilities to hover and conduct slow forward flight. In contrast, fixed wing aircrafts use steady aerodynamics to generate forces to stay aloft and fly forward, which normally results in lower lift coefficients on average as compared to the unsteady aerodynamics. Therefore, fixed wing aircrafts need to move fast enough to generate sufficient lift. Considering the aerodynamic drag quadratically increases with the velocity of the incoming flow, the power consumption during flying roughly increases cubically with the flight speed. This relation pinpoints the drawback of the locomotion methods with fixed or rotary wings in the context of the power efficiency considering their high rotational or translational speed.

Nowadays, MAVs have shown increasing socio-economic impacts in many fields (Floreano & Wood, 2015), such as low-altitude mapping and inspection, transportation of goods or medical service inside confined areas, and health-monitoring of infrastructures. However, long flight duration is generally required for the accomplishment of aforementioned tasks, and this requirement posts a challenge to rotary wing MAVs. As a consequence, FWMAVs are becoming more attractive both from the scientific and practical perspectives, as indicated by various FWMAVs designed and tested globally (e.g., de Croon *et al.*, 2009, Bolsman *et al.*, 2009, Keennon *et al.*, 2012, Ma *et al.*, 2013, Nguyen *et al.*, 2015). However, there are still limitations for the development of energy efficient FWMAVs which can outperform rotary and fixed wing MAVs dramatically or show performance close to natural flapping flight. The limitations originate from many aspects, including the physics involved in flapping flight, problems resulting from the scaling effect (Trimmer, 1989), and fabrication techniques for centimeter- and millimeter-scale structures. Many unsteady aerodynamic phenomena, including the prolonged leading edge vortex/vortices (Ellington *et al.*, 1996, Birch & Dickinson, 2001, Johansson *et al.*, 2013), wing-wing and wing-wake interactions (Lehmann & Pick, 2007, Lehmann, 2008) and fast pitching-up rotation (Meng & Sun, 2015), have been identified from insect flight

and proven to be beneficial for higher lift or thrust generation. However, the complicated coupling between these unsteady phenomena (or other unknowns), flexible wing structures and flapping kinematics are still not fully understood. When motors scale down with the dimension of mechanical systems, their power density normally scale down as well (Wood *et al.*, 2012). Meanwhile, the transmission efficiency due to the increased friction between the constituent components and the greater viscous loss will become problematic even though they are not vital for larger scale systems (Floreano & Wood, 2015). Different approaches have been developed to fabricate MAV systems, such as microelectromechanical systems (MEMS) techniques in sub-millimeter scale manufacturing (Judy, 2001), printed circuit MEMS (PC-MEMS) for mesoscale devices (Sreetharan *et al.*, 2012), and subtractive machining and additive manufacturing for centimeter-scale or large devices, etc. However, it is still a challenge to fabricate MAVs as a whole or with fewer components to increase the reproducibility and, thus, reduce the cost.

1.1.2. ATALANTA PROJECT

Seeing the great potential of FWMAVs in the future and also the related scientific challenges, the Atalanta project aims for an innovative integrated FWMAV design with 100 mm wing span and 4 g maximum vehicle mass, as shown by the prototype (Bolsman, 2010) in Fig. 1.1.
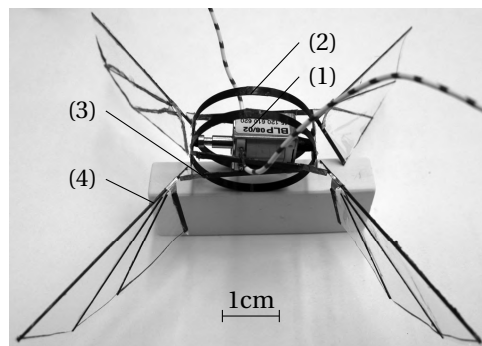
Figure 1.1: Prototype of four-winged Atalanta FWMAV designed by Bolsman (2010), which aims to exploit the resonance of such a compliant mechanism to realize wing actuation. This concept design consists of (1) a linear motor, (2) ring-based compliant structures, (3) compliant mechanical amplification mechanisms and (4) flexible wings.

In the past decade, the Atalanta team has conducted research addressing the following aspects:

- *Flight mechanism.* Inspired by insect thorax which drives the wings in a direct or an indirect manner with elastic deformation (Dudley, 2002), different drive mechanisms were designed by exploiting the bending or torsion of elastic elements to convert energy between actuator and wings (Bolsman, 2010). These types of drive mechanisms have the potential to implement resonance to achieve the wing motion and to restore the kinetic energy of flapping wings, which can decrease the

1

energy consumption as compared to traditional flight mechanisms using linkage mechanisms and gearboxes.

- *Actuator.* Traditional electromagnetic motors show a great drop of power density when scaled down. As an alternative, the Atalanta project is working on a chemical actuator which uses chemical energy directly, like all animals (van Wageningen, 2012, van den Heuvel, 2015). One of the highlights of the chemical actuator is that the self-weight decreases with the consuming of chemical fuel.
- *Sensing.* To avoid the large amount of power consumed by image data transmission or onboard image processing, optical flow based flight sensing and control methods are being developed to realize the autonomous flight status identification, obstacle avoidance and object approaching (Selvan, 2014).
- *Flight control.* The compliant mechanisms used by the Atalanta FWMAVs post new challenges for the flight control. One developed approach is to control the flapping wing kinematics by changing the dynamic response of the compliant system which can be realized by tuning the local structural properties (e.g., thickness, Young's modulus, temperature) (Peters *et al.*, 2016).

1.2. PROBLEM DESCRIPTION

Diverse wing morphologies can be found in the realm of insects (Ellington, 1984*a*,*b*, Dudley, 2002, Berman & Wang, 2007). The area, mass and stiffening materials of insect wings are carefully distributed to realize specific wing inertia and flexibility. In contrast, most existing flapping wing designs are either over-simplified in wing morphology (e.g., de Croon *et al.*, 2009, Bolsman *et al.*, 2009, Keennon *et al.*, 2012, Nguyen *et al.*, 2015) or directly duplicate the wing morphology of specific insects (e.g., Tanaka & Wood, 2010, Ha *et al.*, 2014). As one of the challenges posted by the Atalanta project, the present work is trying to identify the most influential wing characteristics with respect to the flight performance of flapping wings and to achieve new wing designs which can decrease the gap between artificial wings for FWMAVs and insect wings, particularly from the perspective of energy efficiency.

Figure 1.2 compares the continuous flight time of flying insects and different types of unmanned aerial vehicles (UAVs[1]). It can be seen that small-scale flapping wing UAVs, i.e., FWMAVs, show the shortest continuous flight time on average as compared to rotary wing and fixed wing UAVs. In contrast, some insects (e.g., *R. ferrugineus, S. laurasii, M. galloprovincialis*) can fly continuously for much longer time (more than 200 minutes) even with less body mass (Martí-Campoy *et al.*, 2016). Therefore, the energy efficiency is still a primary bottleneck to the application of FWMAVs in practice.

FWMAVs are essentially systems to convert energy from one form to other forms. As shown by the energy conversion diagram of FWMAVs in Fig. 1.3, the energy source (e.g., electrical or chemical energy) is primarily transformed into three other forms, i.e., the kinetic energy, potential energy and thermal energy. Some of these energy outputs are useful. For instance, the kinetic and elastic energy of the wing, the kinetic energy of fluid and the thermal energy resulting from the skin friction on the boundary layer of

---

[1] UAV represents any aircraft with no pilot on board while MAV is a class of miniature UAV that has a size restriction. United States Defense Advanced Research Projects Agency (DARPA) has defined the MAV as any flying vehicle which is limited to 150 mm or smaller in any linear dimension (e.g., wingspan, length).
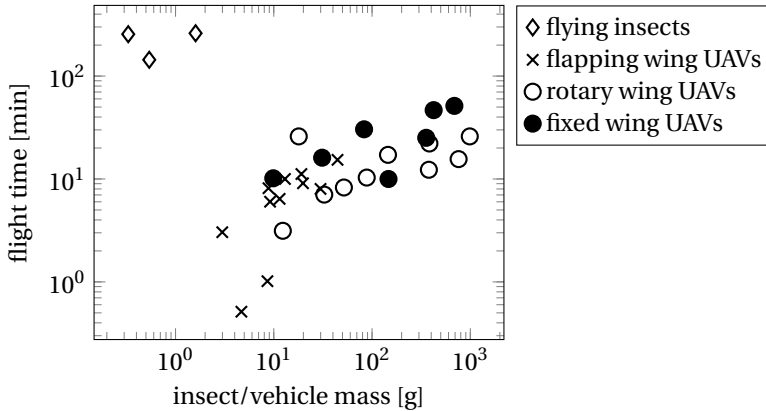
Figure 1.2: Continuous flight time versus mass of insects or unmanned aerial vehicles (UAVs). Data for insects and UAVs are adapted from Martí-Campoy *et al.* (2016) and Floreano & Wood (2015), respectively.

wings serve to do mechanical work to generate the lift and thrust. However, some energy outputs (e.g., thermal energy resulting from most frictions) only cause energy loss and, thus, reduce the energy efficiency of FWMAV systems.

Many ways can be used to increase the energy efficiency, for instance, the reduction of the dry friction in the drive mechanism by using less mechanical components (Bolsman *et al.*, 2009, Ma *et al.*, 2013), and the reuse of the elastic and kinetic energy stored by the wings and body of FWMAVs by including elastic components in the drive mechanism (Bolsman *et al.*, 2009, Lau *et al.*, 2014). Another way is to improve the performance of flapping wings by increasing the conversion efficiency from the energy generated by the drive mechanism to the useful work done to generate lift and thrust. However, it is still unclear on how to achieve wing designs which can dramatically decrease the energy consumption as compared to existing wing designs.

In order to design flapping wings for FWMAVs, flapping wings need to be mathematically modeled and parameterized. However, it is non-trivial to systematically model flapping wings considering the diversity of insect wing morphology and flapping kinematics. The modeling is also complicated by the unsteady aerodynamics associated to the reciprocating flapping wings at low Reynolds numbers and the dynamic aeroelasticity (Zhao *et al.*, 2010, Du & Sun, 2010, Shyy *et al.*, 2010) due to the interaction among elastic force, aerodynamic load and inertial load. Therefore, an important part of this thesis is to develop:

- an integrated morphological and kinematic model for flapping wings to capture the most important aspects that influence the efficiency of FWMAVs,
- a predictive aerodynamic model which enables a rapid and accurate evaluation of the aerodynamic performance of different wing designs,
- and a computationally efficient fluid-structure interaction (FSI) model which can be combined with optimization techniques to study the optimal wing flexibility.
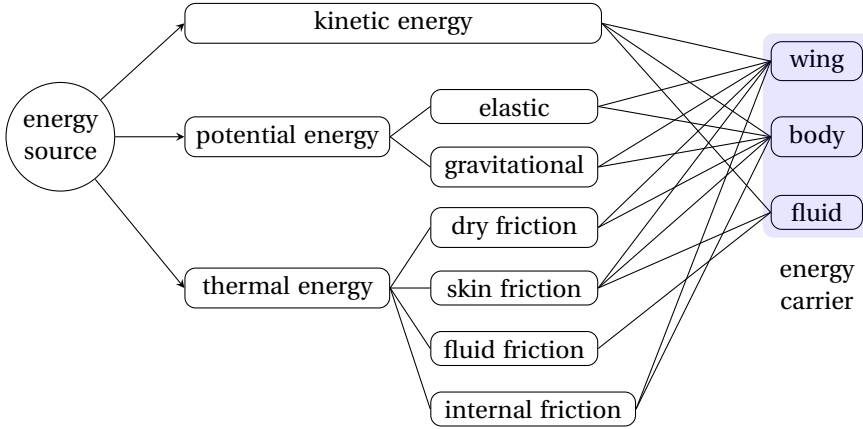
1

Figure 1.3: Energy conversion of FWMAVs.

1.3. AIM AND SCOPE

The main aim of this dissertation is to answer the following research question:

"How to design flapping wings for energy-efficient hovering flight?"

The energy efficiency is quantified by the cycle-averaged energy consumption which is normalized by the corresponding lift generation.

Considering the complexity of flapping flight, the scope of this work is intended to be limited to the design of flapping wings for hovering flight. This is because hovering flight is generally more energy-consuming as compared to forward flight (Dudley, 2002) and is one of the most important tasks that FWMAVs have to execute. New wing designs should be able to dramatically reduce the energy consumption during hovering flight as compared to existing flapping wing designs.

In order to reduce the design and manufacturing complicities of FWMAVs, their wings are typically driven back and forth by their drive mechanisms, the heaving motion is constrained by the extremely high out-of-stroke-plane bending stiffness, and the pitching motion is passively determined by the wing flexibility, inertia and aerodynamic loads. Therefore, this type of kinematics is assumed for the artificial wing design for the entire study.

1.4. OUTLINE

The structure of this dissertation is visualized in Fig. 1.4.

In Chapter 2, a predictive quasi-steady model of aerodynamic loads on flapping wings is presented. Based on the proposed aerodynamic model, the component-level designs of flapping wings are presented in Chapters 3, 4 and 5. In Chapter 3, the optimal location of the pitching axis for flapping wings with different shapes is investigated. Chapter 4 first introduces a computationally efficient FSI model based on the proposed quasi-steady model and an analytical representation of flapping wing twist is presented. Based on the proposed FSI model, the optimal twist is studied for a hawkmoth wing and an artificial flapping wing. In Chapter 5, an active method to change the stiffness of the elastic

hinge of flapping wings is introduced. The work in this chapter was carried out together with Hugo Peters.

In Chapter 6, the retrospection and discussion of the modeling and design of flapping wings are provided. The dissertation is finalized with conclusions and recommendations in Chapter 7.
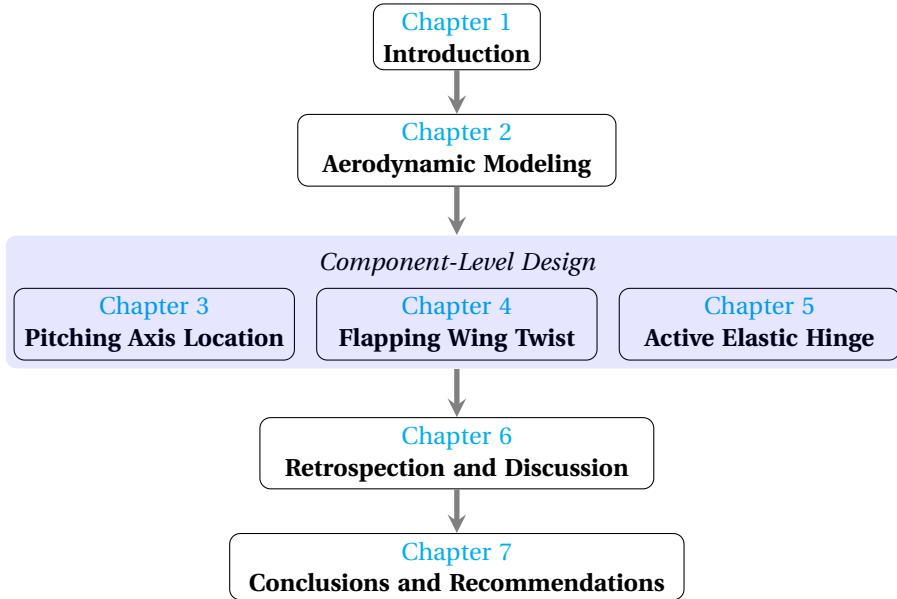

Figure 1.4: Visual outline of this dissertation.

2

A PREDICTIVE QUASI-STEADY MODEL OF AERODYNAMIC LOADS ON FLAPPING WINGS

Quasi-steady aerodynamic models play an important role in evaluating aerodynamic performance and conducting design and optimization of flapping wings. Most quasi-steady models are aimed at predicting the lift and thrust generation of flapping wings with prescribed kinematics. Nevertheless, it is insufficient to limit flapping wings to prescribed kinematics only since passive pitching motion is widely observed in natural flapping flights and preferred for the wing design of flapping wing micro air vehicles (FWMAVs). In addition to the aerodynamic forces, an accurate estimation of the aerodynamic torque about the pitching axis is required to study the passive pitching motion of flapping flights. The unsteadiness arising from the wing's rotation complicates the estimation of the center of pressure (CP) and the aerodynamic torque within the context of quasi-steady analysis. Although there are a few attempts in literature to model the torque analytically, the involved problems are still not completely solved.

In this chapter, we present an analytical quasi-steady model by including four aerodynamic loading terms. The loads result from the wing's translation, rotation, their coupling as well as the added-mass effect. The necessity of including all the four terms in a quasi-steady model in order to predict both the aerodynamic force and torque is demonstrated. Validations indicate a good accuracy of predicting the CP, the aerodynamic loads and the passive pitching motion for various Reynolds numbers. Moreover, compared to the existing quasi-steady models, the presented model does not rely on any empirical parameters and, thus, is more predictive, which enables application to the shape and kinematics optimization of flapping wings.

2

2.1. INTRODUCTION

One of the most fascinating features of insects is the reciprocating flapping motion of their wings. The flapping motion is generally a combination of wing translation (yaw) and rotation, where the rotation can be further decomposed into wing pitch and roll. The scientific study of insect flight dates back to the time Chabrier (1822) published a book on insect flight and related morphology. However, Hoff (1919) was probably the first to analyze the aerodynamics of insect flight with momentum theory which idealizes the stroke plane as an actuator-disk to continuously impart downward momentum to the air. Since then, aerodynamic modeling of the force generation by flapping wings, especially in an analytical way, has been a research focus for both biologists and engineers.

Analytical modeling of flapping wing performance can be roughly classified into three groups: steady-state models, (semi-empirical) quasi-steady models and unsteady models. Steady-state models, including the actuator-disk model (Hoff, 1919), provided us the first insight into the average lift generation and power consumption of flapping flight without digging into the time course of the transient forces (see Weis-Fogh (1972) and Ellington (1984d)). Meanwhile, quasi-steady models were investigated by Osborne (1951) and Ellington (1984c) by taking the change of the angle of attack (AOA) over time and the velocity variation along the wing span into consideration. Then, with the help of experimental studies on dynamically scaled mechanical flapping wings, empirical corrections were introduced into quasi-steady models to improve their accuracy. Typically these models are refereed to as semi-empirical quasi-steady models (e.g., Dickinson *et al.*, 1999, Berman & Wang, 2007). Recently, unsteady models attempted to analytically model the unsteady flow phenomena, for instance, the generation and shedding of leading edge vortices (LEVs) and trailing edge vortices (TEVs) (Ansari, 2004, Xia & Mohseni, 2013). These models are capable of demonstrating details of the changing flow field during flapping flight with much less computational cost as compared to the numerical simulations which directly solve the governing Navier-Stokes equations. The Kutta condition is generally enforced at the trailing edge by these unsteady models. However, as pointed out by Ansari *et al.* (2006), during stroke reversals the fluid is more likely to flow around the trailing edge rather than along it such that the applicability of the Kutta condition in the conventional sense is questionable.

With the emergence of flapping wing micro air vehicles (FWMAVs), design studies on flapping wings have stimulated research to keep improving existing quasi-steady models by capturing more unsteady characteristics of prescribed flapping motion without increasing the computational cost. Reviews on recent progress can be found in many papers (e.g., Sane, 2003, Ansari *et al.*, 2006, Shyy *et al.*, 2010). However, the pitching motion of flapping wings of insects, especially during wing reversals, is not always actively controlled. Torsional wave along the trailing edge (TE) of a wing traveling from the wing tip to root is considered as a signature of passive or partly passive wing pitching and has been observed on wings of Diptera (Ennos, 1989) and dragonfly (Bergou *et al.*, 2007). To simplify the drive mechanism, wings of FWMAVs are also designed to pitch passively (e.g., de Croon *et al.*, 2009, Bolsman *et al.*, 2009, Ma *et al.*, 2013). In this case, the pitching motion is governed by the wing flexibility, inertia and aerodynamic loads.

To study the passive pitching motion and help the wing design, both the aerodynamic force and torque must be calculated. Nevertheless, most existing quasi-steady
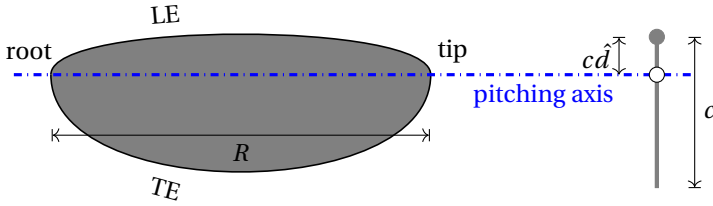
Figure 2.1: Illustration of the pitching axis of a flapping wing. In lateral view on the right, the filled circle in gray represents the leading edge (LE) of the wing, and $\hat{d}$ indicates the dimensionless distance from the LE to the pitching axis which is normalized by the chord length.

models are only interested in, and limited to, the prediction of the force generation. On the other hand, there are some attempts to model the torque in order to study the passive pitching behavior. For example, Bergou *et al.* (2007) employed a quasi-steady model to verify if sufficient pitching torque could be generated to realize passive wing reversals. The aerodynamic force on the wing was calculated based on the formulas used for studying fluttering and tumbling plates (Andersen *et al.*, 2005). To predict the passive pitching motion over an entire stroke, Whitney & Wood (2010) used a quasi-steady model that includes the aerodynamic loads due to the wing translation, rotation and added-mass effect with the help of some empirical coefficients. They pointed out that the effect of the coupling between wing translation and rotation was not included in their model since the corresponding center of pressure (CP) is hard to determine analytically due to the unsteadiness introduced by the wing rotation. However, experiments conducted by Sane & Dickinson (2002) show that the coupling effect and the position of the pitching axis (as shown in Fig. 2.1) have a big influence on the aerodynamic loads generated by flapping wings. Consequently, both should be included into the quasi-steady aerodynamic model. Another common limitation of most existing quasi-steady models is the heavy dependence on empirical parameters. Those parameters need to be determined by experiments each time the wing shape is changed. This hinders their application to wing design and optimization.

In the present work, we propose a more comprehensive and predictive quasi-steady model by including four aerodynamic loading terms that result from the wing's translation, rotation, their coupling as well as the added-mass effect. In Sec. 2.2, we demonstrate the necessity of including all the four terms for a quasi-steady model in order to predict both the aerodynamic force and torque accurately. In Sec. 2.3, two validations are used to show the capability and accuracy of the proposed model to predict the CP, aerodynamic loads and passive pitching motion by comparing with experimental data and other existing quasi-steady models. Conclusions are provided in Sec. 2.4.

2.2. FORMULATION

The reciprocating flapping motion is the most prominent feature of flapping wings, which sets it apart from other traditional methods of flight. The flapping motion results in large geometrical AOA which would stall conventional translating wings. For flapping wings,

generally, the flow starts to separate at the LE after wing reversals, and forms a LEV or LEVs (Johansson *et al.*, 2013). Instead of growing quickly and then shedding into the wake, the LEV on flapping wings generally remains attached over the entire half-strokes for two possible reasons: (1) the spanwise flow from the wing root to tip removes energy from the LEV which limits the growth and the shedding, as shown on hawkmoth wings (Ellington *et al.*, 1996); and (2) due to the downwash flow induced by the tip and wake vortices, the effective AOA decreases and the growth of the LEV is restricted, as indicated by the wings of Drosophila (Birch & Dickinson, 2001). The prolonged attachment of the LEV assists flapping wings to maintain high lift. This phenomenon makes it more convenient to analytically model the aerodynamic effect of the attached LEV compared to the case that the LEV sheds before the pitching reversal.

To analytically predict the unsteady aerodynamic loads on flapping wings, we presume that:

- The flow is incompressible, i.e., the fluid density ρ^{f} is regarded as a constant. This is justified due to the relative low average wing tip velocity compared to the speed of sound (Sun, 2014).
- The wing is a rigid, flat plate. Wings of some small insects (e.g., fruitfly wings (Ellington, 1999)) and FWMAV wings (Ma *et al.*, 2013) show negligible wing deformation. Even for wings of larger insects, the enhancement of lift due to wing camber and twisting is generally less than 10% compared to their rigid counterparts (Sun, 2014). The wing thickness t is also negligible when compared to the other two dimensions, i.e., the average chord length $\bar{c}$ and span R (see Fig. 2.1).
- The resultant aerodynamic force acting on the wing is perpendicular to the chord during the entire stroke. This assumption is supported by three facts: (1) the leading-edge suction force (Sane, 2003) is negligible for a plate with negligible thickness; (2) the viscous drag on the wing surface is marginal as compared to the dominant pressure load when moving at a post-stall AOA; (3) the strength of the bound circulation, which results in a net force perpendicular to the incoming flow, is negligible as compared to the vorticity-induced circulation (Ford & Babinsky, 2014).
- A quasi-steady state is assumed for an infinitesimal duration such that the transient loads on the flapping wing are equivalent to those for steady motion at the same instantaneous translational velocity, angular velocity and AOA.

Considering the variation in the velocity and acceleration along the wing span, the blade element method (BEM) (Osborne, 1951) is used for discretizing the wing into chordwise strips with finite width. The resultant loads can be calculated by integrating strip loads over the entire wing. As a consequence of the quasi-steady assumption, the time dependence of the aerodynamic loads primarily arises from the time-varying kinematics.

2.2.1. FLAPPING KINEMATICS

To describe the kinematics of a rigid flapping wing, three successive rotations, i.e., sweeping motion (yaw), heaving motion (roll) and pitching motion (pitch), are used, as illustrated by the "cans in series" diagram in Fig. 2.2. Four different frames are involved in these rotations, including an inertial frame $x_i y_i z_i$, two intermediate frames $x_\theta y_\theta z_\theta$ and

Figure 2.2: Successive wing rotations used to describe the kinematics of a rigid flapping wing, shown using the "cans in series" approach proposed by Schwab & Meijaard (2006). Four different frames are involved in these rotations, including an inertial frame $x_i y_i z_i$, two intermed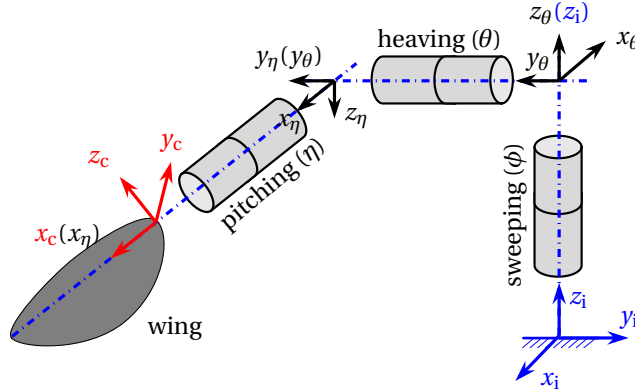iate frames $x_\theta y_\theta z_\theta$ and $x_\eta y_\eta z_\eta$, and a co-rotating frame $x_c y_c z_c$. All these frames share the same origin although they are drawn at various locations.

$x_\eta y_\eta z_\eta$, and a co-rotating frame $x_c y_c z_c$. The inertial frame $x_i y_i z_i$ is fixed at the joint that connects the wing to body. Axes x_i and y_i confine the stroke plane while the z_i axis is perpendicular to this plane and follows the right-hand rule which holds for all the frames. The rotation around the z_i axis represents the sweeping motion and results in the intermediate frame $x_\theta y_\theta z_\theta$. The heaving motion is the rotation around the y_θ axis and leads to another intermediate frame $x_\eta y_\eta z_\eta$, where the pitching motion is conducted about its x_η axis. Eventually, we get the co-rotating frame $x_c y_c z_c$, which is fixed to and co-rotates with the wing. Its x_c axis coincides with the pitching axis, and the z_c axis coincides with the wing plane and perpendicular to the x_c axis. Both the inertial frame $x_i y_i z_i$ and the co-rotating frame $x_c y_c z_c$ are of particular interest for the study of flapping wing motion and aerodynamic performance. The quasi-steady aerodynamic model presented in this chapter is constructed in the co-rotating frame in order to facilitate the application of the BEM, while the lift and drag are generally quantified in the inertial frame.

The flapping motion can be quantified using three Euler angles: sweeping angle ϕ, heaving angle θ and pitching angle η. An example of these Euler angles during flapping motion has been demonstrated in a semi-sphere constructed in the inertial frame, as shown in Fig. 2.3. It can been seen that ϕ is the angle between the x_i axis and the projection of the x_c axis on the stroke plane, θ is the angle between the x_c axis and its projection on the stroke plane, and η is the angle between the z_c axis and the plane that is perpendicular to the stroke plane and parallels to the x_c axis. With these Euler angles, three successive rotations, i.e., the sweeping, heaving and pitching motion, can be formulated
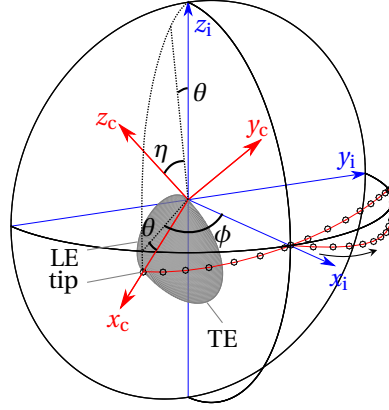
Figure 2.3: Two frames and three Euler angles demonstrated in a semi-sphere. Frames $x_i y_i z_i$ and $x_c y_c z_c$ are fixed to the origin and co-rotates with the wing, respectively. Axes x_i and y_i confine the stroke plane. The small circles indicate the wing tip trajectory ("∞" shape here as an example). The plane constructed by the dashed lines is perpendicular to the stroke plane and parallels to the x_c axis. ϕ, θ and η represent the sweeping, heaving and pitching angle, respectively.

as

$$
\boldsymbol{R}_\phi = \left[\begin{array}{ccc} \cos\phi & -\sin\phi & 0 \\ \sin\phi & \cos\phi & 0 \\ 0 & 0 & 1 \end{array}\right], \boldsymbol{R}_\theta = \left[\begin{array}{ccc} \cos\theta & 0 & \sin\theta \\ 0 & 1 & 0 \\ -\sin\theta & 0 & \cos\theta \end{array}\right], \boldsymbol{R}_\eta = \left[\begin{array}{ccc} 1 & 0 & 0 \\ 0 & \cos\eta & -\sin\eta \\ 0 & \sin\eta & \cos\eta \end{array}\right],
$$
(2.1)

respectively.

The quasi-steady model proposed in this work calculates the aerodynamic loads in the co-rotating frame. Therefore, the flapping velocity and acceleration in the co-rotating frame are required. The angular velocity $\boldsymbol{\omega}_c$ and angular acceleration $\boldsymbol{\alpha}_c$ can be obtained by transforming the sweeping and heaving motion from corresponding frames into the co-rotating frame where the wing pitching motion is described, as in,

$$
\boldsymbol{\omega}_c = \boldsymbol{R}_\eta^{\mathrm{T}} \boldsymbol{R}_\theta^{\mathrm{T}} \boldsymbol{R}_\phi^{\mathrm{T}} \dot{\phi} \boldsymbol{e}_{z_i} + \boldsymbol{R}_\eta^{\mathrm{T}} \boldsymbol{R}_\theta^{\mathrm{T}} \dot{\theta} \boldsymbol{e}_{y_\theta} + \boldsymbol{R}_\eta^{\mathrm{T}} \dot{\eta} \boldsymbol{e}_{x_\eta} = \left[\begin{array}{c} \dot{\eta} - \dot{\phi}\sin\theta \\ \dot{\theta}\cos\eta + \dot{\phi}\cos\theta\sin\eta \\ \dot{\phi}\cos\eta\cos\theta - \dot{\theta}\sin\eta \end{array}\right],
$$
(2.2)

and

$$
\boldsymbol{\alpha}_c = \dot{\boldsymbol{\omega}}_c = \left[\begin{array}{c} \ddot{\eta} - \ddot{\phi}\sin\theta - \dot{\phi}\dot{\theta}\cos\theta \\ \ddot{\phi}\cos\theta\sin\eta + \ddot{\theta}\cos\eta - \dot{\eta}\dot{\theta}\sin\eta + \dot{\phi}(\dot{\eta}\cos\eta\cos\theta - \dot{\theta}\sin\eta\sin\theta) \\ \ddot{\phi}\cos\eta\cos\theta - \ddot{\theta}\sin\eta - \dot{\eta}\dot{\theta}\cos\eta - \dot{\phi}(\dot{\eta}\cos\eta\sin\eta + \dot{\theta}\cos\eta\sin\theta) \end{array}\right],
$$
(2.3)

where $\boldsymbol{e}_{z_i}$, $\boldsymbol{e}_{y_\theta}$ and $\boldsymbol{e}_{x_\eta}$ are unit vectors in the z_i, y_θ and x_η directions, respectively.

In the co-rotating frame, the translational velocity and acceleration of a point on the pitching axis with a position vector $\boldsymbol{r} = [x_c, 0, 0]^{\mathrm{T}}$ can be calculated by

$$
\boldsymbol{v}_c = \boldsymbol{\omega}_c \times \boldsymbol{r} = x_c[0, \omega_{z_c}, -\omega_{y_c}]^{\mathrm{T}},
$$
(2.4)

and

$$\boldsymbol{a}_\mathrm{c} = \boldsymbol{\alpha}_\mathrm{c} \times \boldsymbol{r} + \boldsymbol{\omega}_\mathrm{c} \times \boldsymbol{v}_\mathrm{c} = x_\mathrm{c}[-\omega_{y_\mathrm{c}}^2 - \omega_{z_\mathrm{c}}^2, \alpha_{z_\mathrm{c}} + \omega_{x_\mathrm{c}}\omega_{y_\mathrm{c}}, \omega_{x_\mathrm{c}}\omega_{z_\mathrm{c}} - \alpha_{y_\mathrm{c}}]^\mathrm{T}, \qquad (2.5)$$

where the term $\boldsymbol{\omega}_\mathrm{c} \times \boldsymbol{v}_\mathrm{c}$ represents the Coriolis effect due to the rotation of the co-rotating frame.

Given the kinematic information, we are able to determine the aerodynamic loads on a flapping wing during hovering. If, instead, the forward flight is studied, the contribution of the velocity of forward flight to the resultant translational velocity has to be included. This can be done by transforming the forward velocity from the inertial frame to the co-rotating frame and then adding this to the translational velocity $\boldsymbol{v}_\mathrm{c}$ as formulated in Eq. 2.4.

2.2.2. AERODYNAMIC MODELING

For flapping wings, it is attractive to model the aerodynamic loads analytically since the numerical simulations by directly solving the governing Navier-Stokes equations are extremely time-consuming and also require a comprehensive representation of the flow physics for high accuracy. The design and optimization of flapping wings for FWMAVs also demand an efficient tool to quickly evaluate the aerodynamic performance of given designs.

As a result of the unsteadiness of the fluid surrounding flapping wings, it is nontrivial to analytically formulate the total aerodynamic load in a single term. Instead, we separate it into four parts: the translation-induced load, the rotation-induced load, the load resulting from the coupling between the wing translation and rotation and the load due to the added-mass effect, as illustrated in Fig. 2.4. The first three components represent the pressure loads induced by the translational and/or rotational velocities while the added-mass effect results from the energy dissipation or absorption by the fluid that is decelerated or accelerated by the flapping wing. The contribution of added-mass effect to the resultant aerodynamic load relies on the values of translational and rotational acceleration as well as the location of rotation axis, which are normally represented by the matrix of added-mass coefficients. These coefficients for two-dimensional plates have been well studied (Newman, 1977) and, thus, are used in this model by combining with the BEM. However, different combinations of the first three terms can be found in literature depending on the problems studied. In Table 2.1, we compare two quasi-steady models (Berman & Wang, 2007, Whitney & Wood, 2010) which have been commonly used with the proposed model on four aspects: (1) capability of predicting the resultant force and torque, (2) composition of the resultant loads, (3) whether a real pitching axis position is used, and (4) dependence on empirical parameters. For flapping wings with fully prescribed kinematics, generally, the desired information is the (average) aerodynamic force. The rotation-induced force is ignored in these cases for two reasons: (1) the transient force due to pure rotation will be zero if the wing platform is symmetric about the pitching axis, which is generally assumed (Berman & Wang, 2007), (2) the average force due to the pure rotation over one flapping cycle is zero if its two half-strokes mirror each other. For flapping wings with passive pitching motion, both the temporal aerodynamic force and torque are required to calculate the pitching motion. The contribution of the pure wing rotation has to be considered since the distributed damping load due to wing rotation always adds a torque about the pitching axis no matter if the net

Table 2.1: Comparison of the characteristics between two existing quasi-steady models and the proposed model. "-" means that the resultant torque estimation was not the objective of the model of Berman & Wang (2007) and thus not present in their paper.

items	Berman & Wang (2007)	Whitney & Wood (2010)	proposed model
resultant force	Yes	Yes	Yes
resultant torque	-	Yes	Yes
translation-induced loads	Yes	Yes	Yes
rotation-induced loads	No	Yes	Yes
coupling loads	Yes	No	Yes
added-mass loads	Yes	Yes	Yes
empirical parameters	Yes	Yes	No
pitching axis position	fixed at half chord	real	real

force is zero or not. However, the coupling effect between the translation and rotation of the wing is generally ignored (Whitney & Wood, 2010) or considered without taking the pitching axis into consideration (Bergou *et al.*, 2007). This is because of the difficulty in analytically determining the contribution of wing rotation to the aerodynamic loads due to the unsteadiness. It can be seen that existing quasi-steady models show inconsistency in the loading terms that are included. Therefore, this work aims to achieve a better quasi-steady model from the perspectives of:

- eliminating the inconsistency in the loading terms,
- modeling the total contribution of the wing rotation to the resultant aerodynamic loads and corresponding CP more accurately,
- and further reducing the dependence on empirical parameters.

In the following subsections, the components as listed in Fig. 2.4 will be elucidated in sequence. After that, the Wagner effect (Wagner, 1925) and corresponding conditions under which it should be considered are discussed.

TRANSLATION-INDUCED LOAD

Experimental studies (Ellington *et al.*, 1996, Pitt Ford & Babinsky, 2013, Percin & van Oudheusden, 2015) show that the LEV dominates the force generation of translational wings compared to the bound circulation. Due to the unsteadiness of the LEV, the translational lift coefficient C_L^{trans} is generally measured on dynamically scaled flapping wings. According to experimental results obtained on different wings (Dickinson *et al.*, 1999, Usherwood & Ellington, 2002*b*, Wang *et al.*, 2004), the lift coefficient can be approximately formulated as

$$C_L^{\text{trans}} = A\sin(2\tilde{\alpha}), \tag{2.6}$$

where A is the maximum lift coefficient to be determined experimentally for different wings, and the AOA ($\tilde{\alpha}$) for a rigid wing model can be calculated by

$$\tilde{\alpha} = \arccos(|v_{z_c}/v_c|) = \arccos\left(\left|\omega_{y_c}/\sqrt{\omega_{y_c}^2 + \omega_{z_c}^2}\right|\right), \qquad \text{if} \quad \boldsymbol{v}_c \neq \boldsymbol{0}. \tag{2.7}$$

total
aerodynamic
load

(1)
translation-
induced load

(2)
rotation-
induced load
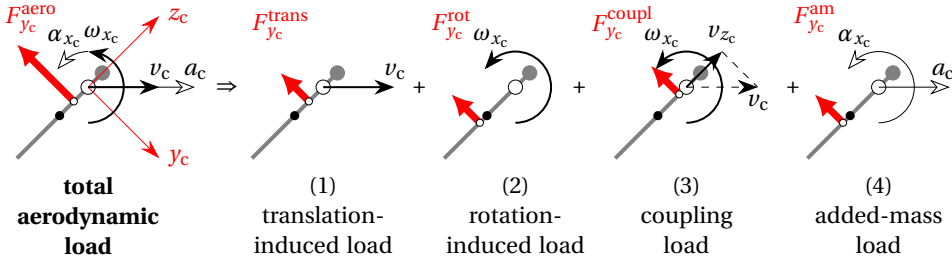
(3)
coupling
load

(4)
added-mass
load

Figure 2.4: Decomposition of total aerodynamic loads on a flapping wing. The wing kinematic quantities and aerodynamic forces are illustrated qualitatively. The gray line segments, gray dots, larger white circles and black dots represent the chord, leading edge (LE), pitching axis and chord center, respectively. The smaller white circles indicate the locations of center of pressure/load induced by each term.

According to Eq. 2.6, the wing translating at an AOA of 45° gives the maximum lift, but the maximum value A might differ from one wing to the other. The experimental determination of A hinders a general application to calculate the lift coefficient of arbitrary wings. Based on the extended lift line theory (Schlichting & Truckenbrodt, 1979) for low-aspect-ratio wings in an incompressible flow, Taha *et al.* (2014) used an analytical expression for the coefficient A of a flat flapping wing. That is

$$A = \frac{\pi \mathcal{R}}{2 + \sqrt{\mathcal{R}^2 + 4}},\tag{2.8}$$

where $\mathcal{R}$ is the aspect ratio, defined as $R/\bar{c}$. Using Eq. 2.8, rather good estimations of the lift coefficients for translational flapping wings with different aspect ratios can be achieved according to the comparison with experimental data (see Taha *et al.* (2014)).

It should be note that C_L^{trans} is the three-dimensional (3D) lift coefficient for the entire wing. However, it is more useful to know the two-dimensional (2D) coefficient (C_l^{trans}) for the wing airfoil that can be used directly in the BEM. Conventionally, the translational velocity at the radius of gyration is taken as the reference to calculate the aerodynamic forces for the entire flapping wings (e.g., Harbig *et al.*, 2014, Lee *et al.*, 2015, Percin & van Oudheusden, 2015). In this case, the same resultant translational lift can be obtained by BEM with C_l^{trans} which takes the value of C_L^{trans}, as shown in Appendix A. Therefore, C_L^{trans} is directly used in our quasi-steady model to evaluate the translational aerodynamic forces.

According to the assumption that the resultant force is perpendicular to the wing surface (i.e., aligned with the y_c axis), the translational drag and resultant force coefficients can be calculated by using the translational lift coefficient as formulated in Eq. 2.6, as given by

$$C_D^{\text{trans}} = C_L^{\text{trans}} \tan(\tilde{\alpha})\tag{2.9}$$

and

$$C_{F_{y_c}}^{\text{trans}} = C_L^{\text{trans}}/\cos(\tilde{\alpha}).\tag{2.10}$$

Using Eqs. 2.6, 2.9 and 2.10, we calculate the analytical lift, drag and resultant force co-efficients as a function of the AOA for a dynamically scaled hawkmoth wing (Usherwood & Ellington, 2002a) and Drosophila wing (Dickinson *et al.*, 1999), respectively, as shown in Fig. 2.5(a). The order of magnitudes of the Reynolds number of the hawkmoth wing ($\mathcal{R} = 2.83$) and Drosophila wing ($\mathcal{R} = 3.74$) are 10^3 and 10^2, respectively. Comparison of the polar plots based on the analytical and experimental results is given in Fig. 2.5(b). It can be seen that the analytical lift and drag coefficients agree with the experimental results very well for both wings except for the discrepancy at the pre-stall AOAs (i.e., $0° \sim 20°$) for the Drosophila wing. The discrepancy is mainly because of the neglected viscous drag at the boundary layer in the proposed model while the drag does exist in reality, especially at small Reynolds number and low AOA. However, the AOA of flapping wings is normally in the post-stall region. Therefore, it is acceptable to use the analytical formulas to predict the force coefficients of translational wings.
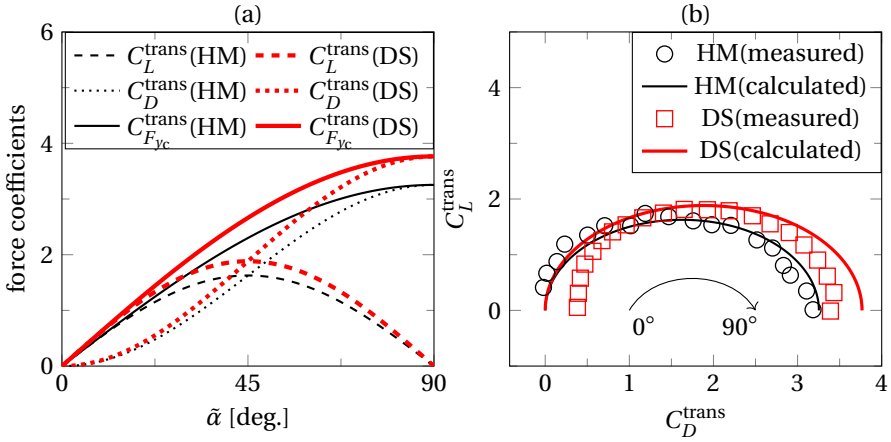

Figure 2.5: Force coefficients of two different translational wings. HM and DS represent dynamically scaled wings by mimicking wings of hawkmoth (Usherwood & Ellington, 2002a) and Drosophila (Dickinson *et al.*, 1999), respectively. (a) Analytical lift, drag and resultant force coefficients calculated with Eqs. 2.6, 2.9 and 2.10. (b) Comparison of analytical and measured force coefficients represented by polar plots which show the relationship between the translation-induced lift and drag coefficients at AOAs ranging from 0° to 90° in 5° and 4.5° increments for the HM and DS wings, respectively.

The resultant wing translation-induced force $F_{y_c}^{\text{trans}}$ can be calculated by integrating over the wing surface as in

$$F_{y_c}^{\text{trans}} = -\text{sgn}(\omega_{z_c})\frac{1}{2}\rho^f(\omega_{y_c}^2 + \omega_{z_c}^2)C_{F_{y_c}}^{\text{trans}}\int_0^R x_c^2 c\,dx_c, \qquad (2.11)$$

where $\text{sgn}(\cdot)$ is the signum function and c is the chord length as a function of the radius x_c. The translational velocity v_c shown in Fig. 2.4 is written as $x_c\sqrt{\omega_{y_c}^2 + \omega_{z_c}^2}$. It should be

noted that the angular velocity has been taken out of the integration based on the rigid wing assumption.

Experimental measurements of the center of pressure (CP) on flapping wings that translate at different AOAs have been conducted by Dickson *et al.* (2006) on a dynamically scaled Drosophila wing and by Han *et al.* (2015) on a hawkmoth wing. The measured chordwise CP locations $\hat{d}_{cp}^{trans}$ for both hawkmoth and Drosophila wing, which have been normalized by local chord length, are linearly fitted and plotted as a function of AOA in Fig. 2.6. Both lines show the shift of the CP from near the LE ($\hat{d}_{cp}^{trans} = 0$) to the chord center ($\hat{d}_{cp}^{trans} = 0.5$) with the increase of AOA. In the proposed model, the value of $\hat{d}_{cp}^{trans}$ is assumed to be linear to the AOA as given by

$$\hat{d}_{cp}^{trans} = \frac{1}{\pi}\tilde{\alpha}, \quad \text{where} \quad 0 \leqslant \tilde{\alpha} \leqslant \frac{\pi}{2}, \tag{2.12}$$

which indicates that the proposed formula assumes that $\hat{d}_{cp}^{trans}$ is equal to 0 and 0.5, respectively, when AOA is 0 and $\pi/2$. For the post-stall AOA which is generally experienced by flapping wings, the CP location from the proposed formula almost stays between the empirical data obtained from two model wings.
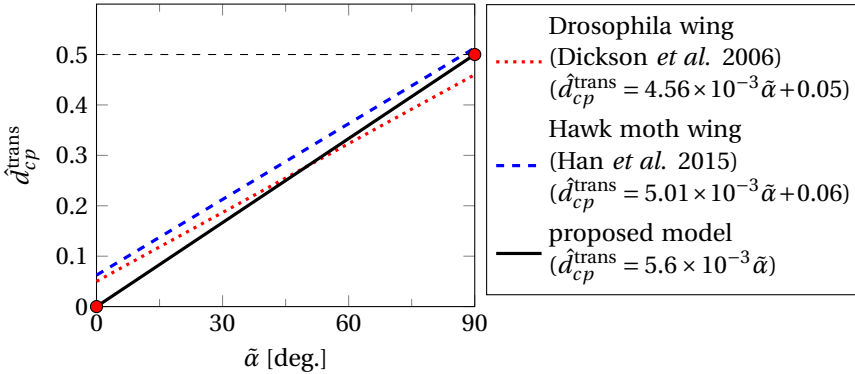

Figure 2.6: Measured chordwise centre of pressure (CP) for dynamically scaled insect wings and the analytical formula of CP used in our model. The values of CP are normalized by local chords and denoted as $\hat{d}_{cp}^{trans}$.

With the analytical resultant force and the chordwise CP location for translating wings, the torques around the x_c axis and z_c axis of the co-rotating frame can be expressed as

$$\tau_{x_c}^{trans} = \begin{cases} -\text{sgn}\left(\omega_{z_c}\right)\frac{\rho^f}{2}\left(\omega_{y_c}^2 + \omega_{z_c}^2\right)C_{F_{y_c}}^{trans}\left(\hat{d}_{cp}^{trans} - \hat{d}\right)\int_0^R x_c^2 c^2 \, dx_c, & \omega_{y_c} \leqslant 0 \\ -\text{sgn}\left(\omega_{z_c}\right)\frac{\rho^f}{2}\left(\omega_{y_c}^2 + \omega_{z_c}^2\right)C_{F_{y_c}}^{trans}\left(1 - \hat{d}_{cp}^{trans} - \hat{d}\right)\int_0^R x_c^2 c^2 \, dx_c, & \omega_{y_c} > 0 \end{cases} \tag{2.13}$$

and

$$\tau_{z_c}^{trans} = -\text{sgn}\left(\omega_{z_c}\right)\frac{\rho^f}{2}\left(\omega_{y_c}^2 + \omega_{z_c}^2\right)C_{F_{y_c}}^{trans}\int_0^R x_c^3 c \, dx_c, \tag{2.14}$$

where $\hat{d}$ is the normalized distance between the LE and the pitching axis (see Fig. 2.1), and the negative and positive values of ω_{y_c} mean that the translational velocity component v_{z_c} $(= -x_c\omega_{y_c})$ points at the LE and TE, respectively. When $\omega_{y_c} > 0$, the real AOA is higher than 90° which is not covered by the analytical model for AOA as shown in Fig. 2.6. This situation is handled by taking the TE as the LE, then the AOA becomes less than 90°. The torque about y_c axis is zero since the resultant force is assumed to be perpendicular to the wing.

The translation-induced loads have been analytically represented while taking account of the influence of $\mathit{\Re}$. This allows further application to study the wing shape influence in an analytical manner.

ROTATION-INDUCED LOAD

When a wing rotates about an arbitrary axis in a medium, it experiences distributed loads. Although the resultant force is zero if the wing is symmetric about its rotation axis, the resultant torque about the rotation axis is non-zero. Therefore, it is necessary to include this rotation-induced load in the quasi-steady model to correctly calculate the aerodynamic torque. In fact, this loading term is excluded by most existing quasi-steady models.

To calculate this load using BEM, the wing has to be discretized into chordwise strips first. For a rotating wing, different velocities are induced in the chordwise direction (= $-z_c\omega_{x_c}$), of which the amplitude linearly increases with the distance from the pitching axis. The chordwise velocity gradient requires the discretization of each chordwise strip as well. Consequently, the resultant rotation-induced force is calculated by integrating the load on each infinitesimal area (i.e., $dx_c dz_c$) over the entire wing surface, as in

$$F_{y_c}^{\text{rot}} = \frac{\rho^f}{2}\omega_{x_c}|\omega_{x_c}|C_D^{\text{rot}}\int_0^R\int_{\hat{d}c-c}^{\hat{d}c} z_c\,|z_c|\,dz_c dx_c, \tag{2.15}$$

where C_D^{rot} is the rotational damping coefficient, $\hat{d}c-c$ and $\hat{d}c$ are the coordinates of the wing's trailing edge (TE) and leading edge (LE) in the z_c direction, respectively. Meanwhile, the resultant torques around axes x_c and z_c are calculated by

$$\tau_{x_c}^{\text{rot}} = -\frac{\rho^f}{2}\omega_{x_c}|\omega_{x_c}|C_D^{\text{rot}}\int_0^R\int_{\hat{d}c-c}^{\hat{d}c} |z_c|^3\,dz_c dx_c, \tag{2.16}$$

and

$$\tau_{z_c}^{\text{rot}} = \frac{\rho^f}{2}\omega_{x_c}|\omega_{x_c}|C_D^{\text{rot}}\int_0^R\int_{\hat{d}c-c}^{\hat{d}c} z_c\,|z_c|\,x_c dz_c dx_c. \tag{2.17}$$

This discretization approach was also used by Andersen *et al.* (2005) with a value of 2.0 for C_D^{rot} on a tumbling plate and by Whitney & Wood (2010) with a value of 5.0 for flapping wings to achieve a better agreement between theoretical and experimental results. It is necessary to generalize this coefficient to enable the application for different flapping wings. The damping load on a rotating plate is analogous to the load acting on a plate that is placed vertically in a flow with varying incoming velocities from the top to bottom. The latter is basically the case for a translational wing at an angle of attack of 90°. However, it is questionable if it is sufficient to use the traditional drag coefficient for

a pure translating plate normal to flow (≈ 2 for a flat plate at $Re = 10^5$ (Anderson, 2010)). During the wing reversals of flapping motion, the sweeping motion is almost seized but the pitching velocity is nearly maximized. In this case, the pure rotational load dominates the aerodynamic loading which is still influenced by the flow field induced by the past sweeping motion. In this situation, it is more correct to use the translational drag coefficient C_D^{trans} for a sweeping wing (see Eq. 2.9) when AOA is equal to $90°$ as the rotational damping coefficient, i.e.,

$$C_D^{\text{rot}} = C_D^{\text{trans}}(\tilde{\alpha} = \frac{\pi}{2}) = \frac{2\pi \mathcal{R}}{2 + \sqrt{\mathcal{R}^2 + 4}}, \tag{2.18}$$

which normally leads to higher damping coefficients (e.g., $C_D^{\text{rot}} = 3.36$ when $\mathcal{R} = 3$) as compared to the drag coefficient for a pure translating plate normal to flow.

To avoid alternating the LE during flapping, which increases the power consumption, the pitching axes of flapping wings are generally located between the LE and the center line (Berman & Wang, 2007). The CP location of the load induced by the pure rotation, which is defined as the local-chord-length-normalized distance from the LE to the CP, can be determined by

$$\hat{d}_{\text{cp}}^{\text{rot}} = -\frac{3}{4} \frac{(\hat{d} - 1)^4 + \hat{d}^4}{(\hat{d} - 1)^3 + \hat{d}^3} + \hat{d}, \quad \text{where} \quad 0 \leq \hat{d} < 0.5, \tag{2.19}$$

which implies that the CP moves from $3/4$ chord to infinity while the pitching axis moves from the LE to the chord centre.

COUPLING LOAD

Although the translation- and rotation-induced loads have been modeled analytically and separately, they are insufficient to represent the loads on the wing conducting translation and rotation simultaneously because of the nonlinearity introduced by the fluid-wing interaction. Considering a wing whose planform is symmetric about its pitching axis and moving with constant translational and rotational velocities, the resultant rotation-induced force $F_{y_c}^{\text{rot}}$ is equal to zero. The resultant force, therefore, should be equal to the translational force $F_{y_c}^{\text{trans}}$ for a linear system assumption. However, for this case, the experiment conducted by Sane & Dickinson (2002) reported higher resultant force compared to $F_{y_c}^{\text{trans}}$. This additional force is explained by the coupling effect between the wing translation and rotation.

Traditionally, the coupling load on a plate with translational velocity v, rotational angular velocity ω_{x_c}, chord c and unit span is formulated as

$$F_{\text{trad}}^{\text{coupl}} = \rho^{\text{f}} v \underbrace{C^{\text{coupl}} \omega_{x_c} c^2 \left(\frac{3}{4} - \hat{d} \right)}_{\text{rotational circulation}}, \tag{2.20}$$

where C^{coupl} is a constant coupling coefficient equal to π. The term was first included into a quasi-steady model for flapping wings by Ellington (1984c) to reflect the contribution of wing rotation on the aerodynamic force. Since then, this term is widely used in quasi-steady analysis (Dickinson *et al.*, 1999, Sane & Dickinson, 2002, Nabawy &

Crowther, 2014) for different types of insect wings. It is generally assumed that the contribution of the wing rotation can be represented by this single coupling term without considering the load due to the pure wing rotation. However, there are some limitations for the coupling term to fully represent the rotational effect. Firstly, the coupling coefficient C^{coupl} in Eq. 2.20 is a constant, but experiments (Sane & Dickinson, 2002, Han *et al.*, 2015) have shown its dependency on the ratio between the translational velocity v and rotational angular velocity ω_{x_c}. Secondly, the influence of the wing rotation on the location of center of pressure (CP) can not be reflected purely by the coupling term presented in Eq. 2.20. In fact, according to the experimental results from Han *et al.* (2015), the trajectories of CP locations for different AOAs are different when the wing is pitching up at different velocities even though the sweeping motion is maintained. Thirdly, this single term fails to predict the aerodynamic force due to wing rotation when the pitching axis is at 3/4 chord ($F^{\text{coupl}}_{\text{trad}} = 0$ for this case). Fourthly, at the start and end of each half-stroke, the rotational torque predicted by Eq. 2.20 is small as a result of small translational velocity v. However, the aerodynamic torque about the pitching axis at these moments can be considerable due to the pure wing rotation, as shown in subsection 2.2.2.
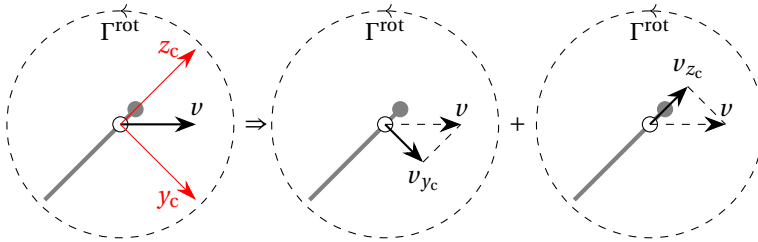

Figure 2.7: Decomposition of the coupling effect between the wing translation and rotation. Γ^{rot} represents the circulation induced by the wing rotation.

In this work, the aerodynamic loads contributed by the wing rotation have already been partly reflected by the pure rotation-induced load. Consequently, we have to avoid the inclusion of the pure rotational effect again in the coupling term. Due to the difficulty in analytical formulating the coupling effect between wing translation and rotation for a post-stall AOA, the coupling is qualitatively decomposed into two components as illustrated in Fig. 2.7. The influence of wing rotation on the surround fluid can be modeled as a circulation Γ^{rot} around the flapping wing. The first component in the decomposition represents the interaction between ω_{x_c} and the projection of v on the y_c axis. For a plate translating at an AOA of 90°, a smaller rotational turbulence will not dramatically change the drag coefficient due to the already existing flow separation behind the plate before the turbulence occurs, which implies that this coupling effect is also marginal. For this reason, this component is excluded from the coupling load. Consequently, the second component in Fig. 2.7 will be used to calculate the coupling load in our quasi-steady model. This term is equivalent to a plate uniformly rotating around its pitching axis at zero AOA when immersed in an incoming flow at a velocity of v_{z_c}.

It should be mentioned that the coupling term is reformulated in the proposed model as compared to the traditional formula in Eq. 2.20. The key difference is that the new

formula used for the coupling term is derived based on the condition that the plate uniformly rotates around its pitching axis in an incoming flow. This condition should be applied as a result of the "quasi-steady" assumption. However, the formula used in most existing quasi-steady models is taken from the work of Fung (1993) where the plate is assumed to oscillate around its equilibrium position in a harmonic way. The derivation of the coupling load due to the second component in Fig. 2.7 is presented in Appendix B, where the pressure distribution on this rotating plate is obtained through constructing the acceleration potential of the surrounding fluid. The load due to the coupling effect consists of two loading terms, as in,

$$F_{y_c}^{coup} = \begin{cases} \pi\rho^f \omega_{x_c}\omega_{y_c}\left[\int_0^R \left(\frac{3}{4}-\hat{d}\right)c^2 x_c dx_c + \int_0^R \frac{1}{4}c^2 x_c dx_c\right], & \omega_{y_c} \leq 0 \\ \pi\rho^f \omega_{x_c}\omega_{y_c}\left[\int_0^R \left(\hat{d}-\frac{1}{4}\right)c^2 x_c dx_c + \int_0^R \frac{1}{4}c^2 x_c dx_c\right], & \omega_{y_c} > 0. \end{cases} \tag{2.21}$$

When $\omega_{y_c} \leq 0$, the velocity component v_{z_c} points from the TE to LE. The first term with the CP (denoted as $\hat{d}_{cp}^{coupl,I}$) at the 1/4 chord point can be regarded as a result of a rotation-induced vorticity concentrated at the 1/4 chord while satisfying the boundary condition for the downwash at the 3/4 chord, and the second term with the CP (denoted as $\hat{d}_{cp}^{coupl,II}$) at the 3/4 chord is a result of Coriolis effect experienced by the flow on a rotating wing. When $\omega_{y_c} > 0$, v_{z_c} points from the LE to TE, the coupling force is calculated by taking the TE as LE. As a consequence, the CP locations are also switched as compared to the case with $\omega_{y_c} \leq 0$.

Next, knowing the force components and corresponding locations of CP, the aerodynamic torque about the pitching axis and z_c axis due to the coupling effect can be expressed as

$$\tau_{x_c}^{coup} = \begin{cases} \pi\rho^f \omega_{x_c}\omega_{y_c}\left[\int_0^R \left(\frac{3}{4}-\hat{d}\right)\left(\frac{1}{4}-\hat{d}\right)c^3 x_c dx_c + \int_0^R \frac{1}{4}\left(\frac{3}{4}-\hat{d}\right)c^3 x_c dx_c\right], & \omega_{y_c} \leq 0 \\ \pi\rho^f \omega_{x_c}\omega_{y_c}\left[\int_0^R \left(\hat{d}-\frac{1}{4}\right)\left(\frac{3}{4}-\hat{d}\right)c^3 x_c dx_c + \int_0^R \frac{1}{4}\left(\frac{1}{4}-\hat{d}\right)c^3 x_c dx_c\right], & \omega_{y_c} > 0 \end{cases} \tag{2.22}$$

and

$$\tau_{z_c}^{coup} = \begin{cases} \pi\rho^f \omega_{x_c}\omega_{y_c}\left[\int_0^R \left(\frac{3}{4}-\hat{d}\right)c^2 x_c^2 dx_c + \int_0^R \frac{1}{4}c^2 x_c^2 dx_c\right], & \omega_{y_c} \leq 0 \\ \pi\rho^f \omega_{x_c}\omega_{y_c}\left[\int_0^R \left(\hat{d}-\frac{1}{4}\right)c^2 x_c^2 dx_c + \int_0^R \frac{1}{4}c^2 x_c^2 dx_c\right], & \omega_{y_c} > 0. \end{cases} \tag{2.23}$$

In the proposed quasi-steady model, the rotation-induced load and coupling load are superimposed to represent the whole rotational effect. It is worth mentioning that the derivation of the coupling term in Appendix B is based on the assumption that the velocity of the incoming fluid should be much higher than the rotational velocity, while for flapping wings the translational velocity is typically a few times the rotational velocity on average. This discrepancy might lead to an overestimation of the wing rotation effect since the couping effect is getting weaker with the decrease of the incoming fluid velocity. Nevertheless, the decomposition of the coupling term as shown in Fig. 2.7 reduces this discrepancy by taking the AOA into consideration which results in a decreased couping effect at the end of each half-stroke.

To give an insight into the importance of both the rotation-induced load and coupling load for the quasi-steady aerodynamic model, we compare the chordwise CP measured for a dynamically scaled hawkmoth wing (Han *et al.*, 2015) with our analytical
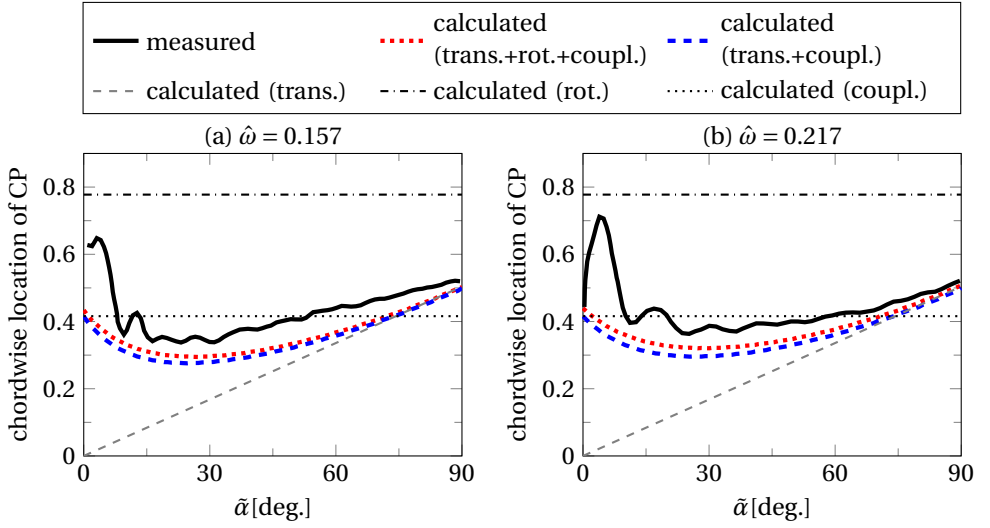
2

Figure 2.8: Comparison of the chordwise centre of pressure (CP) between measured data on a dynamically scaled hawkmoth wing (Han *et al.*, 2015) and analytical results based on the proposed model. $\hat{\omega}$ is defined as $\omega_{x_c}\bar{c}/v_{tip}$, which represents the ratio of pitching velocity to the translational velocity at the wing tip.

model. As shown in Fig. 2.8, for two cases with different ratios of pitching velocity to the translational velocity at the wing tip, the inclusion of the rotation-induced term and coupling term, particularly the later case, in the analytical model improves the agreement of the CP prediction to the measurement. The discrepancy at the initial stage is mainly due to the initial acceleration as reported by Han *et al.* (2015) which was not considered in the analytical results. Even though small discrepancies do exist for moderate AOA, to our knowledge it is the first quasi-steady model that is able to predict the chordwise CP location to this accuracy without relying on any empirical data.

ADDED-MASS LOAD

When flapping wings conduct reciprocating movements, the fluid surrounding the wings will be accelerated or decelerated depending on its position relative to the wing. This effect is most noticeable during the stroke reversal phases. At the same time, the accelerated fluid imposes a reaction on the flapping wings. This reaction can be modeled by the added-mass coefficients multiplied by the acceleration of flapping wings with a direction opposite to the acceleration direction of the wing. The added-mass coefficients for some 2D bodies with simple motions have been studied thoroughly with potential flow theory (Newman, 1977, Brennen, 1982). Therefore, we will use them directly in the added-mass load calculation with the help of the BEM.

Conventionally, we denote the directions of translational motions along axes y_c and z_c of a wing strip as the "2" and "3" directions and the rotation around x_c as the "4" direction. The parameter m_{ij} is used to represent the load induced by the added-mass

effect in the i direction due to a unit acceleration in the j direction. Since the thickness of flapping wings studied and the viscous drag are negligible, all the added-mass coefficients related to the motion in the "3" direction are ignored. Therefore, for a wing strip with chord length c, unit width and its pitching axis with a normalized offset $\hat{d}$ from the LE, the matrix of added-mass coefficients can be expressed as

$$\boldsymbol{M} = \begin{bmatrix} m_{22} & m_{24} \\ m_{42} & m_{44} \end{bmatrix} = \frac{\pi}{4} \rho^{\mathrm{f}} c^2 \begin{bmatrix} 1 & c(1/2 - \hat{d}_0) \\ c(1/2 - \hat{d}_0) & \frac{1}{32} c^2 + c^2 (1/2 - \hat{d}_0)^2 \end{bmatrix}. \tag{2.24}$$

Subsequently, the loads due to added-mass effect can be calculated by

$$\left[F_{y_c}^{\mathrm{am}}, \tau_{x_c}^{\mathrm{am}} \right]^{\mathrm{T}} = -\int_0^R \boldsymbol{M} \left[a_{y_c}, \alpha_{x_c} \right]^{\mathrm{T}} dx_c, \tag{2.25}$$

where a_{y_c} is the translational acceleration in the y_c direction and α_{x_c} is the rotational acceleration around the x_c direction. The total torque about the z_c axis can be easily calculated by integrating along the span. Additionally, it can be found that the centers of pressure induced by the translational and rotational motion, denoted as $\hat{d}_{\mathrm{cp}}^{\mathrm{am,I}}$ and $\hat{d}_{\mathrm{cp}}^{\mathrm{am,II}}$, are located at the half and $(9 - 16\hat{d})/(16 - 32\hat{d})$ chord, respectively.

WAGNER EFFECT

For a wing immersed in an incompressible fluid with a small AOA, Wagner (1925) proposed that the bound circulation around it does not immediately reach its steady-state value if it starts impulsively from rest to a uniform velocity. Instead, the corresponding circulatory force increases slowly to its steady-state value according to the Wagner's function. This Wagner effect was experimentally confirmed by Walker (1931) at $Re = 1.4 \times 10^5$. Sane (2003) attributed it to two reasons: (1) Kutta condition takes time to establish, (2) TEVs are generated and shed gradually. For an immediately started translating plate at two different post-stall AOAs (15° and 45°), an experiment at $Re = 3 \times 10^4$ conducted by Ford & Babinsky (2014) indicates that the increase of circulation surrounding the plate shows a good agreement with the circulation growth proposed by Wagner (1925), although the circulation is dominated by the LEV instead of the bound circulation. However, there is no strong evidence showing that the Wagner effect has a noticeable influence on wings translating at post-stall AOAs in the intermediate Re regime ($10 < Re < 1000$) (Dickinson & Götz, 1993). Especially, for the study of aerodynamics of insects flights, the Wagner effect is generally ignored due to the rapidly formed LEV as a result of high AOAs over the entire stroke and low Reynolds numbers.

Apparently, there is no standard yet to determine if the Wagner effect has to be included or not, and the decision has to be made based on both Re and the type of wing motion. In this work, if the Wagner effect is included, all the circulatory loads will be multiplied by an approximate formula of Wagner's function given by Jones (1940),

$$\Phi(t^*) = 1 - 0.165 e^{-0.0455 t^*} - 0.335 e^{-0.300 t^*}, \tag{2.26}$$

where t^* is a non-dimensional quantity defined as the number of semi-chords the wing has traveled.

2.3. MODEL VALIDATION

To validate the capability of the proposed quasi-steady model to estimate the aerodynamic loads and the passive pitching motion, we show two validations. The first one uses a pitching-up plate while sweeping around an axis (sweeping-pitching plate). This validation allows us to study the contribution of the wing rotational effect to the aerodynamic loads in the absence of the complicated reciprocating motion. The second validation studies the passive pitching motion and aerodynamic forces generated by a flapping wing, and this study helps to estimate the feasibility and accuracy of the proposed model when applied to real flapping wings. The latter involves more complex kinematics and unsteady aerodynamics as compared to the first test case. These two validation cases differ a lot in the Reynolds number.
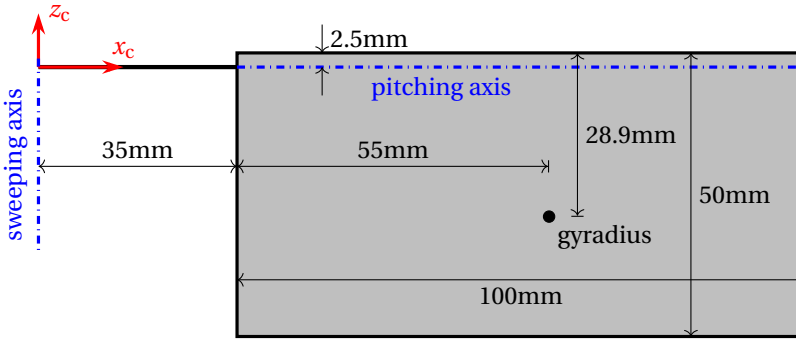
2.3.1. SWEEPING-PITCHING PLATE

Figure 2.9: Dimensions of the plate used by Percin & van Oudheusden (2015).

This validation is based on the experiment carried out by Percin & van Oudheusden (2015), in which the aerodynamic force and torque acting on a sweeping-pitching plate were measured. This rectangular plate has a chord length of 50 mm, a span length of 100 mm, and is connected to a drive mechanism with a bar of 35 mm, as shown in Fig. 2.9. This results in an aspect ratio ($\mathcal{R}$) of 2 for the plate ($\mathcal{R}_{\text{plate}}$) and a nominal value of 3.65 for the entire wing ($\mathcal{R}_{\text{nom}}$). Obviously, this wing platform differs from both fixed wings of airplanes and insect wings which generally show a steady change of chord length along the span. The effective value of $\mathcal{R}$ ($\mathcal{R}_{\text{eff}}$) is supposed to be between $\mathcal{R}_{\text{plate}}$ and $\mathcal{R}_{\text{nom}}$, but has to be determined by experiments. Here, we use the mean of $\mathcal{R}_{\text{plate}}$ and $\mathcal{R}_{\text{nom}}$ (i.e., $\mathcal{R}_{\text{eff}} = 2.83$). The distance from the pitching axis to the leading edge (LE) is a constant and equal to 2.5 mm, which leads to $\hat{d} = 0.05$.

The radius of gyration (gyradius) of the entire wing is 90 mm from the sweeping axis. It is selected as the radius for calculating the reference velocity such that the force and torque coefficients of the 3D wing based on this velocity are equal to the corresponding coefficients used for the BEM in the proposed quasi-static model. However, in the experiment, Percin & van Oudheusden (2015) used the reference velocity at the chord with a distance of 1/4 plate span from the wing tip, which gives a larger radius than that in our

definition. For a fair comparison, the force and torque coefficients from Percin & van Oudheusden (2015) are adapted to agree with our definition.
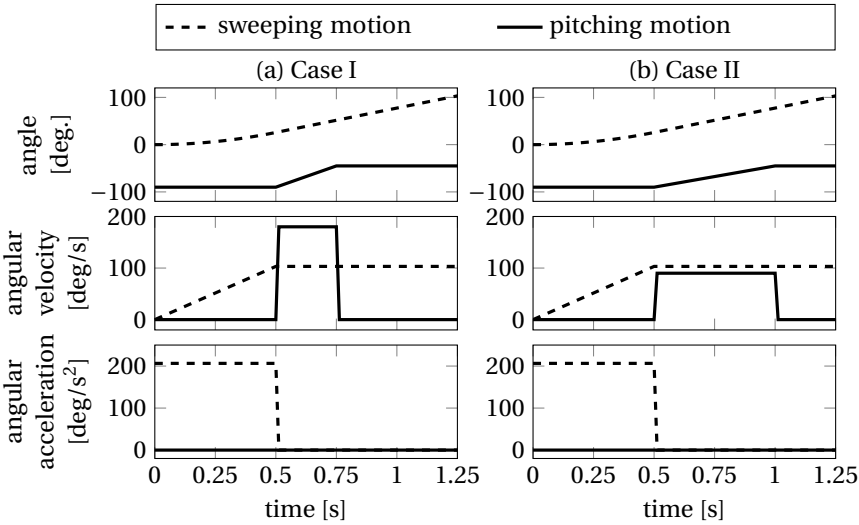

Figure 2.10: Kinematics of the plate for two cases in the same sweeping motion but different pitching motion.

The kinematics of the sweeping-pitching plate is plotted in Fig. 2.10. The sweeping motion is initiated by a stationary acceleration from rest to a sweeping angular velocity about 103 deg/s with zero AOA over the first half second. This is followed by a period of steady sweeping and pitching-up motion. The plate pitches from 0° to 45°, within 0.25 seconds (Case I) and 0.5 seconds (Case II). Thereafter, the plate keeps sweeping at a stationary AOA of 45°. For both cases, the aerodynamic force and torque about the pitching axis are simulated numerically for the first 2 seconds.

The calculated and measured results for both cases are shown in Figs. 2.11 and 2.12. For both cases, the lift, drag and torque data from the experiments are plotted in thick lines in black. It should be noted that (1) the drag in this validation is defined in the direction opposite to the translational velocity of the plate while the drag shown in the rest of this chapter is defined as the component of aerodynamic force on the y_i axis in the inertial frame; (2) the added-mass effect is not considered in the numerical results shown in Figs. 2.11 and 2.12 since the acceleration information during the start and stop phases of pitching motion is unknown. The history of experimentally measured loads can be divided into three phases: (1) before 0.5 seconds, zero lift and a little amount of drag and torque due to the viscous drag on the plate surface can be found; (2) from 0.5 to 0.75 seconds for Case I and to 1 second for Case II, a dramatic increase of loads are reported due to the contribution of the wing rotation and translation; (3) from 0.75 seconds for Case I and 1 second for Case II to 2 seconds, relative steady load histories are shown due to the steady wing sweeping at the stationary AOA. During the first phase, no aerodynamic loads are obtained by the proposed model since the viscous drag is assumed to be
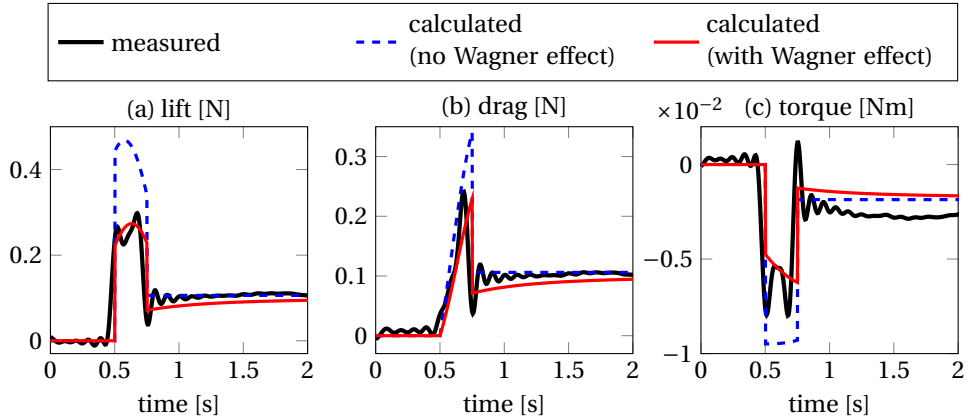
2

Figure 2.11: Comparison of lift, drag and aerodynamic torque about pitching axis for Case I without considering the added-mass effect.
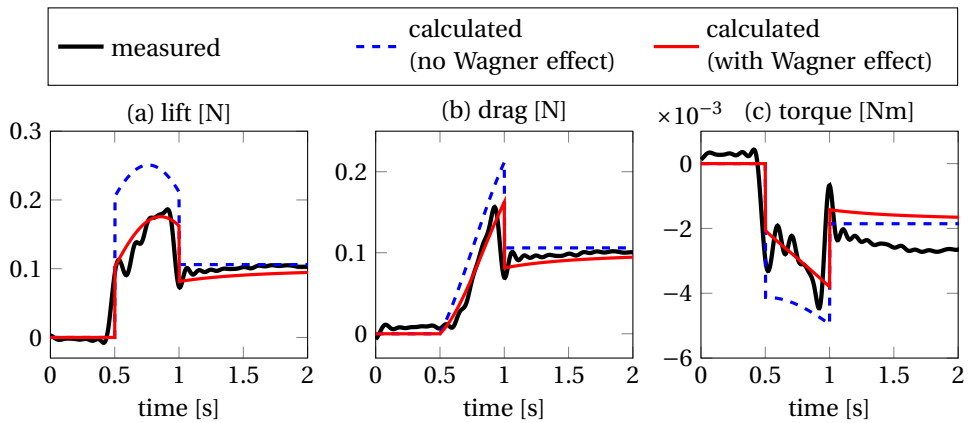

Figure 2.12: Comparison of lift, drag and aerodynamic torque about pitching axis for Case II without considering the added-mass effect.

negligible. At the beginning of the second phase, the rapid increase trend and the amplitudes are well captured by the proposed analytical model while considering the Wagner effect. In contrast, the loads without the Wagner effect apparently overestimate the peak values. If we compare the loads during the second phase to the loads after the pitching motion stops, it is obvious that the increments of the aerodynamic lift, drag and torque due to the wing rotation are dramatic. When the plate stops pitching up, the magnitudes of the drop of lift and drag are all successfully predicted by the proposed quasi-steady model when considering the Wagner effect. The discrepancy of the aerodynamic torque for both cases can result from the slightly underestimated centre of pressure as shown in Fig. 2.8. Based on the comparisons of calculated and measured results for both cases, it can be concluded that the estimations with the Wagner effect show much better agree-
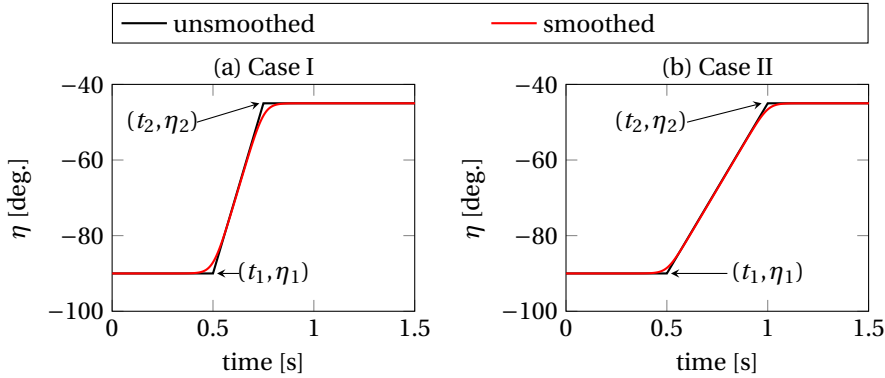
Figure 2.13: Comparison of unsmoothed and smoothed pitching motion for both cases. η_1 and η_2 are the pitching angles before and after the pitching motion occurring at t_1 and t_2, respectively.

ment to the measurements for all the lift, drag and torque histories and for both cases. This can be explained by the fact that both the Reynolds number ($Re = 1 \times 10^4$) and the kinematics satisfy the conditions where the Wagner effect should be considered.

The sharp peaks shown in the experimental data at the transitions are attributed to the added-mass effect during the start and stop of the pitching motion (Percin & van Oudheusden, 2015). The pitching motion shown in Fig. 2.10 is the ideal case where no transition time is needed to start or stop the pitching motion, which is not true in reality. However, the time required for the brushed DC motor used in the experiment to realize the transition of the wing in water is not clear. In order to quantify the acceleration in transitions, we use a continuously differentiable C^∞ function (Eldredge *et al.*, 2009) to replace the ideal pitching motion, as shown in Fig. 2.13. The new function is given by

$$\eta(t) = \frac{\eta_2 - \eta_1}{a(t_2 - t_1)} \ln \left[\frac{\cosh(a(t - t_1))}{\cosh(a(t - t_2))} \right] + \frac{1}{2}(\eta_1 + \eta_2), \tag{2.27}$$

where η_1 and η_2 are the pitching angles before and after the pitching motion which occur at t_1 and t_2, respectively. The parameter a controls the transition time and is set to 40 here to minimize the phase shift between calculated and measured loads. Results obtained from our quasi-steady model including the added-mass effect are also compared with measured data in Figs. 2.14 and 2.15. Apparently, most of the peaks and valleys of the load histories are well captured. The mismatch just before the pitching motion stops might be a result of the imperfection of the hypothetical smoothed pitching motion.

2.3.2. FLAPPING WING
To further validate the proposed model, we use a flapping wing as another test case which is operated at a much smaller Reynolds number (about 100) than that of the sweeping-pitching plate. This experimental measurement was conducted by Whitney & Wood (2010) to obtain the passive pitching motion and lift production of an artificial wing which mimics the wing of Eristalis tenax (dronefly).
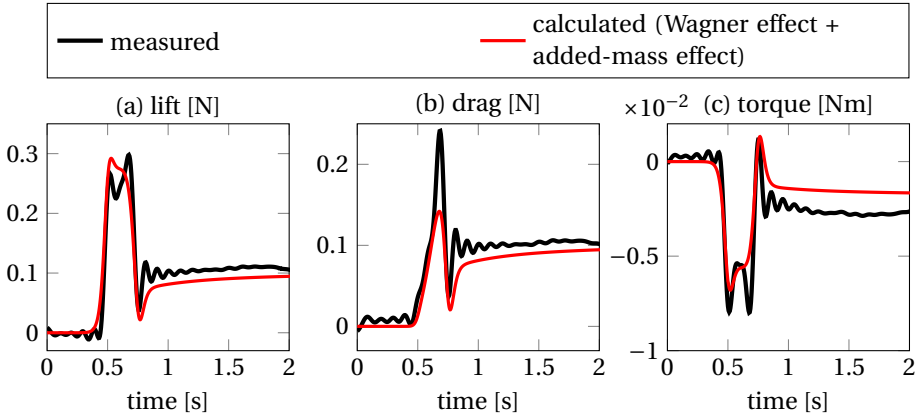
Figure 2.14: Comparison of lift, drag and aerodynamic torque about pitching axis for Case I when added-mass effect is considered based on the smoothed pitching motion.
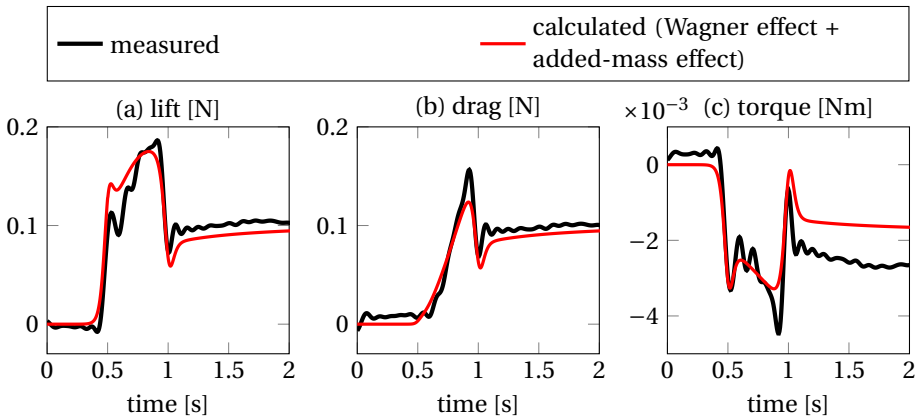
Figure 2.15: Comparison of lift, drag and aerodynamic torque about pitching axis for Case II when added-mass effect is considered based on the smoothed pitching motion.

As shown in Fig. 2.16, the wing span is 15 mm, and the spanwise wing area distribution which can be quantified by the length of all the chordwise strips is described by the Beta probability density function. The first and second radius of moment of area of the wing are equal to 0.5 and 0.56, respectively, and they are taken as the mean and standard deviation of the Beta probability density function. The pitching axis is located at a distance of 0.73 mm from the straight portion of its leading edge (LE). Due to the variation of the chord length along the span, the normalized local distance between the LE and pitching axis $\hat{d}$ changes from the wing root to tip. The wing platform is connected to the drive bar that is located above the wing root with an elastic hinge (polyimide film) of 1.8 mm wide, 70 μm long and 7.6 μm thick.

Figure 2.16: Wing platform used by Whitney & Wood (2010).

The passive pitching motion and the net force that consists of both the aerodynamic lift and wing inertia were measured by Whitney & Wood (2010). The aerodynamic torque about the pitching axis could not be measured by their setup directly. Therefore, the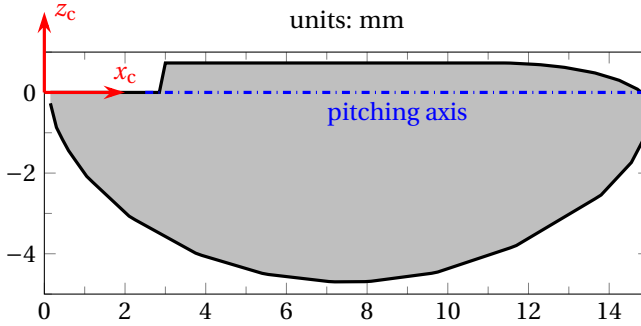 capability of our model to estimate the aerodynamic torque has to be validated indirectly by comparing the calculated and measured passive pitching motions. The pitching motion is jointly determined by the hinge stiffness at the wing root, the wing inertia and the aerodynamic torque about the pitching axis. The equation of motion that governs the passive pitching motion is derived in Appendix C. The hinge stiffness can be modeled as a linear rotational spring (Howell, 2001), and the related inertial terms have been measured by Whitney & Wood (2010). Consequently, the accuracy of the predicted passive pitching motion mainly depends on how well the aerodynamic torque estimation is.

Two cases of flapping kinematics with different ratios of upstroke-to-downstroke duration (u/d), $u/d = 0.79$ for Case I and $u/d = 0.62$ for Case II, were studied in the experiments. Rather different passive pitching motions (Figs. 2.17 and 2.18) and lift force histories (Fig. 2.21) were reported.

In our simulations, the Wagner effect is not included due to the flapping kinematics and low Re, both of which reduce the influence of Wagner effect. The contribution of the small heaving motion is considered. Figures 17 and 18 show the calculated pitching motion when excluding the coupling loads, the rotation-induced loads and using the full model. For both cases, it can be seen that the passive pitching motion predicted by the proposed model that includes all the four loading terms shows best agreement to the experimental data. The inclusion of the rotation-induced loads due to pure wing rotation and the coupling loads between wing translation and rotation improves the prediction of the passive pitching motion by introducing more damping. From the plot of the total aerodynamic torque and its components for both cases as shown in Fig. 2.19, it can be clearly seen that (1) the rotation-induced loads and the coupling loads dominate the aerodynamic torque during the wing reversals; and (2) the coupling between the wing translation and rotation provides additional aerodynamic torque and thus, damping on the wing all over a flapping cycle. Although the wing reversals predicted by our model start slightly earlier than that reported by the experimental data, the pitching amplitudes and the phase shift from the sweeping motion (measured from peak to peak) are quite close, especially for Case I.
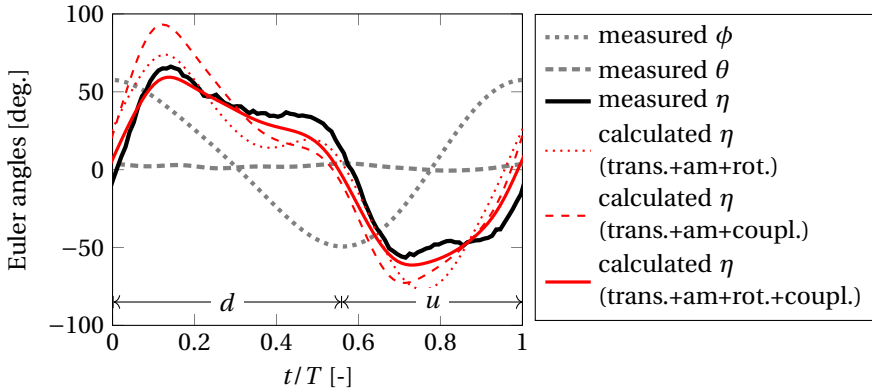
Figure 2.17: Comparison of passive pitching motion between measured and calculated results for case I. Three calculated results correspond to different combinations of the four terms in our quasi-steady model. "d" and "u" indicate the downstroke and upstroke, respectively.
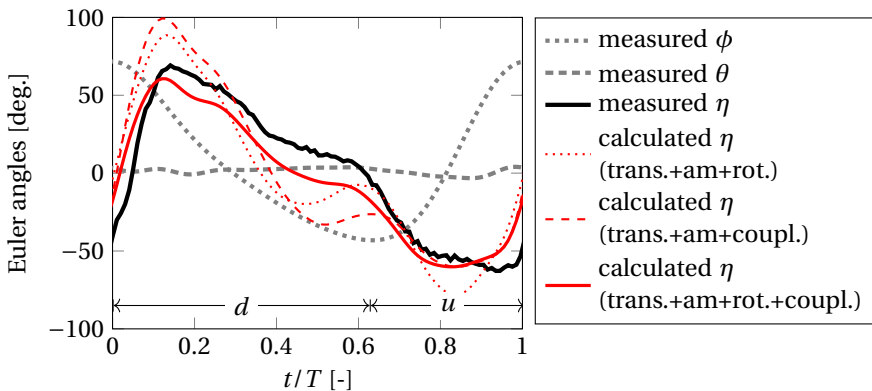
Figure 2.18: Comparison of passive pitching motion between measured and calculated results for case II. Three calculated results correspond to different combinations of the four terms in our quasi-steady model.

Whitney & Wood (2010) also compared the predicted passive pitching motion based on their quasi-steady model with the experimental data. As shown by Table 2.1, their model includes the loads resulting from wing translation, pure rotation and added-mass effect. In their simulation, the translational lift coefficient and rotational damping coefficient were tuned to achieve best agreements with experimental results. They used the centre of pressure (CP) measured on a dynamically scaled model Drosophila Dickson *et al.* (2006) in their simulation. By comparing the passive pitching motion calculated by their quasi-steady model with different combinations of the three components, they argued that the damping due to pure rotation is important but the added-mass effect is not always helpful to reduce the discrepancy with measured results. For Case I, they
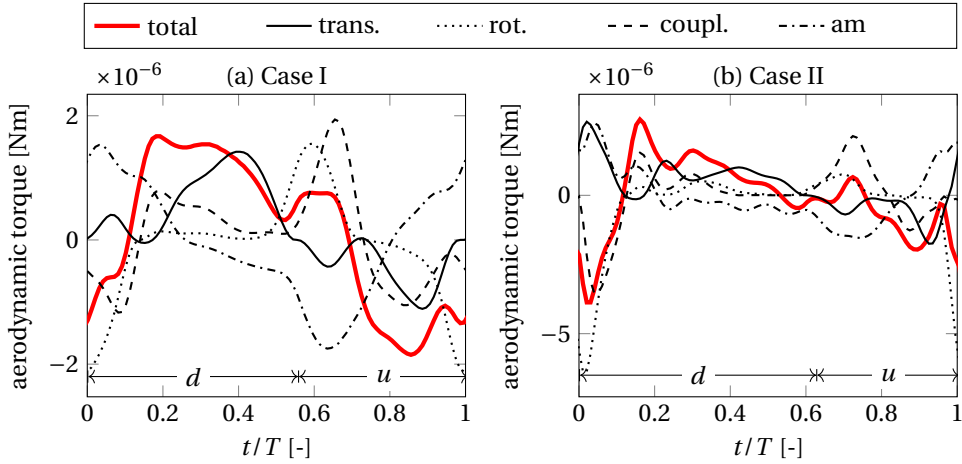
Figure 2.19: Total aerodynamic torque and its components induced by the wing translation, rotation, the coupling term as well as the added-mass effect for both cases.

showed both the calculated passive pitching motion with and without considering the added-mass effect, while for Case II, they only showed the result without considering the added-mass effect. These results are compared with the passive pitching motion predicted by the proposed model in this work as well as the experimental data in Fig. 2.20. It can be seen that without help from any empirical parameters our quasi-steady model still can give comparable passive pitching motion to the seemingly best results from the model of Whitney & Wood (2010) which are based on careful tuning of some parameters. Our model even gives a better prediction of the amplitude of the passive pitching motion.

The lift force measured by Whitney & Wood (2010) is the summation of the aerodynamic and inertial forces of the wing. In Fig. 2.21, two types of calculated forces obtained by the proposed model in this work are presented for both cases. One is based on the fully measured kinematics while the other is based on the kinematics with the measured sweeping and heaving motion but calculated passive pitching motion. It is clear to see that with fully measured kinematics our quasi-steady model gives a rather good prediction of the force histories for both cases except for short periods of overestimation during the upstrokes. The overestimation can be explained by two reasons. First, the shorter duration of upstrokes compared to downstrokes might lead to more complex unsteady flow phenomenon (e.g., Wagner effect) which is a challenge for our quasi-steady model to capture. Second, the angular velocity and acceleration of three Euler angles are calculated based on the corresponding displacements which are fitted from the measured data. This might lead to inaccurate kinematic information, especially the acceleration, which influences the added-mass effect. When the calculated passive pitching motion is used, the overestimation is slightly larger as a result of the discrepancy between calculated and measured pithing motion. But the characteristics of the force histories are still successfully captured, especially during the downstroke.
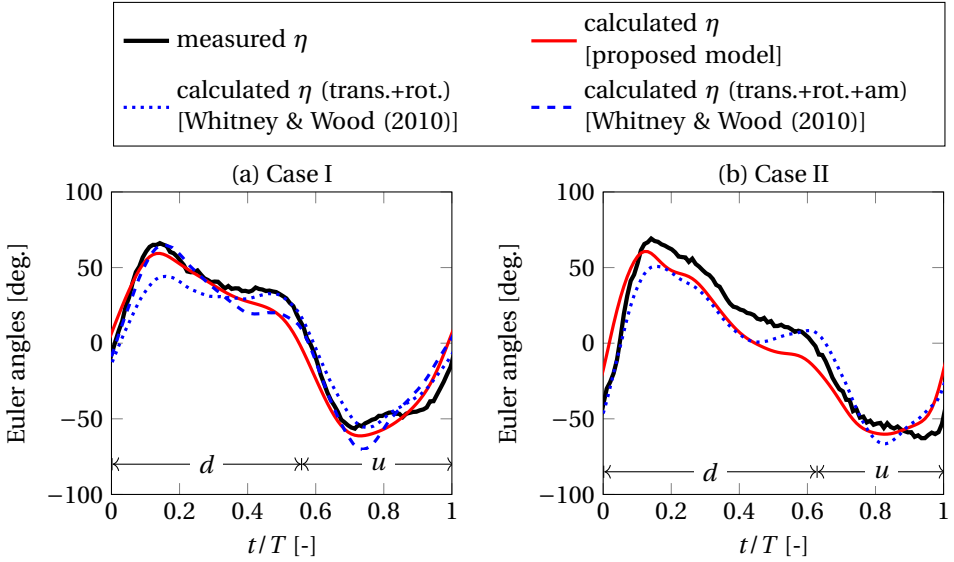
Figure 2.20: Comparison of the passive pitching motion predicted by the proposed quasi-steady model and the model of Whitney & Wood (2010) for both cases.
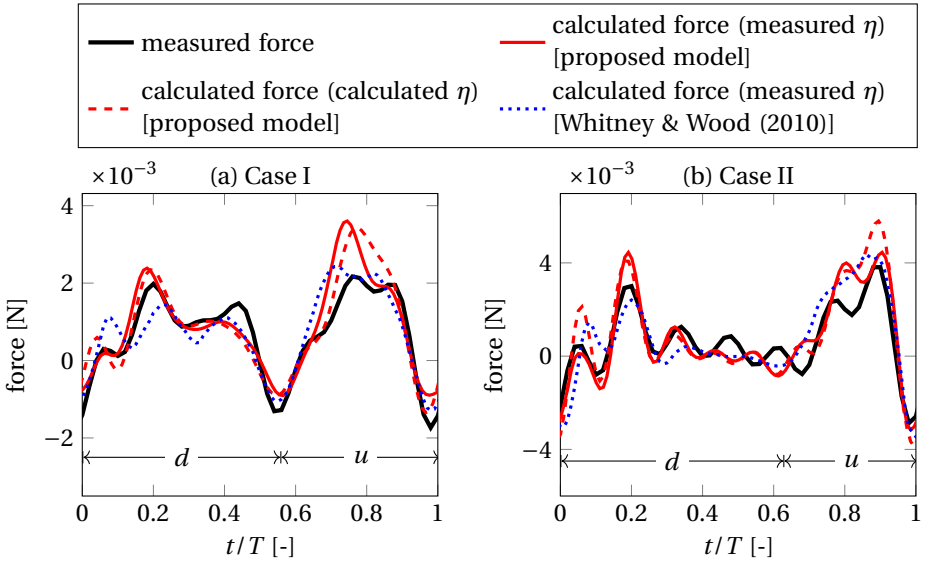

Figure 2.21: Comparison of the force histories for both cases between experimental data and calculated results based on both the proposed quasi-steady model and the model from Whitney & Wood (2010).

In Fig. 2.21, we also show the predicted force history obtained by Whitney & Wood

(2010). In their simulation, the pure rotation effect is ignored during the force calculation although included in the aerodynamic torque estimation for calculating the passive pitching motion. Even though the careful selection of different terms and tuning of empirical parameters do improve the agreement of lift prediction with measured data, their model is less predictive for arbitrary flapping wings compared to our quasi-steady model which does not rely on any empirical data.

The measured average lift forces are 71.6 mg for Case I and 71.2 mg for Case II, respectively. With the proposed quasi-steady model, the average lift based on the fully measured kinematics is 90.9 mg and 81.6 mg for two cases, respectively. Due to the increase of discrepancy between measured and calculated pitching motion, the average lift obtained based on the calculated pitching motion is 89.0 mg for Case I and 94.4 mg for Case II. In addition to the error of the predicted passive pitching motion, this overestimated average lift force might be attributed to the fact that the lift is very sensitive to the wing dimensions. For example, if we decrease the wing span by 1 mm while keeping the aspect ratio, the calculated average lift forces based on measured kinematics are reduced to 75.1 and 66.7 mg for the two cases.

Without using any empirical parameters or selectively choosing different terms, our quasi-steady model is still able to give good predictions to the passive pitching motion. Compared to the results obtained by the quasi-steady model proposed by Whitney & Wood (2010), the proposed model can give a comparable or slightly better prediction of the passive pitching motion. This implies that our model is more predictive for evaluating the aerodynamic performance of flapping wings in passive pitching motion. Admittedly, limited by the inherent drawbacks of the quasi-steady assumption, the unsteady effects, such as wake capture effect, the Wagner effect and the spatial movement of the LEV on the wing surface, can not be reflected. This might be another reason of the discrepancy of the passive pitching motion and force history between calculated and experimental results.

2.4. CONCLUSIONS

For wings performing translational and rotational motion simultaneously, particularly for flapping wings, we proposed a predictive quasi-steady aerodynamic model. This model is capable of predicting both the aerodynamic force and torque, and it also provides better solutions to three issues which have not been addressed completely by existing quasi-steady models. First is the inconsistency of compositions of existing quasi-steady models, which is eliminated by comprehensively including contributions from wing translation, rotation, their coupling and the added-mass effect in the proposed model. Second is the overall contribution of the wing rotation to the total aerodynamic loads and the corresponding centre of pressure, both of which are required for the estimation of aerodynamic torque. We use two components, including the rotation-induced loads due to the pure wing rotation and the loads due to the coupling between wing rotation and translation, to collaboratively represent the overall contribution of the wing rotation. A new formula for the coupling load has been derived based on the condition that the plate uniformly rotates around its pitching axis in an incoming flow. This condition should be applied as a result of the "quasi-steady" assumption. However, the formula used in most existing quasi-steady models assumes that the plate oscillates around

2

its equilibrium position in a harmonic way. The importance of both components to the quasi-steady model has been shown by the fact that the damping torque excluding the contribution from either of them is far from sufficient to maintain the expected passive pitching motion. The proposed model shows excellent prediction of the centre of pressure of a dynamically scaled hawkmoth wing conducting translational and rotational motion simultaneously at different angles of attack. Third is that most existing quasi-steady models depend on empirical parameters. In contrast, the proposed model does not rely on any empirical data while it still shows a comparable accuracy on estimating the aerodynamic force, torque and the passive pitching motion as shown by the comparisons with experimental data of two test cases. This implies that the proposed model is more predictive compared to existing quasi-steady models. Therefore, the proposed quasi-steady model can be applied to the design and optimization of flapping wings.

3

OPTIMAL PITCHING AXIS LOCATION OF FLAPPING WINGS FOR EFFICIENT HOVERING FLIGHT

Flapping wings can pitch passively about their pitching axes due to their flexibility, inertia, and aerodynamic loads. A shift in the pitching axis location can dynamically alter the aerodynamic loads, which in turn changes the passive pitching motion and the flight efficiency. Therefore, it is of great interest to investigate the optimal pitching axis for flapping wings to maximize the power efficiency during hovering flight.

In this chapter, flapping wings are modeled as rigid plates with non-uniform mass distribution. The wing flexibility is represented by a linearly torsional spring at the wing root. The quasi-steady aerodynamic model introduced in Chapter 2 is used to evaluate the lift generated by such wings. Two extreme power consumption scenarios are modeled for hovering flight, i.e., the power consumed by a drive system with and without the capacity of kinetic energy recovery. For wings with different shapes, the optimal pitching axis location is found such that the cycle-averaged power consumption during hovering flight is minimized. This chapter is organized as follows. Sec. 3.1 introduces the background and motivation. The following sections start with the flapping wing modeling in Sec. 3.2 which consists of the wing area and mass distribution models as well as the kinematics model. In Sec. 3.3, the aerodynamic model and the power consumption model are introduced. Based on the optimization model described in Sec. 3.4, we investigate the optimal location of pitching axis for different wings and analyse its influences on the power efficiency during hovering flight in Sec. 3.5. Conclusions are presented in Sec. 4.5.

3.1. Introduction

There exists a great diversity of wing morphology among insects, especially from the wing shape perspective. Compared to the wing outlines of various winged-insects, the wings of most flapping wing micro air vehicles (FWMAVs) (de Croon *et al.*, 2009, Bolsman *et al.*, 2009, Keennon *et al.*, 2012, Ma *et al.*, 2013, Nguyen *et al.*, 2015) have much simpler shapes (e.g., quarter-ellipse, polygon). Although this simplification helps to decrease the design complexity and fabrication difficulty, the effect of wing shape on the flapping flight performance, particularly on the energy-efficiency, can not be completely ignored.

Wing shape determines the area distribution which can be further decomposed into distributions in the span and chord directions. Aerodynamic loads on flapping wings roughly increase quadratically with the velocity and, thus, are sensitive to the spanwise area distribution (SWAD). As a result, its influence on flapping wing performance has been extensively studied in the past. For instance, Ansari *et al.* (2008) investigated the influence of the spanwise wing area distribution and aspect ratio on the lift generation and power efficiency using an unsteady aerodynamic model (Ansari, 2004). Recently, Shahzad *et al.* (2016) conducted similar investigations using a computational fluid dynamics (CFD) method. They both showed that wings with more outboard area and higher aspect ratio generate higher lift but also consume more power. This is because the lift and power scale with the square and cube of flapping velocity, respectively. Optimal wing shapes have also been studied in literature using quasi-steady aerodynamic models. Typically, the total lift force is constrained in these studies. By keeping the wing aspect ratio constant, Wang *et al.* (2013) showed that flapping wings with more outboard area can have better performance, i.e., higher lift generation or less power consumption. Stewart *et al.* (2013) found that the optimal wing shape which provides maximal thrust for forward flight tends to push much of the planform away from the wing root. Wang *et al.* (2014*a*) investigated the optimal wing shape for energy-efficient hovering flight in passive pitching motion while keeping the total wing area constant. A wing planform with a low aspect ratio, similar to butterfly wings, was obtained.

In contrast, the influence of chordwise area distribution (CWAD) on flapping flight performance has been less studied. CWAD determines the inertia and aerodynamic loads a wing needs to overcome when pitching about its pitching axis. Particularly when the wing pitches passively due to its flexibility and the inertial and aerodynamic loads CWAD directly determines the passive pitching behavior, including the amplitude, the phase lag from sweeping motion, and its deviation from a harmonic motion. Passive pitching can be found for both insects (Ennos, 1989, Combes & Daniel, 2003, Bergou *et al.*, 2007, Ishihara *et al.*, 2009) and FWMAVs (Wood, 2008, de Croon *et al.*, 2009, Keennon *et al.*, 2012, Ma *et al.*, 2013). Particularly for FWMAVs, the passive pitching motion is preferred in order to simplify the drive mechanism. Consequently, the location of the pitching axis becomes an important design aspect for artificial wings in order to achieve energy-efficient flight for FWMAVs.

This work aims to find the optimal pitching axis location for flapping wings with passive pitching motion. Flapping wings are modeled as rigid plates with non-uniform mass distribution. The wing flexibility is represented by a linearly torsional spring at the wing root, which is commonly used for the wing design (Whitney & Wood, 2010, Wang *et al.*, 2014*a*). The predictive quasi-steady aerodynamic model presented in Chapter 2 is used

to evaluate the lift generated by such wings. Two extreme power consumption scenarios are modeled for hovering flight, i.e., the power consumed by a drive system with or without the capacity of kinetic energy recovery. In this study, hovering flight is considered not only because it is generally more energy-consuming compared to forward flight (Dudley, 2002), but also it is a required and an important capability for FWMAVs.

3.2. FLAPPING WING MODELING

3.2.1. AREA DISTRIBUTION

Wing area distribution is decomposed into spanwise area distribution (SWAD) and chordwise area distribution (CWAD).

Ellington (1984a) proposed that the SWAD of insect wings can be approximately described by Beta probability density function (BPDF). The mean and standard variance of the BPDF are represented by the dimensionless radii of the first and second spanwise moment of area, which are denoted as $\hat{r}_{s_1}$ and $\hat{r}_{s_2}$, respectively. They are defined as

$$\hat{r}_{s_1} = \frac{1}{SR} \int_0^R cr\,dr \quad \text{and} \quad \hat{r}_{s_2} = \sqrt{\frac{1}{SR^2} \int_0^R cr^2\,dr}, \tag{3.1}$$

where R, c and S are the wing span, chord length and the total area, respectively. Furthermore, $\hat{r}_{s_1}$ was correlated with $\hat{r}_{s_2}$ by the relation $\hat{r}_{s_2} = 0.929\hat{r}_{s_2}^{0.732}$ by Ellington (1984a). In contrast, for wings of FWMAVs, the SWAD is often simplified to reduce the modeling and fabrication complexity. For instance, flapping wings with rectangular (Seshadri *et al.*, 2013), quarter-ellipsoidal (Keennon *et al.*, 2012), triangular (Chaudhuri *et al.*, 2013) and polygonal (de Croon *et al.*, 2009) shapes have been adopted.

Compared to the SWAD, the CWAD was less studied for two reasons. First, successful take-off and stable flight are still the research objectives of most FWMAVs. Thus, people are more interested in the lift and thrust generation which are more sensitive to the wing SWAD. Second, the influence of the CWAD on flight performance is more pronounced for wings that pitch passively when compared to wings with fully prescribed kinematics, and the latter is more frequently used. In order to model the CWAD, we introduce a dimensionless parameter $\hat{d}$ which is defined as the local-chord-normalized distance from the leading edge (LE) to the pitching axis (PA). The parameter $\hat{d}$ is formulated as a linear function of the spanwise radius r, i.e.,

$$\hat{d}(r) = \frac{r}{R}(\hat{d}_t - \hat{d}_r) + \hat{d}_r, \quad 0 \leq r \leq R, \tag{3.2}$$

where R is the wing span, and $\hat{d}_r$ and $\hat{d}_t$ represent the values of $\hat{d}$ at the wing root and the tip, respectively. When $\hat{d}_r = \hat{d}_t = 0$, the wing takes its straight LE as the pitching axis, which has been widely adopted for most FWMAVs (de Croon *et al.*, 2009, Bolsman *et al.*, 2009, Keennon *et al.*, 2012, Ma *et al.*, 2013, Nguyen *et al.*, 2015). When $\hat{d}_r = \hat{d}_t = 0.5$, the wing planform is symmetric about its PA, which has been used as a simplified wing model for studying the optimal kinematics by Berman & Wang (2007). In contrast, the PA of insect wings is generally located between the LE and the mid-chord line. The difference of the PA location between artificial and insect wings inspired us to investigate the
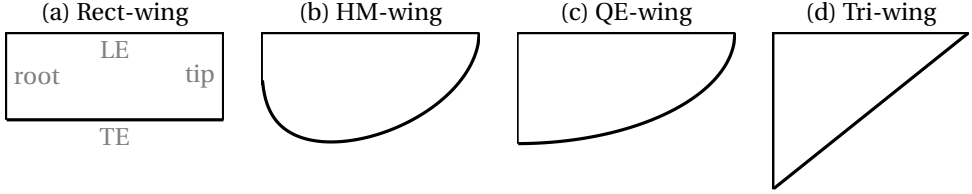
(a) Rect-wing	(b) HM-wing	(c) QE-wing	(d) Tri-wing

Figure 3.1: Four traditional wings with the same straight leading edge (LE) but differ-ent trailing edges (TEs). The shape of the TE is determined by the spanwise area distributions (SWADs). The SWADs of these wings correspond to the rectangular wing (Rect-wing), the hawkmoth wing (HM-wing), the quarter-ellipsoidal wing (QE-wing) and the triangular wing (Tri-wing). The value of $\hat{r}_{s_1}$ decreases from left to right.

influence of the PA on the flight efficiency and find the optimal PA location for artificial wings.

In this work, four traditional wings with straight leading edges but different spanwise area distributions (SWADs) are studied. As shown in Figs. 3.1 (a) - (d), the SWADs of these wings are identical to the rectangular wing (Rect-wing), the hawkmoth wing (HM-wing), the quarter-ellipsoidal wing (QE-wing) and the triangular wing (Tri-wing), respectively. However, the shapes of these wings can vary significantly if the CWAD is changed. The resulting effect on the flight performance is still unclear and will be studied in this work. To facilitate the comparison, all wings have the same wing span and surface area S.

3.2.2. MASS DISTRIBUTION

Similar to the wing area distribution, the wing mass distribution is also characterized by the spanwise mass distribution (SWMD) and the chordwise mass distribution (CWMD).

Span wise, the dimensionless radii of the first and second moment of inertia, which are denoted as $\hat{r}_{m_1}$ and $\hat{r}_{m_2}$, respectively, are generally used to reflect the MD. According to studies on different species of insects (Ellington, 1984a, Betts & Wootton, 1988, Dudley & Ellington, 1990, Willmott & Ellington, 1997b), $\hat{r}_{m_1}$ typically ranges from 0.2 to 0.5, and $\hat{r}_{m_2}$ from 0.3 to 0.6. Combes & Daniel (2003) measured the spanwise bending stiffness variation from the root to the tip of a hawkmoth wing (Manduca sexta) and a dragon-fly wing (Aeshna), and found that the variation can be approximated by an exponential decline. The spanwise stiffness is related to the cross-sectional profile in chordwise di-rection and proportional to the term $c(r)\,t_m^3(r)$, where c and t_m are the chord length and the maximal thickness of the cross-section. Therefore, if the variation of the chord length is ignored, the change of t_m along the span can be approximately described by an expo-nential function

$$t_{\mathrm{m}}(r) = \lambda_1 e^{\lambda_2 r}, \qquad 0 \leqslant r \leqslant R, \tag{3.3}$$

where λ_1 and λ_2 are two parameters to be determined. In this work, we assume that the wing is made of the same material with a density ρ^{w}, which implies that the MD is equivalent to the wing thickness variation. Therefore, the function of t_{m} can reflect the SWMD if the wing has the same cross-sectional profile along the span.

The CWMD is also important since it determines the pitching inertia and, thus, the

(a) kite profile   (b) uniform profile

Figure 3.2: Schematic diagram of two cross-sectional profiles that are used to describe the chordwise mass distribution. The maximal thickness of the cross-section is denoted as t_m. LE and TE represent the leading edge and trailing edge, respectively.

passive pitching motion. Due to the lack of knowledge on the CWMD of insect wings, we assume two different cross-sectional profiles, as shown in Fig. 3.2. The first is a kite profile, i.e., the thickness (or mass) of an arbitrary cross-section increases linearly from zero at both the leading and trailing edges to the maximal value t_m at the pitching axis location. The second is a uniform thickness along the chord.

Based on the proposed SWMD and CWMD models, the mass distribution of an arbitrary wing can be quantified. When the wing mass m^w and the moment of inertia are known, the unknown parameters λ_1 and λ_2 in Eq. 3.3 can be determined by solving following system of equations

$$\int_0^R \rho^w \gamma \lambda_1 e^{\lambda_2 r} c \, dr - m^w = 0, \tag{3.4a}$$

$$\int_0^R \rho^w \gamma \lambda_1 e^{\lambda_2 r} c r^2 \, dr - m^w \hat{r}_{m_2}^2 = 0, \tag{3.4b}$$

where the value of γ depends on the CWMD ($\gamma = 1/2$ for the kite profile and $\gamma = 1$ for the uniform profile). It should be noted that the spanwise radii of the first and second moment of inertia (i.e., $\hat{r}_{m_1}$ and $\hat{r}_{m_2}$) do not change with the value of γ.

To validate the proposed mass distribution model, we use it to describe the wing mass distribution of four insects, including a hawkmoth, a hoverfly, a bumblebee and a dronefly. The wing mass and the dimensionless spanwise radii of the first and second moment of inertia (i.e., $\hat{r}_{m_1}$ and $\hat{r}_{m_2}$) of these insects have been measured in literature (Ellington, 1984a, Willmott & Ellington, 1997b). The values of λ_1 and λ_2 for each insect wing are determined using Eqs. 3.4. Thus, the mass distribution over the entire wing is known. Then, the values of $\hat{r}_{m_1}$ are calculated and compared with the measured values, as shown in Table 3.1. The comparison shows that the calculated $\hat{r}_{m_1}$ deviates from the measured value by less than 6.9% for all the four wings, which implies that the proposed model provides a good representation of the SWMD of insects wings.

3.2.3. KINEMATICS
Two frames are introduced to describe the flapping kinematics of a rigid wing, i.e., the inertial frame $x_i y_i z_i$ and the co-rotating frame $x_c y_c z_c$, as shown in Fig. 3.3. The inertial frame is fixed at the wing joint. The x_i axis coincides with the projection of the leading edge on the horizontal stroke plane while the wing is at rest at the middle stroke. The z_i axis is perpendicular to the stroke plane, and the y_i axis is defined by the right-hand-rule. The co-rotating frame rotates with the wing, whose x_c axis coincides with the PA, and the

Table 3.1: Comparison of the calculated and measured values of $\hat{r}_{m_1}$ for different insect wings. The value of $\hat{r}_{m_1}$ of the hawkmoth wing was measured by Willmott & Ellington (1997b). The values of $\hat{r}_{m_1}$ of the other three wings were measured by Ellington (1984a). The measurement errors are not taken into account. The model error is defined as $\left|\hat{r}_{m_1}^{cal} - \hat{r}_{m_1}^{meas}\right| / \hat{r}_{m_1}^{meas}$.

insect species	wing mass [mg]	measured $\hat{r}_{m_2}$ [-]	measured $\hat{r}_{m_1}$ [-]	calculated $\hat{r}_{m_1}$ [-]	model error (%)
hawkmoth	44.79	0.38	0.29	0.31	6.90
hoverfly	0.21	0.44	0.36	0.37	2.78
dronefly	0.53	0.40	0.32	0.33	3.13
bumblebee	0.54	0.44	0.36	0.37	2.78

y_c and z_c axes are perpendicular and parallel to the wing platform. The sweeping angle ϕ and pitching angle η can be described by these two frames, as shown in Fig. 3.3.

A harmonic function

$$\phi(t) = \phi_m \sin(2\pi f t) \tag{3.5}$$

is used to prescribe the sweeping motion with an amplitude of ϕ_m and a drive frequency f. The passive pitching motion is determined by the wing inertia, the rotational stiffness of the linear torsional spring and the aerodynamic torque about the PA (i.e., the x_c axis in Fig. 3.3). Based on Euler's second law of motion for a rigid body, the equation of motion for the pitching motion can be derived from

$$\tau_{x_c}^{\text{applied}} + \tau_{x_c}^{\text{iner}} = 0, \tag{3.6}$$

where $\tau_{x_c}^{\text{applied}}$ includes the elastic torque $\tau_{x_c}^{\text{elas}}$ due to the resistance from deformed spring and the aerodynamic torque $\tau_{x_c}^{\text{aero}}$ that will be discussed in next section. The inertial torque $\boldsymbol{\tau}^{\text{iner}}$ can be given in the co-rotating frame by

$$\boldsymbol{\tau}^{\text{iner}} = -\boldsymbol{I}\boldsymbol{\alpha}_c - \boldsymbol{\omega}_c \times (\boldsymbol{I}\boldsymbol{\omega}_c), \tag{3.7}$$

where $\boldsymbol{I}$ is the inertia matrix, and $\boldsymbol{\omega}_c$ and $\boldsymbol{\alpha}_c$ are the wing angular velocity and acceleration in the co-rotating frame, respectively. $\boldsymbol{\omega}_c$ and $\boldsymbol{\alpha}_c$ can be obtained by

$$\boldsymbol{\omega}_c = [\dot{\eta}, \dot{\phi}\sin\eta, \dot{\phi}\cos\eta]^{\text{T}}, \tag{3.8}$$

$$\boldsymbol{\alpha}_c = [\ddot{\eta}, \dot{\phi}\dot{\eta}\cos\eta + \ddot{\phi}\sin\eta, \ddot{\phi}\cos\eta - \dot{\phi}\dot{\eta}\sin\eta]^{\text{T}}. \tag{3.9}$$

The inertia matrix $\boldsymbol{I}$ can be calculated by

$$\boldsymbol{I} = \begin{bmatrix} I_{x_c x_c} & I_{x_c y_c} & I_{x_c z_c} \\ I_{y_c x_c} & I_{y_c y_c} & I_{y_c z_c} \\ I_{z_c x_c} & I_{z_c y_c} & I_{z_c z_c} \end{bmatrix} = \begin{bmatrix} \int_M z_c^2 dm & 0 & -\int_M x_c z_c dm \\ 0 & \int_M (x_c^2 + z_c^2) dm & 0 \\ -\int_M x_c z_c dm & 0 & \int_M x_c^2 dm \end{bmatrix}, \tag{3.10}$$

where the cross term $I_{x_c z_c}$ results from the asymmetry of the wing mass distribution about the PA. The inertia matrix expressed in the co-rotating frame does not change with
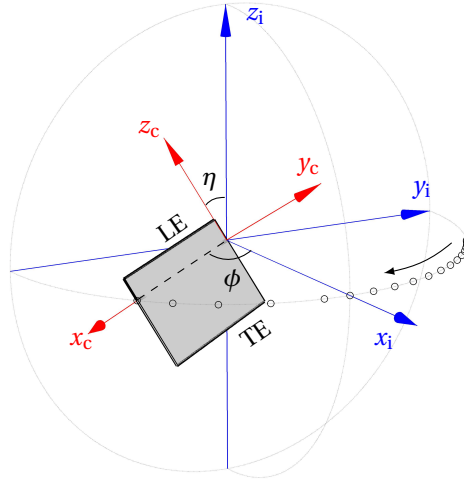
Figure 3.3: Two frames used for describing the motion of flapping wings. The inertial frame $x_i y_i z_i$ is fixed to the wing joint, while the co-rotating frame $x_c y_c z_c$ co-rotates with the wing.

the flapping motion, and this facilitates the easy derivation of the equation of motion. The inertial terms related to the wing thickness are ignored since the thickness is negligible when compared to the span and average chord length. Substituting the x_c component of $\boldsymbol{\tau}^{\text{iner}}$ and the formula of the elastic torque (i.e., $\tau_{x_c}^{\text{elas}} = -k_\eta \eta$) into Eq. 3.6, the equation of motion can be rewritten as

$$I_{x_c x_c} \ddot{\eta} + k_\eta \eta = \tau_{x_c}^{\text{aero}} + \frac{1}{2} I_{x_c z_c} \dot{\phi}^2 \sin(2\eta) - I_{x_c z_c} \ddot{\phi} \cos \eta, \tag{3.11}$$

where the last two inertial terms represent the centrifugal force and Euler force induced by the sweeping motion, respectively. It can be seen that both the aerodynamic and inertial terms introduce nonlinearity to the system. The influence of the inertial nonlinearity to the pitching motion depends on $I_{x_c x_c}$, $I_{x_c z_c}$ and $\phi(t)$. The values of $I_{x_c x_c}$ and $I_{x_c z_c}$ depend on the PA location, while $\phi(t)$ depends on the flapping frequency. In this study, the influence of the PA location and flapping frequency on the pitching motion will be studied, and the optimal wing design will be investigated to maximize the energy-efficiency during hovering flight.

3.3. AERODYNAMIC AND POWER CONSUMPTION MODELING

3.3.1. QUASI-STEADY AERODYNAMIC MODEL
The aerodynamic term $\tau_{x_c}^{\text{aero}}$ in the equation of motion (Eq. 3.11) is calculated by a predictive quasi-steady aerodynamic model as proposed by Wang *et al.* (2016). The quasi-steady assumption means that the transient aerodynamic loads on a flapping wing are equivalent to that on the wing undergoing a steady motion at the same transient velocity and angle of attack. The viscous drag at the thin boundary layer and the suction load

at the leading edge are ignored since they are negligible compared to the load resulting from the pressure difference between two sides of flapping wings (Sane, 2003). Consequently, the resultant aerodynamic force can be assumed to be perpendicular to the wing platform, i.e., aligned to the y_c axis in the co-rotating frame, over the entire stroke. Therefore, it is convenient to formulate the aerodynamic loads in the co-rotating frame. The resultant aerodynamic force and torque are calculated by

$$F_{y_c}^{aero} = F_{y_c}^{trans} + F_{y_c}^{rot} + F_{y_c}^{coupl} + F_{y_c}^{am}, \tag{3.12a}$$

$$\tau_{x_c}^{aero} = \tau_{x_c}^{trans} + \tau_{x_c}^{rot} + \tau_{x_c}^{coupl} + \tau_{x_c}^{am}, \tag{3.12b}$$

$$\tau_{z_c}^{aero} = \tau_{z_c}^{trans} + \tau_{z_c}^{rot} + \tau_{z_c}^{coupl} + \tau_{z_c}^{am}, \tag{3.12c}$$

where the four loading terms at the right-hand side of each equation originate from the wing translation, the rotation, the couping between them and the added mass effect. The translation-induced loading terms (i.e., $F_{y_c}^{trans}$, $\tau_{x_c}^{trans}$ and $\tau_{z_c}^{trans}$) represent the loads when a wing undergoes pure translation at a certain angle of attack. The rotation-induced loading terms (i.e., $F_{y_c}^{rot}$, $\tau_{x_c}^{rot}$ and $\tau_{z_c}^{rot}$) reflect the aerodynamic damping loads on the wing that purely rotates about its PA. The coupling terms (i.e., $F_{y_c}^{coupl}$, $\tau_{x_c}^{coupl}$ and $\tau_{z_c}^{coupl}$) represent the loads due to the coupling effect between the wing translation and rotation. The terms $F_{y_c}^{am}$, $\tau_{x_c}^{am}$ and $\tau_{z_c}^{am}$ reflect the loads due the added-mass effect as a result of the accelerated or decelerated fluid surrounding the wing. More details on the formulations of each term can be found in Chapter 2.

3.3.2. POWER CONSUMPTION
Due to the limited on-board power supply, the flight endurance of existing FWMAVs is generally less than 20 minutes (Floreano & Wood, 2015). This issue motivates us to improve the power efficiency of flapping wing designs.

For flapping wings with passive pitching, the total power consumption consists of three components: (1) aerodynamic power P^{aero} used to overcome the aerodynamic drag, (2) inertial power P^{iner} to accelerate the wing and surrounding fluid, and (3) elastic power P^{elas} due to the resistance from the elastic spring. These can be formulated as

$$P^{aero}(t) = -\tau_{x_c}^{aero}\omega_{x_c} - \tau_{z_c}^{aero}\omega_{z_c}, \tag{3.13a}$$

$$P^{iner}(t) = -\tau_{x_c}^{iner}\omega_{x_c} - \tau_{y_c}^{iner}\omega_{y_c} - \tau_{z_c}^{iner}\omega_{z_c}, \tag{3.13b}$$

$$P^{elas}(t) = k_\eta \eta \omega_{x_c}, \tag{3.13c}$$

respectively. Due to aerodynamic drag, $P^{aero} > 0$ during most parts of a flapping cycle. During wing reversals, the aerodynamic drag can be in the same direction as the sweeping motion due to the wing rotational effect. For such cases, $P^{aero} < 0$. The kinetic energy of the wing increases during the accelerating phase of each half-stroke and, thus, $P^{iner} > 0$. During deceleration, the wing starts to lose its kinetic energy, which implies $P^{iner} < 0$. The lost kinetic energy can be dissipated, used to compensate the energy consumed by the drag, or stored in the kinetic energy recovery drive system (KERS). The KERS can be in different forms, e.g., insect thoraxes (Dudley, 2002) and elastic structures of FWMAVs (Bolsman *et al.*, 2009, Lau *et al.*, 2014).

The uncertainty of the kinetic energy transformation complicates the modeling of the exact power consumed by flapping wings. Instead, two extreme power consumption scenarios are modeled. First, a KERS is used, thus, the cycle-averaged elastic and inertia power will be zero. Therefore, the total average power consumption $\bar{P}_{\text{KERS}}^{\text{total}}$ is equal to the average aerodynamic power, i.e.,

$$\bar{P}_{\text{KERS}}^{\text{total}} = \frac{1}{T} \int_T P^{\text{aero}} dt, \tag{3.14}$$

where T is the period of a flapping cycle. Second, a drive system which can not recover kinetic energy is used. In this case, the kinetic energy and the elastic energy will be first used to compensate the energy consumed by drag. The extra energy will be dissipated. For convenience, this type of drive system will be referred to as non-KERS in this work. The total average power consumption $\bar{P}_{\text{non-KERS}}^{\text{total}}$ for this extreme case can be calculated by

$$\bar{P}_{\text{non-KERS}}^{\text{total}} = \frac{1}{T} \int_T \Xi \left(P^{\text{aero}} + P^{\text{iner}} + P^{\text{elas}} \right) dt, \tag{3.15}$$

where $\Xi(\bullet)$ is an operator to set negative values to zero and keep positive values the same.

The power consumption by flapping wings should lie between $\bar{P}_{\text{KERS}}^{\text{total}}$ and $\bar{P}_{\text{non-KERS}}^{\text{total}}$. To facilitate the comparison of energy-efficiency between different wing designs, the average power is normalized by the mass that can be lifted by the corresponding wing design and denoted by adding a cap (e.g., $\hat{P}_{\text{KERS}}^{\text{total}}$ and $\hat{P}_{\text{non-KERS}}^{\text{total}}$).

3.4. OPTIMIZATION MODEL

To investigate the influence of the pitching axis (PA) location on the power efficiency, $\hat{d}_r$ and $\hat{d}_t$ are optimized. Meanwhile, the kinematics is also optimized by setting the sweeping frequency f and the rotational stiffness k_η as design variables. The minimization of the cycle-averaged power consumption $\hat{P}_{\text{KERS}}^{\text{total}}$ and $\hat{P}_{\text{non-KERS}}^{\text{total}}$ are set as the optimization objective for KERS and non-KERS, respectively, while sufficient lift force needs to be generated. The lift generated by optimized wings needs to be equal to the required lift (e.g., half of the body weight for two-winged FWMAVs).

It is interesting to compare the energy efficiency between wings with an optimal PA location and traditional wing designs which have a straight LE as the PA (see Fig. 3.1). For a fair comparison, the kinematics, i.e., the values of f and k_η, are also optimized for traditional wings subjected to the same objective and constraint.

For a fair comparison of the power consumption, all the wings studied in this work share the same span R, aspect ratio $Æ$, wing mass m^{w}, spanwise radius of the second moment of inertia $\hat{r}_{m_2}$, sweeping amplitude ϕ_m and the lift generation requirement $\bar{L}_{\text{req}}$. These parameters are prescribed by referring to an adult female hawkmoth (HMF2) studied by Willmott & Ellington (1997b), as listed in Table 3.2.

Due to the nonlinearity existing in the equation of motion for the passive pitching motion, both the lift and power are non-convex functions in the design domain expanded by four design variables (i.e., $\hat{d}_r$, $\hat{d}_t$, f and k_η). Therefore, a stochastic global optimization method (Li & Au, 2010) is used to obtain the rough optima. Then, the rough

Table 3.2: Prescribed parameters of flapping wings. $\mathcal{R}$ is the aspect ratio of a single wing and defined as R^2/S. $\bar{L}_{\mathrm{req}}$ is the lift generation required for a single wing.

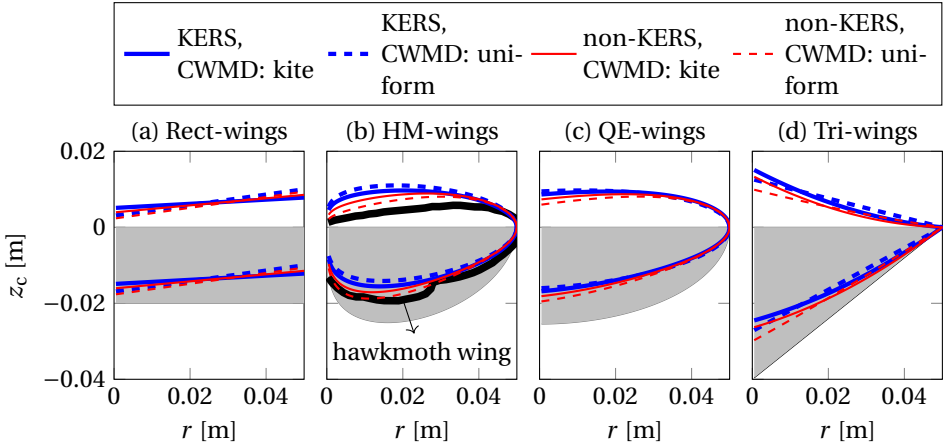| parameters	R	$\mathcal{R}$	m^{w}	$\hat{r}_{m_2}$	ϕ_m	$\bar{L}_{\mathrm{req}}$
units	[$\times 10^{-3}$m]	[-]	[$\times 10^{-6}$Kg]	[-]	[degrees]	[$\times 10^{-3}$N]
HMF2	51.00	2.77	46.01	0.38	61.64	9.21
model wings	50.00	2.50	50.00	0.38	60.00	9.80

Figure 3.4: Optimal pitching axis locations for different types of wings. Gray areas represent traditional wings with a straight leading edge (LE) as the PA. To facilitate the comparison, all the optimal PAs coincide with the straight LE of corresponding traditional wings.

solution is taken as the initial value for a gradient-based optimization method (*fmincon* from MATLAB®) which uses the sequential quadratic programming algorithm.

In this work, we study the optimal PA for eight wings resulting from the combination of four spanwise area distributions (SWADs) (see Fig. 3.1) and two chordwise mass distributions (CWMDs) (see Fig. 3.2). For each wing, both the two extreme power consumption cases are considered as the optimization objective. Therefore, 16 optimization cases are studied in total.

3.5. RESULTS AND ANALYSIS

3.5.1. OPTIMAL PITCHING AXIS LOCATION

For different wings, the shapes with the optimal PA location are compared to traditional wings which use a straight LE as the PA in Fig. 3.4. To facilitate the comparison, all the optimal pitching axes coincide with the straight LE of corresponding traditional wings. It can be seen that the pitching axes of all the optimized wings are located behind the LE. These optimized wings are quite different from traditional wings but can be very close to insect wings, as shown by the comparison between optimized HM-wings with the real
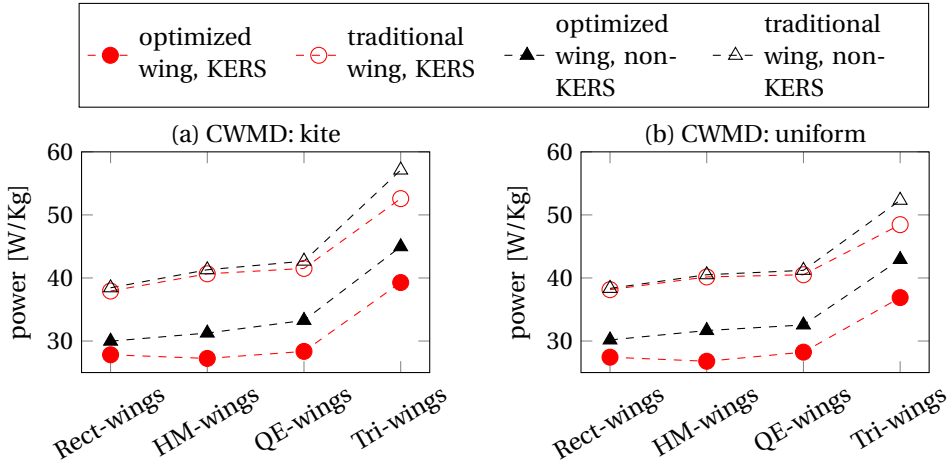
Figure 3.5: Comparison of power consumption of different wings for both KERS and non-KERS. The horizontal axis ticks Rect-wing, HM-wing, Rect-wing and Tri-wing represent the wings with the chordwise area distribution of the rectangular wing, the hawkmoth wing, the quarter-ellipsoidal wing and the triangular wing as shown in Fig.3.1, respectively.

hawkmoth wing in Fig. 3.4 (b).

Optimized wings with different CWMDs and subjected to different power consumption scenarios show close PA locations. However, there are recognizable differences between optimized wing shapes. First, when the same CWMD is used, the PA of optimized wings for KERS is further behind the LE as compared to the optimal PA for non-KERS. The difference is more prominent at the wing root than at the wing tip. Second, the optimal location of PA is more sensitive to the objective function than CWMD. It should be noted that aforementioned observations hold for all the four types of wings.

In order to interpret the optimal PA location, we plot the corresponding power consumption, pitching amplitudes, flapping frequency and the rotational stiffness for all the cases. Here, the pitching amplitude is defined by the maximum pitching angle. Intercomparisons are used to help the analysis.

3.5.2. ANALYSIS

Figure 3.5 compares the power consumed by different optimized wings. It is clearly seen that the wings with optimal PA location show a dramatical reduction of the power consumption as compared to traditional wings. For KERS, up to 33% of power can be saved by the HM-wing with the optimized PA when compared to the traditional HM-wing. The minimum amount of power that can be saved by the wing with optimized PA location is still more than 21%, as shown by the QE-wings for non-KERS.

It can be also observed that, for traditional wings, the use of KERS does not reduce the power consumption significantly as compared to non-KERS. In contrast, when the PA is at the optimal location, the power consumption shows a considerable drop for KERS. For instance, more than 13% of energy has been saved via recovering kinetic energy by the
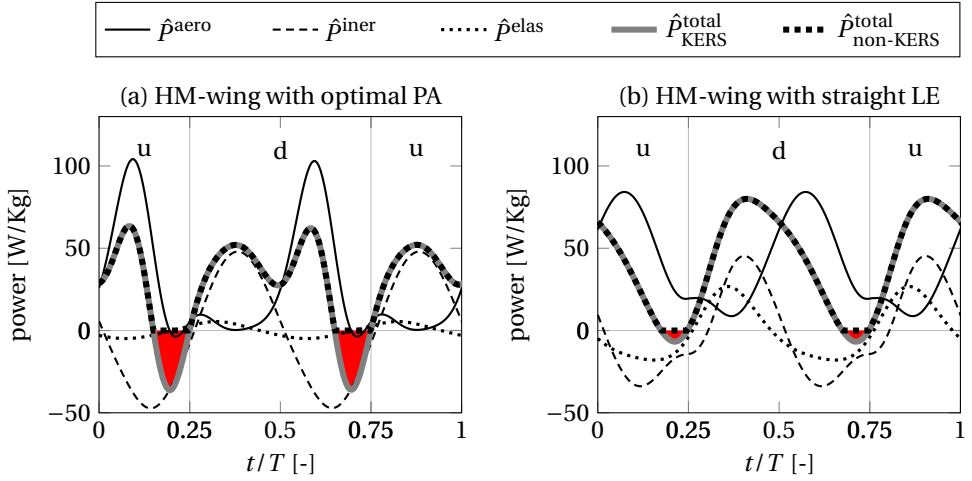
Figure 3.6: Comparison of the power histories for the HM-wings with a kite profile CWMD. (a) The wing has a optimal PA location. (b) The straight LE is taken as the PA. Filled areas between the curves for $\hat{P}_{KERS}^{total}$ and $\hat{P}_{non\text{-}KERS}^{total}$ indicate the kinetic energy that can be potentially recovered by drive system. "u" and "d" represent the upstroke and downstroke, respectively.

HM-wing with the optimal PA. The influence of PA location on the usefulness of kinetic energy recovery capacity can be better understood from the power plot in Fig. 3.6. The study of power history of the HM-wings with a kite profile CWMD is taken as an example. It can be seen that the aerodynamic power before pitching reversals is negligible for the HM-wings with optimal PA. Thus, the negative power due to the wing deceleration can not be completely offset by the aerodynamic power. Such a significant amount of unnecessary power consumption can be avoided by using KERS. In contrast, the traditional HM-wing still experiences a significant amount of aerodynamic power consumption before reversals which is almost equal to the negative inertial power. Thus, the remainder of the kinetic energy that can be stored is very limited.

From Fig. 3.5, we can also see that the Tri-wings show the lowest power efficiency. This is due to the fact that the Tri-wings have a smaller $\hat{r}_{s_1}$ as compared to other wings (see Fig. 3.1), which implies that the area of the Tri-wings is closer to the root on average. As a consequence, the aerodynamic efficiency of Tri-wings is lower due to the lower average flapping velocity.

The pitching amplitudes η_m corresponding to different optimized wings are compared in Figs. 3.7 (a) and (b). The plots show that the pitching amplitudes of wings with a straight LE are lower than wings with an optimal PA, and the pitching amplitudes of Tri-wings are lower than other wings. By comparing these results with the power plots in Fig. 3.5, it can be concluded that a higher pitching amplitude leads to lower power consumption. The conclusion can be explained by the relation between the aerodynamic power and the pitching amplitude. This is because, for KERS and non-KERS, the power consumption is equal to or dominated by the aerodynamic power, respectively. We know

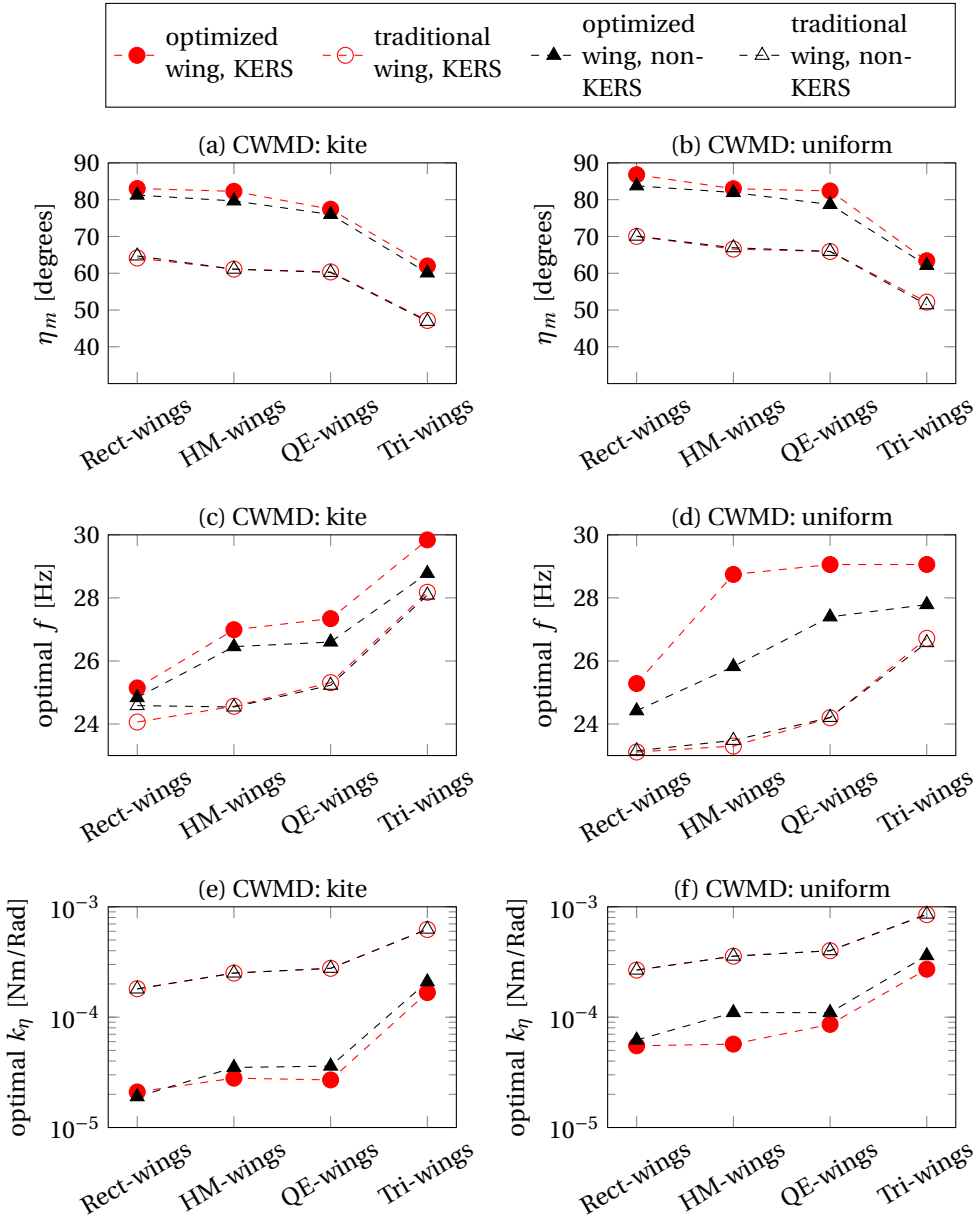**Figure 3.7:** Comparison of optimal results for four types of wings with two different chordwise mass distribution (CWMD) for both KERS and non-KERS.

that the aerodynamic power is proportional to the average drag, while the average drag is inversely proportional to the average lift-to-drag ratio since all the wings need to generate the same average lift. Furthermore, the value of the lift-to-drag ratio is inversely

3
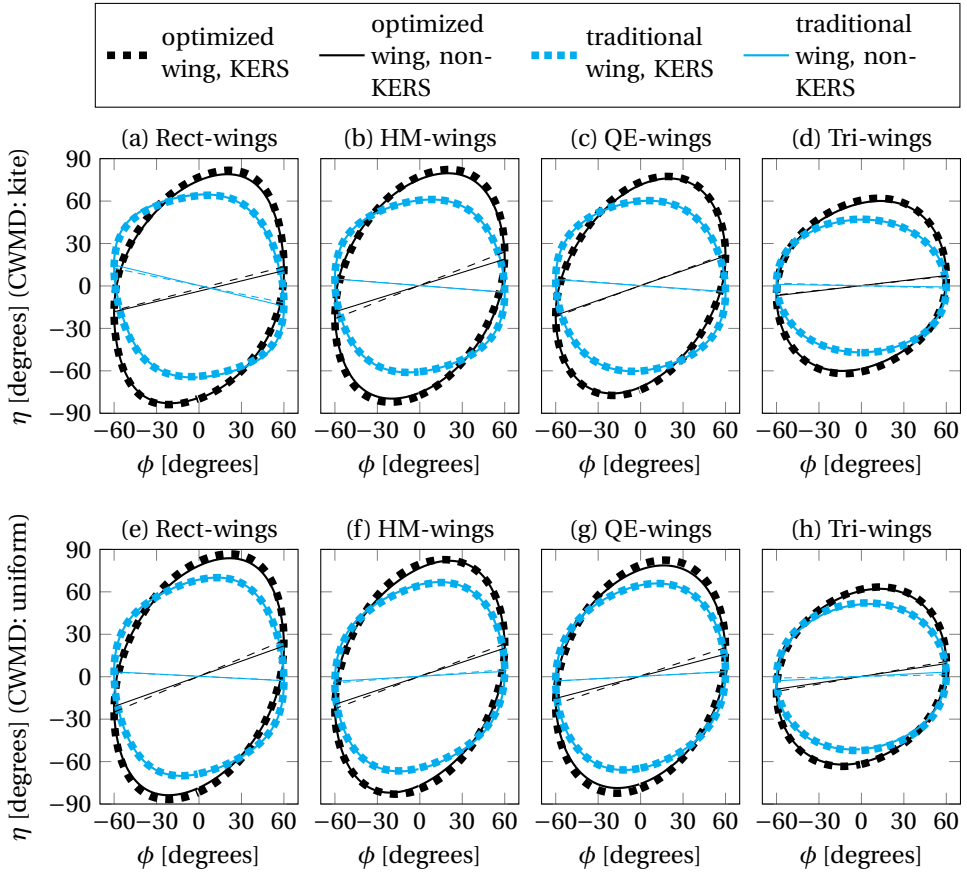
Figure 3.8: Phase portrait of optimal kinematics. The cross-line with a positive/negative slope means that the corresponding pitching motion is ahead/behind of the sweeping motion.

proportional the angle of attack based on the condition that the resultant aerodynamic force is perpendicular to the chord. We also know that the average angle of attack is inversely proportional to the pitching amplitude. Therefore, the aerodynamic power is inversely proportional to the pitching amplitude.

The lift generation is related to both the angle of attack and the flapping velocity. According the aerodynamic model proposed by Wang *et al.* (2016), the lift coefficient of a translational wing reaches its maximal value at the angle of attack (AOA) of 45°. In practice, due to the wing rotational and added-mass effects, a flapping wing reaches the highest lift coefficient at an AOA that slightly deviates from 45°. The corresponding AOA will be referred to as lift-maximizing AOA for convenience. The maximal cycle-averaged lift coefficient is attainable when the cycle-averaged absolute deviation of the AOA from the lift-maximizing AOA is minimized. The deviation can be partly reflected by the pitching amplitude. For example, if the pitching motion is assumed to be harmonic

and the lift-maximizing AOA is 45°, the pitching motion has the minimal deviation when the pitching amplitude is 55°. Therefore, for the wing with a pitching amplitude much higher than the lift-maximizing AOA, the average lift coefficient is inversely proportional to the pitching amplitude. We can see from Fig. 3.7 (a) to Fig. 3.7 (d) that, for the wing with a higher pitching amplitude (i.e., a smaller average lift coefficient), a higher flapping frequency is required to increase the flapping velocity such that the lift constraint can be satisfied. The frequencies with respect to the optimized HM-wings with a optimal PA location (see Fig. 3.7 (c)) are 27.04 Hz and 26.46 Hz for KERS and non-KERS, respectively. In contrast, the average flapping frequency of the reference hawkmoth (Willmott & Ellington, 1997a) is 25.40 Hz. The slightly overestimated frequency can be attributed to the smaller span and the higher required lift production of the model wing as compared the hawkmoth wing (see Table 3.2).

When the PA moves from the LE to the optimal location, the wing pitching inertia decreases. Meanwhile, the PA gets closer to the center of pressure (CP) which is normally located between the 1/4 chord to the mid-chord (Zhao *et al.*, 2010, Wang *et al.*, 2016). Both the change of the pitching inertia and the distance between the CP and PA tends to reduce the external torque applied on the PA. Therefore, in order to maintain the expected pitching amplitude, the wing rotational stiffness k_η needs to decrease simultaneously. This is why the optimal stiffness used by wings with a straight LE is much larger than that for the wings with a optimal PA location, as shown in Figs. 3.7 (e) and (f). This also provides an explanation to the wing shape and flexibility of insect wings. With a properly located PA, an insect wing can generate sufficient lift in the most efficient way. Meanwhile, the wing can be very flexible which implies that the structure can be lightweight. The light-weight wing design is also preferred for flapping wings of FWMAVs.

To gain more insight into the pitching motion of wings with the optimal PA, Figure. 3.8 shows the phase portraits of their kinematics and the comparison of the optimal kinematics between optimized and traditional wings. It can be seen that the reversals of pitching motion with respect to the wing with a optimal PA always take place in advance to the sweeping reversals. In contrast, the pitching reversals of traditional wings are generally delayed compared to sweeping reversals. The advanced pitching reversal can enhance the lift generation during the reversal phases (Dickinson *et al.*, 1999, Nakata & Liu, 2012b), and it has also been observed on the hovering hawkmoth (Nakata & Liu, 2012b). The PA location might be also one of the explanations to the advanced pitching reversals observed for insect flight.

In Figs 3.5, 3.7 and 3.8, we showed the optimal power consumption, design variables and kinematics for wings with both the kite and uniform profile CWMDs. It can be observed that the performance difference between the wings with these two CWMDs is marginal. For convenience, the analysis presented in this section was primarily based on the wings with the kite profile CWMD.

3.5.3. Influence of lift constraints

In order to investigate the dependence of the optimal PA location on the lift constraint, we further optimize the PA location for different lift productions, including 50%, 75%, 125% and 150% of the original value (1 g). Taking the HM-wing with a kite profile CWMD as an example, the optimal shapes for different lift constraints are quite close to the orig-
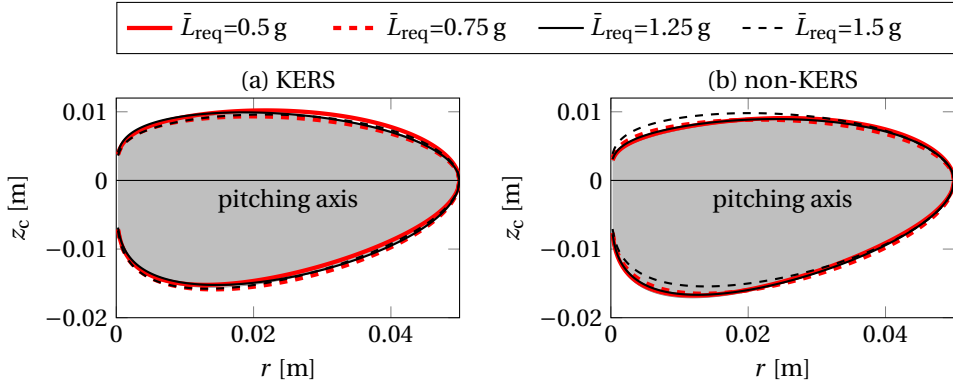
Figure 3.9: Comparison of wing shapes with optimal location of pitching axes for the HM-wing with the kite profile CWMD when subjected to different lift constraints ($\bar{L}_{req}$). The gray areas correspond to the lift constraint of 1 g.

inal optimal wing shape, as shown in Fig. 3.9.

Figure. 3.10 plots the optimal frequency and torsional stiffness as well as the corresponding power consumption and pitching amplitudes with respect to different lift constraints. The power plots in Fig. 3.10 (a) confirm that the wings with the optimal PA location are more energy-efficient than traditional wings regardless of the lift constraint. The optimal pitching amplitudes as shown in Fig. 3.10 (b) are approximately equal to the amplitude of the original optimal wing. In order to satisfy different lift constraints, the optimal frequency increases with the required lift production, as shown in Fig. 3.10 (c). Figure. 3.10 (d) shows that the optimal rotational stiffness for both the wings with the optimal PA location and traditional wings increases with the required lift production approximately at the same rate. However, the absolute change for wings with the optimal PA location is one order smaller than traditional wings.

Combining the results in Figs. 3.9 and 3.10, we can see that the wing with a properly located PA can generate different lift while maintaining a high power efficiency. This can be realized by changing the flapping frequency and a fine tuning of the wing stiffness. For insects, there are several ways to achieve minor stiffness changes, including the vein blood circulation (Hou *et al.*, 2015), wing warping (Ristroph & Childress, 2014). For FW-MAVs, there also exist many approaches to tune the wing stiffness, e.g., piezoelectric polymers, electrorheological fluids, and electrostatic softening (Peters *et al.*, 2015, 2016).

3.6. CONCLUSIONS

This chapter studied the optimal pitching axis (PA) location for different flapping wings to maximize the energy efficiency during hovering flight. We found that the optimal PA is located between the leading edge (LE) and the mid-chord line, which can result in shapes very similar to insect wings. In contrast, traditional wings used by most flapping wing micro air vehicles (FWMAVs) simply pitch about their straight LEs. The comparison of power consumption shows that wings with optimal PA can save up to 33% of power as compared to traditional wings with optimized kinematics. The PA location also influ-
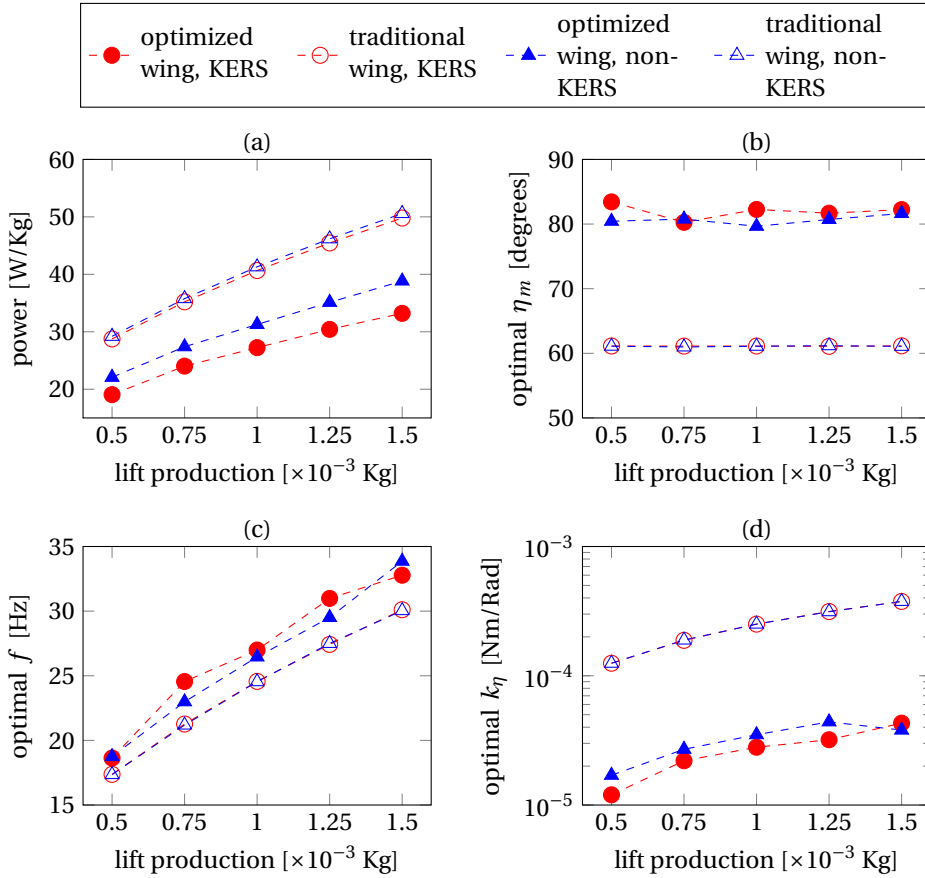
Figure 3.10: Comparison of optimal designs of the HM-wings with the kite profile CWMD for different lift constraints. The HM-wings are optimized for both KERS and non-KERS.

ences the usefulness of the kinetic energy recovery capacity of a drive system. More than 13% of the power consumption can be saved via recovering kinetic energy for wings with an optimal PA while the saved power is negligible for traditional wings. Furthermore, the wing with a properly located PA can generate different lift levels while maintaining a high energy efficiency. This can be realized by simultaneously changing the flapping frequency and fine tuning of the wing stiffness.

It is nontrivial to give a general optimal PA location for flapping wings considering the diversity of flight conditions and the nonlinear relation between the PA location and the flight performance. However, for flapping wings pitching passively, the PA location should be carefully designed.

4

OPTIMAL TWIST OF FLAPPING WINGS FOR EFFICIENT HOVERING FLIGHT

Spanwise twist can dominate the deformation of flapping wings and alters the aerodynamic performance and power efficiency of flapping wings by changing the local angle of attack. Traditional Fluid-Structure Interaction (FSI) models, based on Computational Structural Dynamics (CSD) and Computational Fluid Dynamics (CFD), have been used to investigate the influence of twist on the power efficiency. However, it is impractical to use them for twist optimization due to the high computational cost. On the other hand, it is of great interest to study the optimal twist of flapping wings.

In this chapter, we propose a computationally efficient FSI model based on an analytical twist model and a quasi-steady aerodynamic model which replace the expensive CSD and CFD methods. The twist model uses a polynomial to describe the change of the twist angle along the span. The polynomial order is determined based on a convergence study. A nonlinear plate model is used to evaluate the structural response of the twisted wing. The adopted quasi-steady aerodynamic model analytically calculates the aerodynamic loads by including four loading terms which originate from the wing's translation, rotation, their coupling and the added-mass effect. Based on the proposed FSI model, we optimize the twist of a rectangular wing by minimizing the power consumption during hovering flight. The power efficiency of optimized twistable and rigid wings is studied. This chapter is structured as follows. The introduction is provided in Sec. 4.1. The modeling of twistable flapping wings and the FSI is presented in Sec. 4.2. In Sec. 4.3, the proposed twist model is validated. In Sec. 4.4, flapping wing twist and kinematics are optimized by minimizing the power consumption for hovering using the proposed FSI model. Conclusions are presented in Sec. 4.5.

This chapter is based on the paper "Wang, Q., Goosen, J. F. L., & van Keulen, F. An Efficient Fluid-Structure Interaction Model for Optimizing Twistable Flapping Wings. (submitted to *Journal of Fluids and Structures*".

4.1. Introduction

Flapping wings keep receiving attention from biologists and engineers due to the increasing interest in flapping wing micro air vehicles (FWMAVs). Inspired by insect wings, the kinematics and shape for FWMAV wings have been studied more extensively as compared to the wing flexibility.

The wing thickness is typically one to two orders smaller than the wing span and, consequently, insects wings can be modeled as thin-walled structures. The apparent wing flexibility depends on the morphological characteristics, e.g., the venation layout, cross-sectional profile and the membrane thickness. Due to the inertial and aerodynamic loads, dramatic out-of-plane deformation can be observed for some insect wings. The deformation can be decomposed into three modes (Wootton, 1981): spanwise bending, spanwise twist and chordwise camber. For insect wings, the deformation can be dominated by different modes (Willmott & Ellington, 1997a, Chen et al., 2013, Zheng et al., 2013).

For artificial wings, the deformation can also be described by the three modes. Among them, the twist is of particular interest for realizing power-efficient wing designs because of four reasons. First, to realize the required wing kinematics, the spanwise bending is normally restricted by the wing structural designs, e.g., using longitudinal stiffeners (Bolsman et al., 2009, de Croon et al., 2009) or chordwise corrugations (Tanaka & Wood, 2010, Tanaka, 2012). Second, the turbulent flow surrounding flapping wings is not as sensitive as a laminar flow to the wing camber (Du & Sun, 2010). Third, cm-scale flapping wings (de Croon et al., 2009, Bolsman et al., 2009) are commonly used for FWMAVs. Such wings can exhibit large twist due to the large difference of the inertial and aerodynamic loads at the wing root and tip. Fourth, the twist can dramatically alter the local angle of attack along the span, which changes the aerodynamic performance and the power efficiency. Therefore, this work exclusively focuses on the modeling and effects of wing twist. In addition, only hovering flight is considered because (1) the wing deformation is most pronounced during hovering flight (Willmott & Ellington, 1997a), and (2) hovering flight is generally more power-consuming as compared to forward flight (Dudley, 2002).

Traditional Fluid-Structure Interaction (FSI) models, based on Computational Structural Dynamics (CSD) and Computational Fluid Dynamics (CFD), have been used to investigate the influence of wing twist on the aerodynamic performance and power efficiency of different flapping wings (Du & Sun, 2008, 2010, Nakata & Liu, 2012a,b, Dai et al., 2012). However, limited by the high computational cost, it is impractical to use them for twist optimization. The latter is of great interest for the study of insect wings and the design of artificial wings. Moreover, most of the studies on FSI of flexible wings prescribed the pitching motion at the root, while in reality passive pitching is widely used by wings of insects (Ennos, 1989, Bergou et al., 2007) and FWMAVs (de Croon et al., 2009, Bolsman et al., 2009, Ma et al., 2013). The prescribed pitching motion helps the simulation to converge easier and reduces the computational cost. However, the power consumption of flapping wings with prescribed and passive pitching motion can differ dramatically (Han et al., 2015). In this work, we propose a computationally efficient FSI model to study the (optimal) twist of flapping wings. The proposed FSI model uses an analytical twist model for the structural analysis and a quasi-steady aerodynamic model

(Wang *et al.*, 2016) for the aerodynamic analysis.

4.2. MODELING OF TWISTABLE FLAPPING WINGS

In this work, rectangular flapping wings with uniform thickness are studied. The wings will be modeled as isotropic and homogeneous plates which exhibit twist. Linear elastic material model will be used for structural analysis. In the following subsections, the wing kinematic model and equations of motion will be introduced.

4.2.1. KINEMATICS

The wing motion can be described by a combination of three successive rigid-body rotations and an elastic deformation, as illustrated in Fig. 4.1. The rigid-body rotations consist of the sweeping motion about the z_i axis of the inertial frame $x_i y_i z_i$, the heaving motion about the y_θ axis of the intermediate frame $x_\theta y_\theta z_\theta$, and the pitching motion about the y_η axis of another intermediate frame $x_\eta y_\eta z_\eta$. Thereafter, the frame $x_c y_c z_c$ which co-rotates with the undeformed wing is introduced. The co-rotating frame has its x_c axis directing from the root to the tip of the undeformed wing. Its z_c axis coincides with the undeformed wing plane. Three Euler angles, namely the sweeping angle ϕ, heaving angle θ and the pitching angle η, are used to quantify these rotations. The
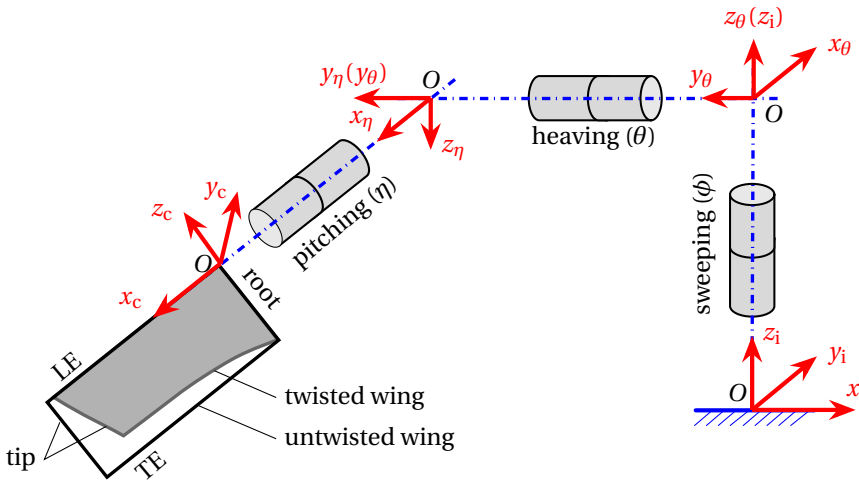
Figure 4.1: Schematic diagram of a twisted rectangular flapping wing. Three successive rigid-body rotations corresponding to the sweeping, heaving and pitching motion are illustrated using the "cans in series" approach (Schwab & Meijaard, 2006). Four frames are involved in the rigid-body rotations, including the inertial frame $x_i y_i z_i$, two intermediate frames $x_\theta y_\theta z_\theta$ and $x_\eta y_\eta z_\eta$, and the co-rotating frame $x_c y_c z_c$. These frames share the same origin O.
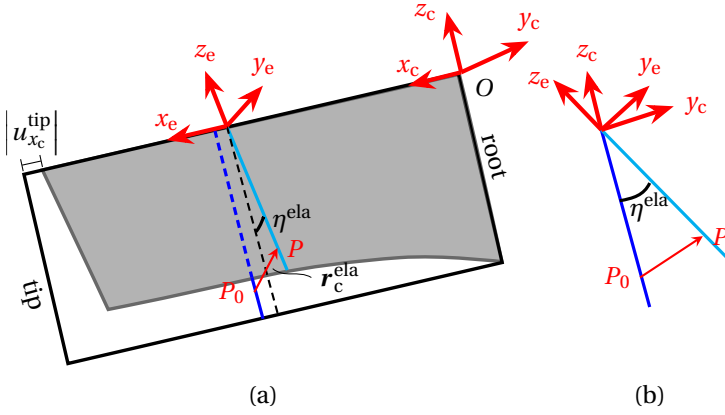
Figure 4.2: Schematic diagram of the elastic displacement of a twisted rectangular wing. The elastic frame $x_e y_e z_e$ is generated by first translating the co-rotating frame $x_c y_c z_c$ along the leading edge and then rotating by the local twist angle. P_0 and P indicate the positions of an arbitrary point at the mid-plane before and after twist. The spanwise tip displacement and the local pitching angle are denoted as $u_{x_c}^{tip}$ and η^{ela}, respectively. $u_{x_c}^{tip}$ will be negative due to the shortening effect. (a) 3D view of the untwisted and twisted wing. (b) 2D view of the local chord when observed from the wing tip.

corresponding rotation matrices are

$$\boldsymbol{R}_\phi = \begin{bmatrix} \cos\phi & -\sin\phi & 0 \\ \sin\phi & \cos\phi & 0 \\ 0 & 0 & 1 \end{bmatrix}, \quad \boldsymbol{R}_\theta = \begin{bmatrix} \cos\theta & 0 & \sin\theta \\ 0 & 1 & 0 \\ -\sin\theta & 0 & \cos\theta \end{bmatrix} \quad \text{and} \quad \boldsymbol{R}_\eta = \begin{bmatrix} 1 & 0 & 0 \\ 0 & \cos\eta & -\sin\eta \\ 0 & \sin\eta & \cos\eta \end{bmatrix}.$$

$$(4.1)$$

The wing's elastic deformation is defined with respect to the co-rotating frame in order to decouple wing deformation and finite rigid-body motions. For a general point P at the mid-plane of the twisted wing, as shown in Fig. 4.2, the position vector is denoted as $\boldsymbol{r}_i = [x_i, y_i, z_i]^T$ in the inertial frame or $\boldsymbol{r}_c = [x_c, y_c, z_c]^T$ in the co-rotating frame. In the co-rotating frame, the position vector $\boldsymbol{r}_i$ is related to $\boldsymbol{r}_c$ via the transformation matrix $\boldsymbol{R}_{c\rightarrow i} (= \boldsymbol{R}_\phi \boldsymbol{R}_\theta \boldsymbol{R}_\eta)$. $\boldsymbol{r}_c$ can be decomposed as

$$\boldsymbol{r}_c = \boldsymbol{r}_{c0} + \boldsymbol{r}_c^{ela}, \tag{4.2}$$

where $\boldsymbol{r}_{c0} (=[x_{c0}, 0, z_{c0}]^T)$ is the position vector of point P before twist, and the corresponding elastic displacement $\boldsymbol{r}_c^{ela}$ has three components, i.e., u_{x_c}, u_{y_c}, and u_{z_c}. The components u_{x_c}, u_{y_c} and u_{z_c} represent the displacement in the x_c, y_c and z_c directions, respectively, as shown in Fig. 4.2. Two assumptions are made regarding wing twist. First, an arbitrary chord from the untwisted wing stays straight and unstretched after twist. Second, the spanwise displacement due to the shortening effect (Trahair, 2005) changes linearly from zero at the wing root to $u_{x_c}^{tip}$ (< 0) at the tip. Thus, the displacement of point

P can be given by

$$\boldsymbol{r}_{\mathrm{c}}^{\mathrm{ela}} = \begin{bmatrix} u_{x_{\mathrm{c}}} \\ u_{y_{\mathrm{c}}} \\ u_{z_{\mathrm{c}}} \end{bmatrix} = \begin{bmatrix} u_{x_{\mathrm{c}}}^{\mathrm{tip}} x_{\mathrm{c}0}/R \\ -z_{\mathrm{c}0}\sin(\eta^{\mathrm{ela}}) \\ z_{\mathrm{c}0}[\cos(\eta^{\mathrm{ela}})-1] \end{bmatrix}. \tag{4.3}$$

Here R is the span of the undeformed wing, and η^{ela} is the local, additional, pitching angle induced by twist. A polynomial function of degree n is used to approximate the change of η^{ela} along the span, i.e.,

$$\eta^{\mathrm{ela}} = \sum_{i=1}^{n} a_i x_{\mathrm{c}0}^i, \qquad 0 \leqslant x_{\mathrm{c}0} \leqslant R, \tag{4.4}$$

where the coefficients a_i, $i \in [1,...,n]$, are determined by the twist angles at n different locations. For convenience, the chords with $x_{\mathrm{c}0} = iR/n$ are selected, and the corresponding twist angles are denoted by q_i^{ela}. Thus, the polynomial coefficients of Eq. 4.4 are determined by

$$\begin{bmatrix} a_1 \\ a_2 \\ \vdots \\ a_n \end{bmatrix} = \begin{bmatrix} R/n & (R/n)^2 & \dots & (R/n)^n \\ 2R/n & (2R/n)^2 & \dots & (2R/n)^n \\ \vdots & \vdots & \ddots & \vdots \\ nR/n & (nR/n)^2 & \dots & (nR/n)^n \end{bmatrix}^{-1} \begin{bmatrix} q_1^{\mathrm{ela}} \\ q_2^{\mathrm{ela}} \\ \vdots \\ q_n^{\mathrm{ela}} \end{bmatrix}. \tag{4.5}$$

As shown in Fig. 4.2, the elastic frame $x_{\mathrm{e}}y_{\mathrm{e}}z_{\mathrm{e}}$ is committed to a local chord. This frame is generated by first translating the co-rotating frame $x_{\mathrm{c}}y_{\mathrm{c}}z_{\mathrm{c}}$ along the leading edge and then rotating it by the local twist angle. In this frame, the translational velocity and acceleration of the chord can be calculated by

$$\boldsymbol{v}_{\mathrm{e}} = \left[v_{x_{\mathrm{e}}}, v_{y_{\mathrm{e}}}, v_{z_{\mathrm{e}}}\right]^{\mathrm{T}} = \boldsymbol{R}_{\mathrm{e}\to\mathrm{i}}^{\mathrm{T}} \dot{\boldsymbol{R}}_{\mathrm{e}\to\mathrm{i}}[x_{\mathrm{e}},0,0]^{\mathrm{T}} \tag{4.6}$$

and

$$\boldsymbol{a}_{\mathrm{e}} = \left[a_{x_{\mathrm{e}}}, a_{y_{\mathrm{e}}}, a_{z_{\mathrm{e}}}\right]^{\mathrm{T}} = \boldsymbol{R}_{\mathrm{e}\to\mathrm{i}}^{\mathrm{T}} \ddot{\boldsymbol{R}}_{\mathrm{e}\to\mathrm{i}}[x_{\mathrm{e}},0,0]^{\mathrm{T}}, \tag{4.7}$$

respectively, where $\boldsymbol{R}_{\mathrm{e}\to\mathrm{i}}$ $(=\boldsymbol{R}_\phi \boldsymbol{R}_\theta \boldsymbol{R}_\eta \boldsymbol{R}_{\mathrm{e}})$ is the resulting transformation matrix from the elastic frame to the inertial frame. The rotational velocity and acceleration of the chord can be obtained by

$$\boldsymbol{\omega}_{\mathrm{e}} = \left[\omega_{x_{\mathrm{e}}}, \omega_{y_{\mathrm{e}}}, \omega_{z_{\mathrm{e}}}\right]^{\mathrm{T}} = \boldsymbol{R}_{\mathrm{e}\to\mathrm{i}}^{\mathrm{T}}\left[0,0,\dot\phi\right]^{\mathrm{T}} + \boldsymbol{R}_{\mathrm{e}\to\theta}^{\mathrm{T}}\left[0,\dot\theta,0\right]^{\mathrm{T}} + \left[\dot\eta+\dot\eta^{\mathrm{ela}},0,0\right]^{\mathrm{T}} \tag{4.8}$$

and

$$\boldsymbol{\alpha}_{\mathrm{e}} = \left[\alpha_{x_{\mathrm{e}}}, \alpha_{y_{\mathrm{e}}}, \alpha_{z_{\mathrm{e}}}\right]^{\mathrm{T}} = \boldsymbol{R}_{\mathrm{e}\to\mathrm{i}}^{\mathrm{T}}\left[0,0,\ddot\phi\right]^{\mathrm{T}} + \boldsymbol{R}_{\mathrm{e}\to\theta}^{\mathrm{T}}\left[0,\ddot\theta,0\right]^{\mathrm{T}} + \left[\ddot\eta+\ddot\eta^{\mathrm{ela}},0,0\right]^{\mathrm{T}}, \tag{4.9}$$

respectively, with $\boldsymbol{R}_{\mathrm{e}\to\theta}$ $(=\boldsymbol{R}_\theta \boldsymbol{R}_\eta \boldsymbol{R}_{\mathrm{e}})$ representing the resulting transformation matrix from the elastic frame to the frame $x_\theta y_\theta z_\theta$. These translational and rotational quantities will be used for the calculation of aerodynamic forces and power consumption of twistable wings.

4.2.2. EQUATIONS OF MOTION

The generalized coordinates that determine the wing kinematics include

$$q = \left[\left[q^{\mathrm{rot}} \right]^{\mathrm{T}}, \left[q^{\mathrm{ela}} \right]^{\mathrm{T}} \right]^{\mathrm{T}}, \tag{4.10}$$

where q^{rot} (= $[q_1^{\mathrm{rot}}, q_2^{\mathrm{rot}}, q_3^{\mathrm{rot}}]^{\mathrm{T}}$) and q^{ela} (= $[q_1^{\mathrm{ela}}, q_2^{\mathrm{ela}}, ..., q_n^{\mathrm{ela}}, q_{n+1}^{\mathrm{ela}}]^{\mathrm{T}}$) are associated to the wing rigid-body rotations and the elastic deformation, respectively. For convenience, q^{rot} and q^{ela} will be referred to as rotational and elastic generalized coordinates, respectively. The first n coordinates of q^{ela} have been introduced in Eq. 4.5. The coordinates $q_1^{\mathrm{rot}}, q_2^{\mathrm{rot}}, q_3^{\mathrm{rot}}$ and q_{n+1}^{ela} represent the sweeping angle ϕ, heaving angle θ, pitching angle η and the spanwise tip displacement $u_{x_c}^{\mathrm{tip}}$, respectively.

The wing's equations of motion can be derived from Lagrange's equation

$$\frac{d}{dt}\left(\frac{\partial E_{\mathrm{k}}}{\partial \dot{q}}\right) - \frac{\partial E_{\mathrm{k}}}{\partial q} + \frac{\partial E_{\mathrm{p}}}{\partial q} = Q^{\mathrm{ext}}, \tag{4.11}$$

with E_{k} and E_{p} representing the wing's kinetic and potential energy, respectively, and Q^{ext} the generalized forces related to the external drive and aerodynamic loads.

KINETIC ENERGY

The wing's kinetic energy can be calculated by

$$E_{\mathrm{k}} = \frac{1}{2}\iint_S h\rho^{\mathrm{w}} \dot{r}_{\mathrm{i}}^{\mathrm{T}} \dot{r}_{\mathrm{i}} ds = \frac{1}{2}\iint_S h\rho^{\mathrm{w}} \left(L\dot{q}\right)^{\mathrm{T}} L\dot{q} ds \triangleq \frac{1}{2}\dot{q}^{\mathrm{T}} M^{\mathrm{w}} \dot{q}, \tag{4.12}$$

where h is the wing thickness, S is the area of the untwisted wing, ρ^{w} is the wing density, and M^{w} is the wing's mass matrix. M^{w} is given by

$$M^{\mathrm{w}} = \iint_S h\rho^{\mathrm{w}} L^{\mathrm{T}} L ds, \tag{4.13}$$

with

$$L = \left[\frac{\partial (R_{\mathrm{c}\to\mathrm{i}} r_{\mathrm{c}})}{\partial q^{\mathrm{rot}}}, R_{\mathrm{c}\to\mathrm{i}} \frac{\partial r_{\mathrm{c}}}{\partial q^{\mathrm{ela}}} \right]. \tag{4.14}$$

Substituting the kinetic energy (Eq. 4.12) into the first two terms at the left-hand side of the Lagrange's equation (Eq. 4.11) yields

$$\frac{d}{dt}\left(\frac{\partial E_{\mathrm{k}}}{\partial \dot{q}}\right) - \frac{\partial E_{\mathrm{k}}}{\partial q} = M^{\mathrm{w}} \ddot{q} + Q_{\mathrm{v}}, \tag{4.15}$$

where Q_{v} represents the sum of the centrifugal and Coriolis forces, i.e.,

$$Q_{\mathrm{v}} = \dot{M}^{\mathrm{w}} \dot{q} - \left[\frac{\partial}{\partial q}\left(\frac{1}{2}\dot{q}^{\mathrm{T}} M^{\mathrm{w}} \dot{q}\right) \right]^{\mathrm{T}}. \tag{4.16}$$

ELASTIC POTENTIAL ENERGY

Typically, the pitching motion of flapping wings results from both the torsion/bending of the elastic elements at the wing root (e.g., torsional spring, elastic hinge or slender beam) and the deformation of the wing plate. These two contributions are functions of the generalized coordinates $\boldsymbol{q}^{\text{rot}}$ and $\boldsymbol{q}^{\text{ela}}$, respectively. Therefore, the total wing potential energy can be decomposed into

$$E_{\text{p}} = E_{\text{p}}^{\text{rot}}\left(\boldsymbol{q}^{\text{rot}}\right) + E_{\text{p}}^{\text{ela}}\left(\boldsymbol{q}^{\text{ela}}\right), \tag{4.17}$$

with $E_{\text{p}}^{\text{rot}}$ and $E_{\text{p}}^{\text{ela}}$ representing the elastic energy related to the rigid-body rotations and the elastic wing twist, respectively. By assuming linear elastic root elements (Howell, 2001, Whitney & Wood, 2010, Wang *et al.*, 2014a), $E_{\text{p}}^{\text{rot}}$ can be formulated as

$$E_{\text{p}}^{\text{rot}} = \frac{1}{2}\left[\boldsymbol{q}^{\text{rot}}\right]^{\text{T}}\boldsymbol{K}^{\text{rot}}\boldsymbol{q}^{\text{rot}}, \tag{4.18}$$

where $\boldsymbol{K}^{\text{rot}}$ represents the stiffness matrix associated to the rigid-body rotations. Based on the linear elastic material model, the potential energy $E_{\text{p}}^{\text{ela}}$ can be calculated by

$$E_{\text{p}}^{\text{ela}} = \frac{1}{2}\iiint_{V}\boldsymbol{\epsilon}^{T}\boldsymbol{C}\boldsymbol{\epsilon}\,dv, \tag{4.19}$$

of which V is the wing volume, $\boldsymbol{\epsilon}$ is the wing strain, and $\boldsymbol{C}$ is the matrix with elastic coefficient. Nonlinear strain-displacement relations for plates with moderate deformation are used to calculate the strain, as given by

$$\boldsymbol{\epsilon} = \begin{bmatrix} \epsilon_{x_{c0}} \\ \epsilon_{z_{c0}} \\ \gamma_{x_{c0}z_{c0}} \end{bmatrix} = \begin{bmatrix} \frac{\partial u_{x_c}}{\partial x_c} + \frac{1}{2}\left(\frac{\partial u_{x_c}}{\partial x_c}\right)^2 + \frac{1}{2}\left(\frac{\partial u_{z_c}}{\partial x_c}\right)^2 + \frac{1}{2}\left(\frac{\partial u_{y_c}}{\partial x_c}\right)^2 - y_c\frac{\partial^2 u_{y_c}}{\partial x_c^2} \\ \frac{\partial u_{z_c}}{\partial z_c} + \frac{1}{2}\left(\frac{\partial u_{x_c}}{\partial z_c}\right)^2 + \frac{1}{2}\left(\frac{\partial u_{z_c}}{\partial z_c}\right)^2 + \frac{1}{2}\left(\frac{\partial u_{y_c}}{\partial z_c}\right)^2 - y_c\frac{\partial^2 u_{y_c}}{\partial z_c^2} \\ \frac{\partial u_{z_c}}{\partial x_c} + \frac{\partial u_{x_c}}{\partial z_c} + \frac{\partial u_{x_c}}{\partial z_c}\frac{\partial u_{x_c}}{\partial x_c} + \frac{\partial u_{z_c}}{\partial z_c}\frac{\partial u_{z_c}}{\partial x_c} + \frac{\partial u_{y_c}}{\partial z_c}\frac{\partial u_{y_c}}{\partial x_c} - 2y_c\frac{\partial^2 u_{y_c}}{\partial x_c\partial z_c} \end{bmatrix}, \tag{4.20}$$

where ϵ and γ represent the normal and shear strain, respectively. It can be observed that Kirchhoff's hypothesis is used and quadratic membrane strain terms are included. The importance of these nonlinear strain terms increases with the twist angle. The constitutive matrix in Eq. 4.19 is given by

$$\boldsymbol{C} = \frac{E}{1-v^2}\begin{bmatrix} 1 & v & 0 \\ v & 1 & 0 \\ 0 & 0 & (1-v)/2 \end{bmatrix}, \tag{4.21}$$

with E and v representing the Young's modulus and Poisson's ratio of the wing, respectively.

Knowing $E_{\text{p}}^{\text{rot}}$ and $E_{\text{p}}^{\text{ela}}$, $\frac{\partial E_{\text{p}}}{\partial \boldsymbol{q}}$ can be calculated. The derivative physically represents the generalized elastic force. If the generalized elastic force is denoted as $\boldsymbol{Q}^{\text{ela}}$, we get

$$\frac{\partial E_{\text{p}}}{\partial \boldsymbol{q}} = \boldsymbol{Q}^{\text{ela}}. \tag{4.22}$$
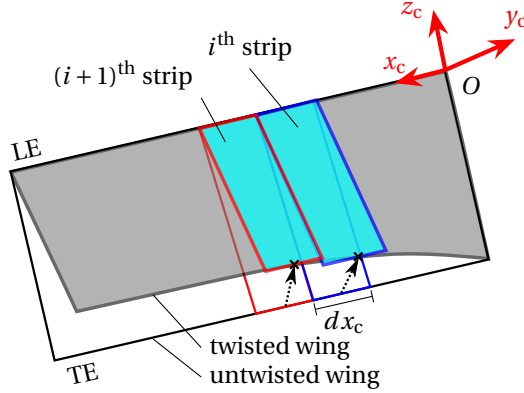
Figure 4.3: Schematic diagram of the blade element method used with the quasi-steady aerodynamic model. (a) 3D view of a wing configuration with two adjacent chordwise strips before and after twist. The width is exaggerated. (b) 2D side-view of the ith strip. The solid and open circles represent the leading edge and the center of pressure, respectively.

EXTERNAL FORCES

The generalized external force in the Lagrange's equation originates from two sources, i.e.,

$$\boldsymbol{Q}^{\text{ext}} = \boldsymbol{Q}^{\text{drive}} + \boldsymbol{Q}^{\text{aero}}, \tag{4.23}$$

where $\boldsymbol{Q}^{\text{drive}}$ and $\boldsymbol{Q}^{\text{aero}}$ correspond to the drive and aerodynamic loads, respectively. In this work, we assume the drive load to be applied at the wing joint. Therefore, $\boldsymbol{Q}^{\text{drive}}$ can be expressed as

$$\boldsymbol{Q}^{\text{drive}} = \left[Q^{\text{drive}}_{q_1^{\text{rot}}}, Q^{\text{drive}}_{q_2^{\text{rot}}}, Q^{\text{drive}}_{q_3^{\text{rot}}}, \boldsymbol{0}^{\text{T}}_{1\times(n+1)} \right]^{\text{T}}, \tag{4.24}$$

of which $Q^{\text{drive}}_{q_1^{\text{rot}}}$, $Q^{\text{drive}}_{q_2^{\text{rot}}}$ and $Q^{\text{drive}}_{q_3^{\text{rot}}}$ represent the drive loads applied on the rotational axes corresponding to the sweeping motion, heaving motion and the pitching motion, respectively. Some of these three terms will be equal to zero if the corresponding motion is fully passive. For instance, $Q^{\text{drive}}_{q_3^{\text{rot}}}$ is zero for wings using passive pitching (Bolsman *et al.*, 2009, Ma *et al.*, 2013).

The generalized aerodynamic force $\boldsymbol{Q}^{\text{aero}}$ is calculated by the quasi-steady aerodynamic model proposed by Wang *et al.* (2016). This model assumes that the transient resultant aerodynamic force $\boldsymbol{F}^{\text{aero}}_{\text{e}}$ does not rely on the flow history and is determined by the transient velocity, acceleration and angle of attack. Due to the wing rotation and twist, the kinematics varies from the wing root to the tip and from the leading edge (LE) to the trailing edge (TE). Therefore, the blade element method (Osborne, 1951) is applied to divide the wing planform into chordwise strips with an infinitesimal width dx_{c}. The infinitesimal resultant aerodynamic force $d\boldsymbol{F}^{\text{aero}}_{\text{e}}$ acting on an arbitrary infinitesimal strip of a twisted wing is approximated by the force on a flat strip. As illustrated in Fig. 4.3, the flat strip is obtained by rotating the respective strip of the untwisted wing

by the local twist angle. The tip displacement $u_{x_c}^{\text{tip}}$ due to the shortening effect is typically two orders smaller than the original span for a moderately twisted wing. Therefore, the change of the wing span due to the twist is neglected for the aerodynamic analysis. The quasi-steady aerodynamic model assumes the resultant force to be perpendicular to the local flat strip considering the pressure load dominates the aerodynamic load on flapping wings (Wang *et al.*, 2016). Therefore, $d\boldsymbol{F}_{\text{e}}^{\text{aero}}$ can be expressed as

$$d\boldsymbol{F}_{\text{e}}^{\text{aero}} = dF_{y_{\text{e}}}^{\text{aero}}\boldsymbol{e}_{y_{\text{e}}}, \tag{4.25}$$

with $\boldsymbol{e}_{y_{\text{e}}}$ denoting the unit vector in the direction of the y_{e} axis of the elastic frame. The quasi-steady model calculates the magnitude of $dF_{y_{\text{e}}}^{\text{aero}}$ by including four loading terms:

$$dF_{y_{\text{e}}}^{\text{aero}} = \left(\tilde{F}_{y_{\text{e}}}^{\text{trans}} + \tilde{F}_{y_{\text{e}}}^{\text{rot}} + \tilde{F}_{y_{\text{e}}}^{\text{coupl}} + \tilde{F}_{y_{\text{e}}}^{\text{am}} \right) dx_{\text{e}}, \tag{4.26}$$

where $\tilde{F}_{y_{\text{e}}}^{\text{trans}}$, $\tilde{F}_{y_{\text{e}}}^{\text{rot}}$, $\tilde{F}_{y_{\text{e}}}^{\text{coupl}}$ and $\tilde{F}_{y_{\text{e}}}^{\text{am}}$ represent the force components resulting from the translation, rotation, their coupling and the added-mass effect of a strip of unit width, respectively. The detailed expressions of these forces are provided in Chapter 2. The generalized aerodynamic force for the entire wing can be obtained by

$$\boldsymbol{Q}^{\text{aero}} = \int_0^R \left\{ \tilde{F}_{y_{\text{e}}}^{\text{trans}} \left[\frac{\partial \boldsymbol{r}_{\text{i,cp}}^{\text{trans}}}{\partial \boldsymbol{q}} \right]^{\text{T}} + \tilde{F}_{y_{\text{e}}}^{\text{rot}} \left[\frac{\partial \boldsymbol{r}_{\text{i,cp}}^{\text{rot}}}{\partial \boldsymbol{q}} \right]^{\text{T}} \right.$$
$$\left. + \tilde{F}_{y_{\text{e}}}^{\text{coupl}} \left[\frac{\partial \boldsymbol{r}_{\text{i,cp}}^{\text{coupl}}}{\partial \boldsymbol{q}} \right]^{\text{T}} + \tilde{F}_{y_{\text{e}}}^{\text{am}} \left[\frac{\partial \boldsymbol{r}_{\text{i,cp}}^{\text{am}}}{\partial \boldsymbol{q}} \right]^{\text{T}} \right\} \boldsymbol{R}_{\text{e}\to\text{i}} \boldsymbol{e}_{y_{\text{e}}} dx_{\text{e}}, \tag{4.27}$$

with $\boldsymbol{r}_{\text{i,cp}}^{\text{trans}}$, $\boldsymbol{r}_{\text{i,cp}}^{\text{rot}}$, $\boldsymbol{r}_{\text{i,cp}}^{\text{coupl}}$ and $\boldsymbol{r}_{\text{i,cp}}^{\text{am}}$ representing the position vectors of the centers of pressure in the inertial frame. These vectors can be obtained by

$$\boldsymbol{r}_{\text{i,cp}}^{\oplus} = \boldsymbol{R}_{\text{e}\to\text{i}}[x_{\text{e}}, 0, -c\hat{d}_{\text{cp}}^{\oplus}]^{\text{T}}, \tag{4.28}$$

with the superscript "$\oplus$" referring to "trans", "rot", "coupl" or "am" for the different loading terms. The locations of the centers of pressure $\hat{d}_{\text{cp}}^{\text{trans}}$, $\hat{d}_{\text{cp}}^{\text{rot}}$, $\hat{d}_{\text{cp}}^{\text{coupl}}$ and $\hat{d}_{\text{cp}}^{\text{am}}$ are also provided in Chapter 2.

The first three components of $\boldsymbol{Q}^{\text{aero}}$ are functions of the generalized velocities, but the last term (i.e., the added-mass term) can be separated into two parts which are functions of the generalized velocities and accelerations, respectively. Therefore, $\boldsymbol{Q}^{\text{aero}}$ can be rewritten as

$$\boldsymbol{Q}^{\text{aero}} = \tilde{\boldsymbol{Q}}^{\text{aero}} - \boldsymbol{M}^{\text{am}}\ddot{\boldsymbol{q}}. \tag{4.29}$$

Here, $\tilde{\boldsymbol{Q}}^{\text{aero}}$ includes all the generalized velocity related terms, and $\boldsymbol{M}^{\text{am}}$ is the mass matrix related to the added-mass effect.

Substituting Eqs. 4.15, 4.22, 4.23 and 4.29 into the Lagrange's equation in Eq. 4.11, we can obtain the equations of motion for a twistable wing as in

$$\boldsymbol{M}\ddot{\boldsymbol{q}} = -\boldsymbol{Q}^{\text{ela}} + \boldsymbol{Q}^{\text{drive}} + \tilde{\boldsymbol{Q}}^{\text{aero}} - \boldsymbol{Q}_{\text{v}}, \tag{4.30}$$

where $\boldsymbol{M}(= \boldsymbol{M}^{\text{w}} + \boldsymbol{M}^{\text{am}})$ is the effective mass matrix.

4.2.3. KINEMATIC CONSTRAINTS

For insects and FWMAVs, there might exist kinematic constraints on the wing rigid-body rotations. For instance, the sweeping motion is generally controlled by a drive system, and a certain type of heaving motion or no heaving motion is generally enforced. If there are n_c rotational constraints, the number of independent generalized coordinates n_i will be $n + 4 - n_c$. The equations of motion given by Eq. 4.30 can be rewritten in a partitioned form as

$$\begin{bmatrix} \boldsymbol{M}_{n_c \times n_c} & \boldsymbol{M}_{n_c \times n_i} \\ \boldsymbol{M}_{n_i \times n_c} & \boldsymbol{M}_{n_i \times n_i} \end{bmatrix} \begin{bmatrix} \ddot{\boldsymbol{q}}_{n_c \times 1} \\ \ddot{\boldsymbol{q}}_{n_i \times 1} \end{bmatrix} = - \begin{bmatrix} \boldsymbol{0} \\ \boldsymbol{Q}^{\text{ela}}_{n_i \times 1} \end{bmatrix} + \begin{bmatrix} \boldsymbol{Q}^{\text{drive}}_{n_c \times 1} \\ \boldsymbol{0} \end{bmatrix} + \begin{bmatrix} \tilde{\boldsymbol{Q}}^{\text{aero}}_{n_c \times 1} \\ \tilde{\boldsymbol{Q}}^{\text{aero}}_{n_i \times 1} \end{bmatrix} - \begin{bmatrix} \boldsymbol{Q}^{\text{v}}_{n_c \times 1} \\ \boldsymbol{Q}^{\text{v}}_{n_i \times 1} \end{bmatrix}, \qquad (4.31)$$

of which the unknown terms are $\ddot{\boldsymbol{q}}_{n_i \times 1}$ and $\boldsymbol{Q}^{\text{drive}}_{n_c \times 1}$. Therefore, two set of equations can be obtained, namely

$$\boldsymbol{Q}^{\text{drive}}_{n_c \times 1} = \boldsymbol{M}_{n_c \times n_c} \ddot{\boldsymbol{q}}_{n_c \times 1} + \boldsymbol{M}_{n_c \times n_i} \ddot{\boldsymbol{q}}_{n_i \times 1} - \tilde{\boldsymbol{Q}}^{\text{aero}}_{n_c \times 1} + \boldsymbol{Q}^{\text{v}}_{n_c \times 1}, \qquad (4.32)$$

and

$$\boldsymbol{M}_{n_i \times n_i} \ddot{\boldsymbol{q}}_{n_i \times 1} = -\boldsymbol{Q}^{\text{ela}}_{n_i \times 1} + \tilde{\boldsymbol{Q}}^{\text{aero}}_{n_i \times 1} - \boldsymbol{Q}^{\text{v}}_{n_i \times 1} - \boldsymbol{M}_{n_i \times n_c} \ddot{\boldsymbol{q}}_{n_c \times 1}. \qquad (4.33)$$

The latter equation represents the set of independent equations of motion. The last term in its right-hand side refers to the Euler force due to the prescribed rotational acceleration. By solving Eq. 4.33, the motion of a twistable wing can be obtained. Substituting Eq. 4.33 into Eq. 4.32, we get

$$\boldsymbol{Q}^{\text{drive}}_{n_c \times 1} = \underbrace{\left[\boldsymbol{M}_{n_c \times n_c} - \boldsymbol{M}_{n_c \times n_i} \boldsymbol{M}^{-1}_{n_i \times n_i} \boldsymbol{M}_{n_i \times n_c} \right] \ddot{\boldsymbol{q}}_{n_c \times 1} - \boldsymbol{M}_{n_c \times n_i} \boldsymbol{M}^{-1}_{n_i \times n_i} \boldsymbol{Q}^{\text{v}}_{n_i \times 1} + \boldsymbol{Q}^{\text{v}}_{n_c \times 1}}_{\text{inertial terms}}$$
$$\underbrace{+ \boldsymbol{M}_{n_c \times n_i} \boldsymbol{M}^{-1}_{n_i \times n_i} \tilde{\boldsymbol{Q}}^{\text{aero}}_{n_i \times 1} - \tilde{\boldsymbol{Q}}^{\text{aero}}_{n_c \times 1}}_{\text{aerodynamic terms}} \underbrace{- \boldsymbol{M}_{n_c \times n_i} \boldsymbol{M}^{-1}_{n_i \times n_i} \boldsymbol{Q}^{\text{ela}}_{n_i \times 1}}_{\text{elastic terms}}, \qquad (4.34)$$

from which it can seen that $\boldsymbol{Q}^{\text{drive}}_{n_c \times 1}$ is used to accelerate/decelerate the wing, overcome the aerodynamic drag and resist the elastic force, as represented by the inertial, aerodynamic and elastic terms, respectively. In practice, $\boldsymbol{Q}^{\text{drive}}_{n_c \times 1}$ is the drive torque which is applied by the motor of FWMAVs or the thorax of insects. It can be used to determine the power consumption.

4.3. VALIDATION OF THE PROPOSED TWIST MODEL

To validate the proposed twist model, we set the span, aspect ratio and the mass of the rectangular wing as 50 mm, 2.5 and 50 mg, respectively, by referring to the adult hawkmoth (HMF2) (Willmott & Ellington, 1997b) and artificial wings of similar size (Bolsman *et al.*, 2009). The wing thickness is set as 1 mm. Here the average thickness of the wing of HMF2 (about 35 μm) is not referred to for two reasons. First, the average thickness is not adequate to reflect the real hawkmoth wing thickness distribution considering its morphological complexity. Second, the wing with prescribed dimensions and mass can be easily fabricated using a foam sheet (Expanded PolyStyrene) in case artificial wings are needed for futural experimental study. A harmonic sweeping motion, $\phi(t) = \phi_m \sin(2\pi f t)$, is applied to drive the wing, where the amplitude ϕ_m is set to 60°
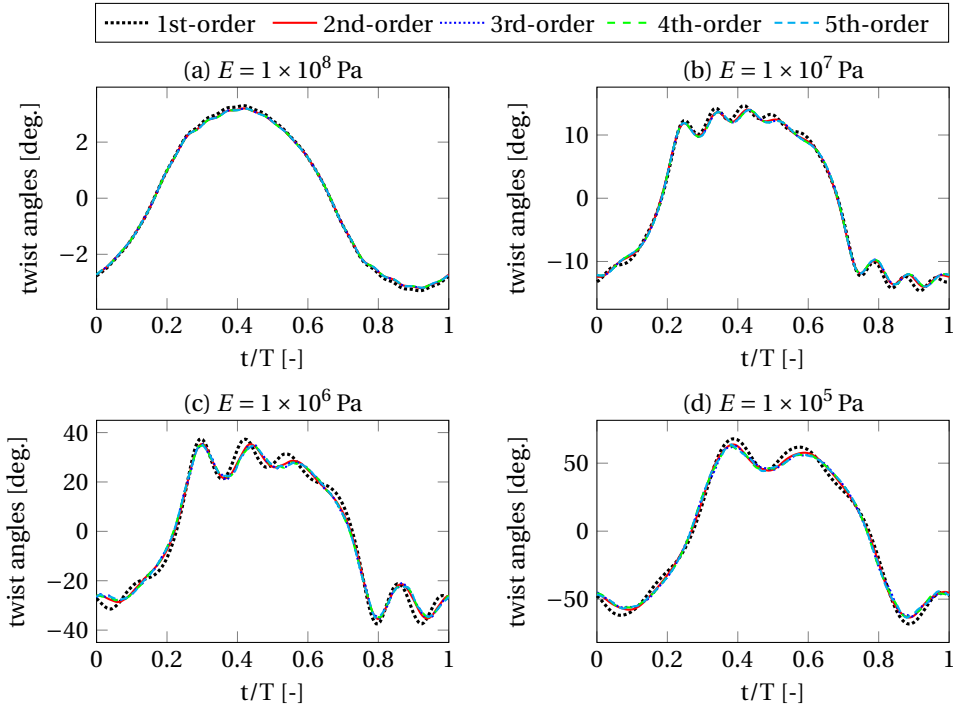
Figure 4.4: Comparison of the wing dynamic twist when different orders of polynomials (from the 1st- to the 5th-order) are used to describe the twist angle along the span. Wings with different Young's moduli are investigated from (a) to (d).

and f is the flapping frequency. The heaving motion is restricted, i.e., $\theta(t) = 0$. The wing pitches passively due to the inertial and aerodynamic loads. The wing stiffness is modeled as a combination of the stiffness k_η of a torsional spring at the wing root and the distributed stiffness of the wing plate. The distributed stiffness is controlled by the Young's modulus E.

The first step before application of the proposed fluid-structure interaction (FSI) model is to determine the proper polynomial order in Eq. 4.4 such that the wing twist can be accurately represented. Therefore, the frequency f and the stiffness k_η are temporarily set to 25 Hz and 5×10^{-4} Nm/rad, which are close to the values of the referred wings. To study different wing stiffnesses, the Young's modulus is set to 1×10^8 Pa, 1×10^7 Pa, 1×10^6 Pa and 1×10^5 Pa. For each case, the convergence of the dynamic wing twist is checked by increasing the polynomial order from 1st- to 5th-order, as shown in Fig. 4.4. It can be observed for all the cases that (1) the twist based on the linear model deviates slightly from higher order twist models, and (2) the differences between the quadratic twist model and higher order twist models are negligible. The marginal contribution of twist modes that are higher than 2nd-order can be explained by the fact that the inertial and aerodynamic loads increase roughly linearly and quadratically from the wing root to the tip, respectively. Therefore, the quadratic polynomial is used for studying the rect-
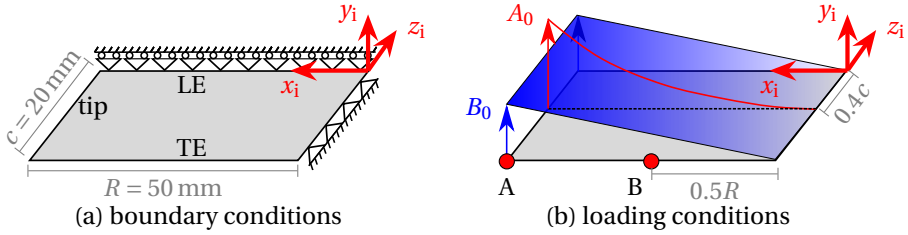
(a) boundary conditions   (b) loading conditions

Figure 4.5: Boundary conditions and loading cases of the rectangular plate used for validating the proposed plate model. (a) The boundary conditions are applied on the leading edge (LE) and the root chord of the middle surface. (b) Two loading cases are considered. The aerodynamic load, which is applied at the 40% chord line, increases quadratically from zero at the root to A_0 at the tip. The inertial load distributes uniformly along the chord direction and linearly increases from zero at the root to B_0 at the tip. The points A and B are located at the tip and middle of the trailing edge (TE), respectively.

angular wing twist. The corresponding degrees of freedom are the twist angles of the chords at the half-span and the tip, i.e., q_1^{ela} and q_2^{ela}. Combining this quadratic twist description and the wing tip displacement $u_{x_c}^{\text{tip}}$, the elastic displacement of the entire wing can be analytically described by Eq. 4.3.

In addition to the analytical description of the wing elastic displacement, the proposed twist model uses the nonlinear strain-displacement relations as given by Eq. 4.20. To validate the proposed twist model, especially for large twist, we calculate and compare the twist using both the proposed model and a finite element analysis (FEA) using COMSOL Multiphysics® software. In FEA, quadratic hexahedral elements ($2 \times 40 \times 100$) are used. For both the FEA and the proposed model, linear elasticity is assumed, and Newton method is used to solve the nonlinear equations. Based on the analytical displacement description in Eq. 4.3, the boundary conditions for the FEA can be obtained, as illustrated in Fig. 4.5 (a). All the boundary conditions are applied at the edges of the wing's middle surface. Two types of loads are considered as shown in Fig. 4.5 (b). The aerodynamic load, which is applied at the 40% chord line, increases quadratically from zero at the root to A_0 at the tip. The 40% chord line is chosen to roughly represent the chordwise aerodynamic load center which might vary from the 1/4 chord to the 1/2 chord in reality (Han *et al.*, 2015). The inertial load distributes uniformly along the chord direction and linearly increases from zero at the root to B_0 at the tip. This load results from the acceleration of the sweeping motion, which can be dominant as compared to other inertial terms (Ennos, 1989). Using these loads, three static loading cases are studied for the validation. Case (a) considers the aerodynamic load with $A_0 = 6 \times 10^{-2}\,\text{N/m}$, while Case (b) includes the inertial load with $B_0 = 2\,\text{N/m}^2$. Case (c) considers both the aerodynamic and inertial loads with A_0 and B_0 being equal to $3 \times 10^{-2}\,\text{N/m}$ and $1\,\text{N/m}^2$, respectively. The values of A_0 and B_0 guarantee the same resultant force for all the three cases.

For the three loading cases, the out-of-plane displacements u_{y_c} at the tip and middle of the TE (i.e., the points A and B in Fig. 4.5 (b)) are compared for the values obtained
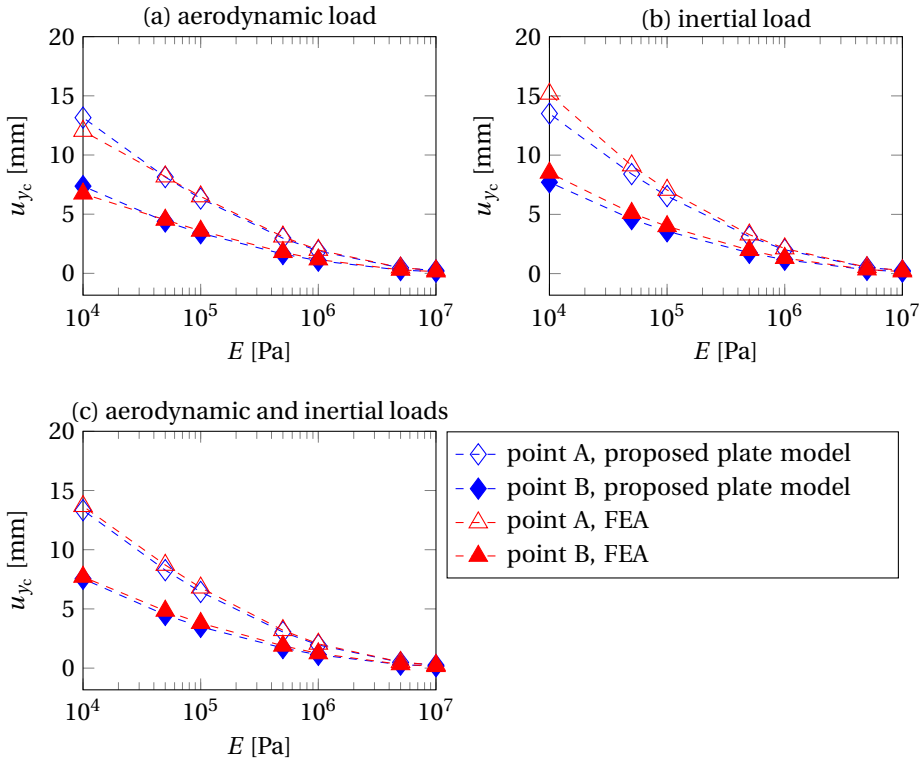
Figure 4.6: Comparison of the out-of-plane displacements u_{y_c} of statically loaded plates based on the proposed analytical plate model and the FEA using COMSOL Multiphysics® software. Three loading cases are considered. (a) The aerodynamic load with $A_0 = 6 \times 10^{-2}$ N/m is applied. (b) The inertial load with $B_0 = 2$ N/m² is applied. (c) Both the aerodynamic and inertial loads are applied. The values of A_0 and B_0 are equal to 3×10^{-2} N/m and 1 N/m², respectively. The values of A_0 and B_0 guarantee the same resultant force for all the three cases.

by the proposed model and the FEA. It can be seen from Fig. 4.6 that, for Case (a), the maximum errors at point A and B are about 15% and 11%, respectively, while for Case (b) they are around 11% at both locations. The errors for these two cases provide the extreme scenarios of the validity of the proposed plate model. Case (c) considers both the inertial and aerodynamic loads, and the maximum errors are only about 5% and 10% at point A and B, respectively. It is worth mentioning that the maximum twist angles for three loading cases are quite large (between 40° and 50°). The good accuracy of the proposed plate model for large twists can be attributed to the consideration of the wing shorting effect and the inclusion of the quadratic membrane terms in the strain-displacement relations. The errors are mainly induced by two assumptions used in the proposed twist model. First, the spanwise displacement is enforced to change linearly from the root

to the tip. Second, the chordwise stretching and camber are ignored. In contrast, the FEA shows a more complicated spanwise displacement field due to the varying spanwise shortening from the LE to the TE. Meanwhile, significant camber can be observed when the wing is subject to the prescribed aerodynamic loads.

4.4. TWIST OPTIMIZATION

The proposed twist model and the quasi-steady aerodynamic model dramatically reduce the computational cost for the FSI analysis as compared to traditional FSI models. In our FSI simulations, the wing is discretized into 50 chordwise strips, which are adequate for the description of the quadratic wing twist. The wing's passive pitching motion normally starts to converge to its steady state from the second half of the first cycle. The aerodynamic force and power consumption in the third cycle are used for analysis and optimization. Newmark method with $\gamma = 1/2$ and $\beta = 1/4$ is used to solve the equations of motion while 500 time steps are taken for each cycle. Each simulation takes about only 4 minutes when using MATLAB® R2014b on a 64-bit computer with a RAM capacity of 8 GB and an Intel® Core™ i5 CPU at 3.40 GHz.

4.4.1. OPTIMIZATION MODEL

The proposed FSI model will be used to optimize the wing twist and kinematics which minimize the cycle-averaged power consumption during hovering flight. The design variables include the root stiffness k_η, the Young's modulus E and the flapping frequency f. The power can be calculated by

$$P^{\text{total}} = \dot{\boldsymbol{q}}_{n_c \times 1}^{\text{T}} \boldsymbol{Q}_{n_c \times 1}^{\text{drive}},$$
(4.35)

where $\boldsymbol{Q}_{n_c \times 1}^{\text{drive}}$ and $\dot{\boldsymbol{q}}_{n_c \times 1}$ are the drive torque and generalized velocity, respectively. Similar to Eq. 4.34, the total power can be decomposed into three components, namely the aerodynamic power P^{aero}, inertial power P^{iner} and the elastic power P^{ela}. Note, the power can be negative due to the loss of the kinetic energy during the deceleration. The lost kinetic energy can be dissipated, used to compensate the energy consumed by the aerodynamic drag, or stored in a kinetic energy recovery drive system (KERS). KERS can appear in different forms, e.g., insect thoraxes (Dudley, 2002) and elastic structures of FWMAVs (Bolsman *et al.*, 2009, Lau *et al.*, 2014). The uncertainty in the kinetic energy transformation complicates the modeling of the average power consumption. Instead, two extreme power consumption scenarios are modeled. First, an ideal KERS is used, which implies that the average elastic and inertia power are both zero. In this setting, the total average power is equal to the average aerodynamic power, i.e.,

$$\bar{P}_{\text{KERS}}^{\text{total}} = \frac{1}{T} \int_T P^{\text{total}} dt = \frac{1}{T} \int_T P^{\text{aero}} dt,$$
(4.36)

with T representing the period of a flapping cycle. Second, a drive system which can not recover any energy is adopted. In this case, the kinetic and elastic energy first compensate the energy consumed by drag. Then, extra energy will be dissipated. This type of drive system will be referred to as non-KERS. The total average power for this extreme

case can be calculated by

$$\bar{P}^{\text{total}}_{\text{non-KERS}} = \frac{1}{T} \int_T \Xi\left(P^{\text{total}}\right) dt, \tag{4.37}$$

where $\Xi(\bullet)$ is an operator which sets negative values to zero but keeps positive values. In practice, the power consumed by flapping wings lies between $\bar{P}^{\text{total}}_{\text{KERS}}$ and $\bar{P}^{\text{total}}_{\text{non-KERS}}$.

For convenience, the optimization with three design variables (i.e., f, k_η and E) is denoted as the "full optimization". In addition, two other optimization cases are studied. One case prescribes the flapping frequency and optimizes the values of k_η and E, while the second case prescribes the root stiffness and optimizes the values of f and E. For all cases, the same objective function and lift constraint are used. By referring to wings of similar size (Willmott & Ellington, 1997b, Bolsman *et al.*, 2009), the required average lift is set to 1 g per wing. The optimized twistable wings will be compared with the corresponding optimized rigid wings for all the cases.

4.4.2. Optimization results and analysis
In the following three subsections, the optimal wing designs for KERS are studied. At the end of this section, the optimal designs for KERS and non-KERS will be compared.

Case 1: full optimization
Previous studies (Du & Sun, 2008, 2010, Nakata & Liu, 2012a,b, Dai *et al.*, 2012) show that twistable flapping wings can outperform their rigid counterparts in terms of power efficiency during hovering flight. However, the kinematics of the rigid counterparts was generally not optimized. In contrast, we optimize the flapping frequency and wing stiffness for both twistable and rigid wings and compare the resulting power efficiency. The design parameters for twistable wings are f, k_η and E, while f and k_η are optimized for rigid wings.

Optimization results show that the cycle-averaged power consumption for optimized twistable and rigid wings are 39.77 W/kg and 40.57 W/kg, respectively. The power has been normalized by the lift generation per kilogram. The improvement in power efficiency by incorporating twist is about 2 percents. In contrast, more considerable improvements were reported in previous studies which normally provide comparisons of unoptimized twistable and rigid wings. For KERS, the total power is equal to the aerodynamic power which is proportional to the drag and the flapping velocity. Therefore, in order to explain the marginal difference in power efficiency, both the optimal pitching motion and the corresponding aerodynamic forces are compared for the optimized twistable and rigid wings.

The pitching motion of the optimized wings is compared in Fig. 4.7. It can be observed that the optimized rigid wing pitches at a high amplitude (77.56°). The resultant aerodynamic force is regarded to be perpendicular to the chord throughout a flapping cycle. Thus, the higher pitching amplitude leads to a higher cycle-averaged lift-to-drag ratio. Since the average lift has been fixed, a higher lift-to-drag ratio implies a lower average drag. For the twistable wing, the optimal design has a root stiffness of 2.88×10^{-4} Nm/rad and Young's modulus of 3.67×10^6 Pa. The root stiffness is slightly larger than the optimal stiffness of the rigid wing (2.39×10^{-4} Nm/rad), which leads to a
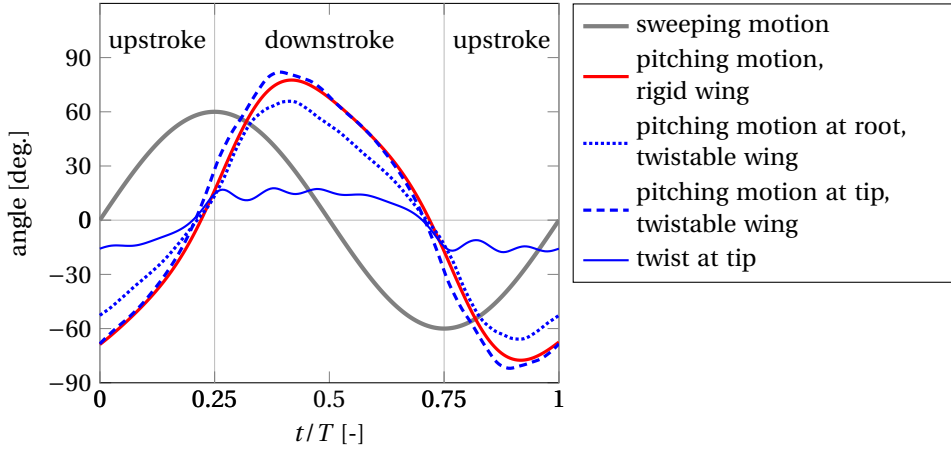
Figure 4.7: Comparison of the pitching motion for the optimized twistable and rigid wings.
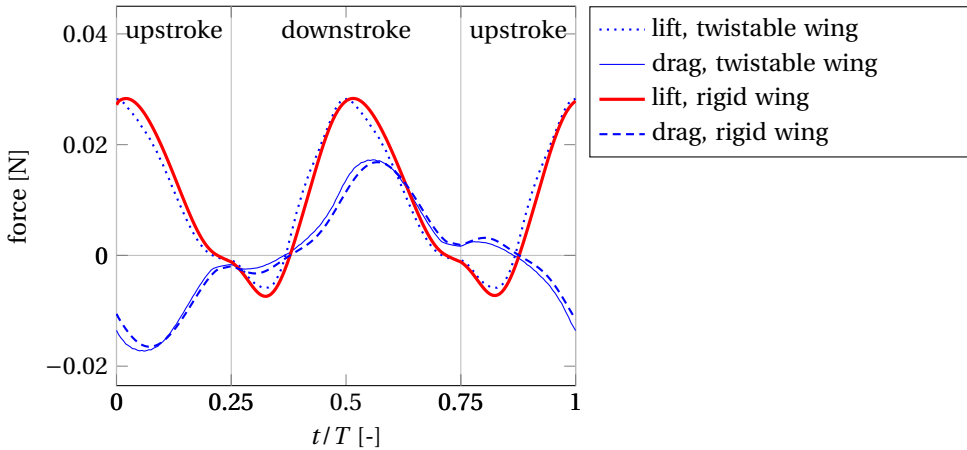

Figure 4.8: Comparison of the lift and drag generated by the optimized twistable and rigid wings.

slightly lower pitching amplitude at the root of the twistable wing as shown in Fig. 4.7. However, with the help of the wing flexibility, a twist with an amplitude of 17.68° exhibits for the optimized twistable wing. Due to the twist, the pitching amplitude at the tip is higher than the optimized rigid wing. Nevertheless, Figure 4.8 shows that the wing twist does not dramatically change the lift and drag profiles. Furthermore, the optimum frequency for the twistable wing and the rigid wing are 20.24 Hz and 20.63 Hz, respectively. The comparable drag profiles and flapping frequencies of the optimized twistable and rigid wings explain the marginal difference in power efficiency.

The power history for the optimized twistable and rigid wings is compared in Fig. 4.9. The most obvious difference is that the power for the rigid wing is very smooth while
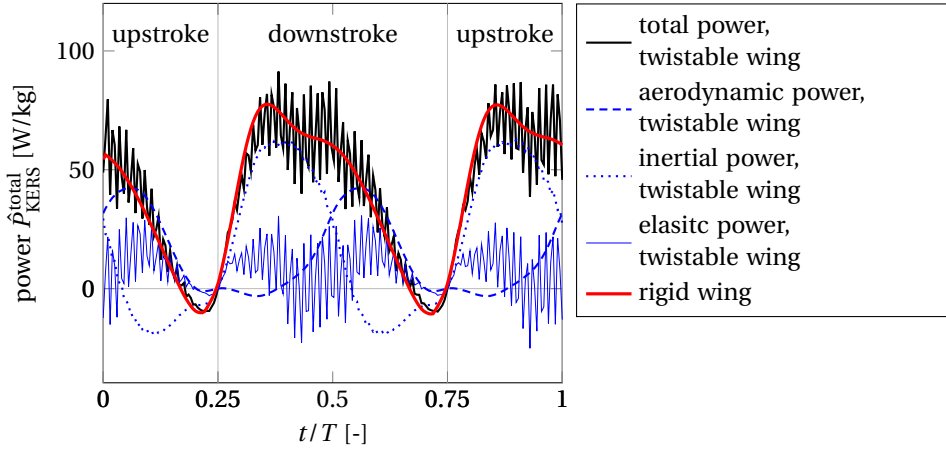
Figure 4.9: Comparison of the power history of the optimized twistable and rigid wings.

there exist high frequency oscillations for the twistable wing. From the decomposition of the total power for the twistable wing, we can see that the high frequency component originates from the elastic power. The elastic power is partially used to deform the wing in spanwise direction. Due to the high axial stiffness, the highest undamped eigen-frequency of the optimized twistable wing is about 80 times the optimum flapping frequency. Moreover, this high frequency spanwise motion is hardly damped since the aerodynamic load acts perpendicular to the spanwise axis. Therefore, it is not surprising to see the high frequency components of the elastic power and, thus, the total power.

When an optimized twistable or rigid wing is adopted, the flapping frequency might deviate from the optimum for maneuvering. Thus, Fig. 4.10 shows the sensitivity of the power consumption and lift generation of twistable and rigid wings with respect to the frequency when all the other parameters are fixed at their optimal values. It can be observed that the effects of the frequency on the power efficiency are comparable between twistable and rigid wings for a KERS drive system. However, the lift generation can be increased by driving the optimized twistable wing with a higher frequency, while there is hardly any potential for the optimized rigid wing to increase lift generation by changing the frequency. The difference underlines the advantage of the twistable wing in terms of flight control.

CASE 2: OPTIMIZATION OF WINGS WITH PRESCRIBED FREQUENCIES
The drive frequency of a FWMAV can significantly deviate from the optimum frequency due to hardware limitations, control operations and payload change. Therefore, it is useful to study the influence of wing twist on power efficiency when the flapping frequency is prescribed differently from the optimum drive frequency (i.e., 20.24 Hz). In this subsection, we optimize k_η for the rigid wings and both k_η and E for twistable wings. The wings will be driven at different frequencies that range from 20 Hz to 30 Hz with a step size of 1 Hz.

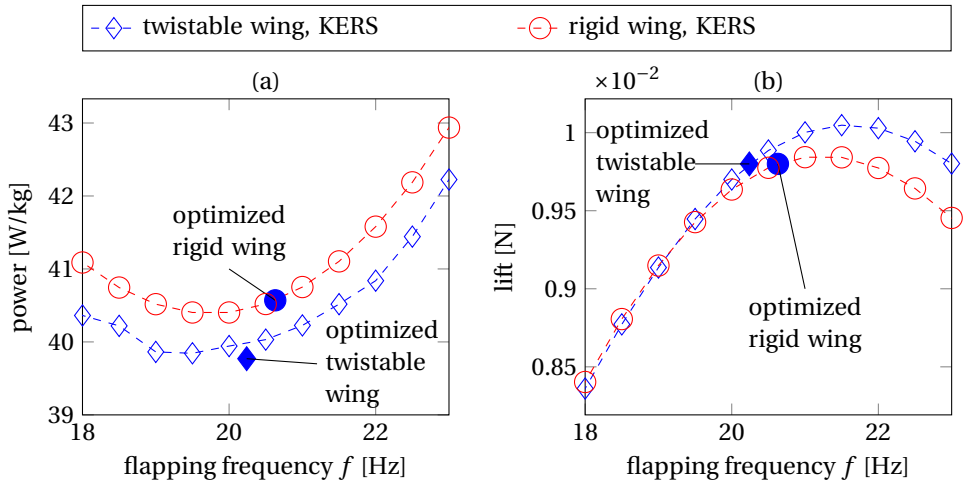The power efficiency and optimal designs are compared in Fig. 4.11. It can be seen

Figure 4.10: Sensitivity of the power consumption and lift generation of twistable and rigid wings with respect to the flapping frequency when the other parameters are fixed at their optimal values. A KERS drive system is used.

from Fig. 4.11 (a) that when the drive frequency is fixed at different non-optimal values, the power saved by the optimized twistable wings is very limited when compared to corresponding rigid wings. Meanwhile, the drive frequency can dramatically change the power consumption of optimized wings. Figure 4.11 (b) shows that the pitching amplitudes of the optimized rigid wings are between the pitching amplitudes at the root and the tip of the corresponding optimized twistable wings. The difference of the pitching motion of the optimized twistable and rigid wings for different drive frequencies are quite similar to what we have shown in Fig. 4.7.

Figures 4.11 (c) and (d) show the wing root stiffness and the Young's modulus of the optimized wings. It can be seen from Fig. 4.11 (c) that the root stiffness of optimized twistable wings is always higher than for corresponding rigid wings, which results in lower pitching amplitudes at the root of the twistable wings. In addition, the optimal root stiffness (Fig. 4.11 (c)) for the rigid wings changes smoothly with the frequency. However, both the wing root stiffness (Fig. 4.11 (c)) and Young's modulus (Fig. 4.11 (d)) for the twistable wings are non-smooth. In contrast, the resulting power consumption for the optimized twistable wings is quite smooth. To explain this, we plot the contour lines of the lift and power as a function of the root stiffness and Young's modulus. It can be observed that, near the optimal design, the lift contour line with a value equal to the required lift generation is approximately parallel to the contour lines for power consumption. This indicates that twistable wings with different combinations of root stiffness and Young's modulus can have similar power efficiency. This phenomenon can be explained by the fact that both the change of root stiffness and the Young's modulus can alter the overall pitching motion and, thus, the aerodynamic power. Furthermore, the freedom on choosing the root stiffness and Young's modulus provides more space for the power-efficient wing designs.
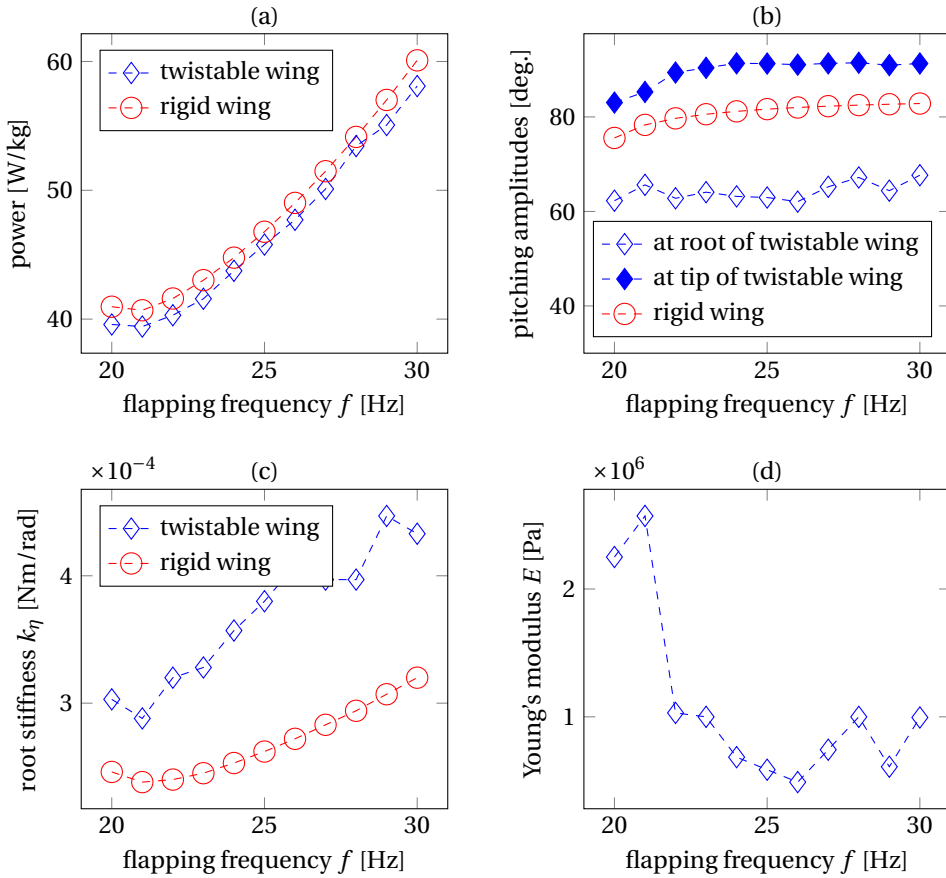
Figure 4.11: Comparison of optimized twistable and rigid wings when the drive frequency is fixed at different values.

CASE 3: OPTIMIZATION OF WINGS WITH FIXED ROOT STIFFNESS

In nature, some insects use pitching motion with high amplitudes but small twist, while others show very small pitching amplitudes at the wing root but large twist. These observations imply that the usefulness of wing twist might be related to the pitching motion at the root. Therefore, we investigate the power efficiency of optimized twistable wings when different values of the root stiffness are used. In this subsection, we optimize f for the rigid wings and both f and E for twistable wings when the root stiffness varies from 3×10^{-4} Nm/rad to 1×10^{-3} Nm/rad with a step size of 1×10^{-4} Nm/rad.

The comparison of the optimized twistable and rigid wings is shown in Fig. 4.13. From Fig. 4.13 (a) and (b), it can be observed that both the power consumption and the flapping frequency for optimized rigid wings approximately increase linearly with the root stiffness. In contrast, both the power consumption and the frequency only show a slight increase for optimized twistable wings. Figure. 4.13 (c) shows that the pitching amplitude of the optimized rigid wings decreases with the root stiffness, while the twist
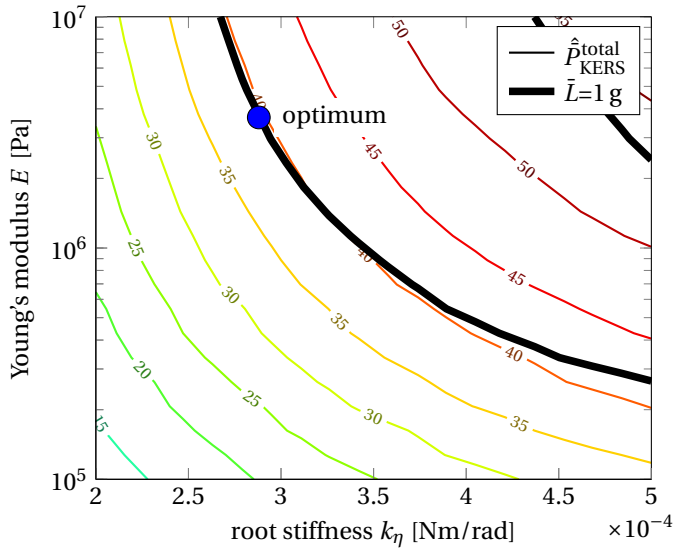
Figure 4.12: Contour plots of the lift and the power consumption as a function of the root stiffness and Young's modulus. The lift acts as a constraint in the optimization. The lift constraint is included as a thick solid line. The blue dot represents the wing stiffness of the optimized twistable wing based on the full optimization.

angle of the optimized twistable wing increases. To increase the twist angle for twistable wings, the Young's modulus needs to decrease, as demonstrated in Fig. 4.13 (d).

The different responses of the power consumption with the increase of the root stiffness can be explained by combining the optimal flapping frequency and the pitching amplitudes as shown in Fig. 4.13 (b) and (c), respectively. As explained in Sec. 4.4.2, the decreasing pitching amplitude tends to increase the average drag, and the increase of the drive frequency tends to increase the flapping velocity. Increase of the average drag and the flapping velocity both lead to higher power consumption for optimized rigid wings. For optimized twistable wings, the increases of the twist and the drive frequency have an opposite effect to the power efficiency. Therefore, the power consumption of optimized twistable wings does not change dramatically for different root stiffness.

The optimization results can be also interpreted from the perspective of lift generation. For rigid wings, due to the decrease of the pitching amplitude, the lift coefficient tends to get lower. In order to maintain sufficient lift generation, the flapping frequency needs to increase. In contrast, wing twist helps to maintain the overall angle of attack when the pitching amplitudes at the root gets lower due to an increase of the root stiffness. As a result, the optimal frequency of the optimized twistable wing does not change as much as for rigid wings.
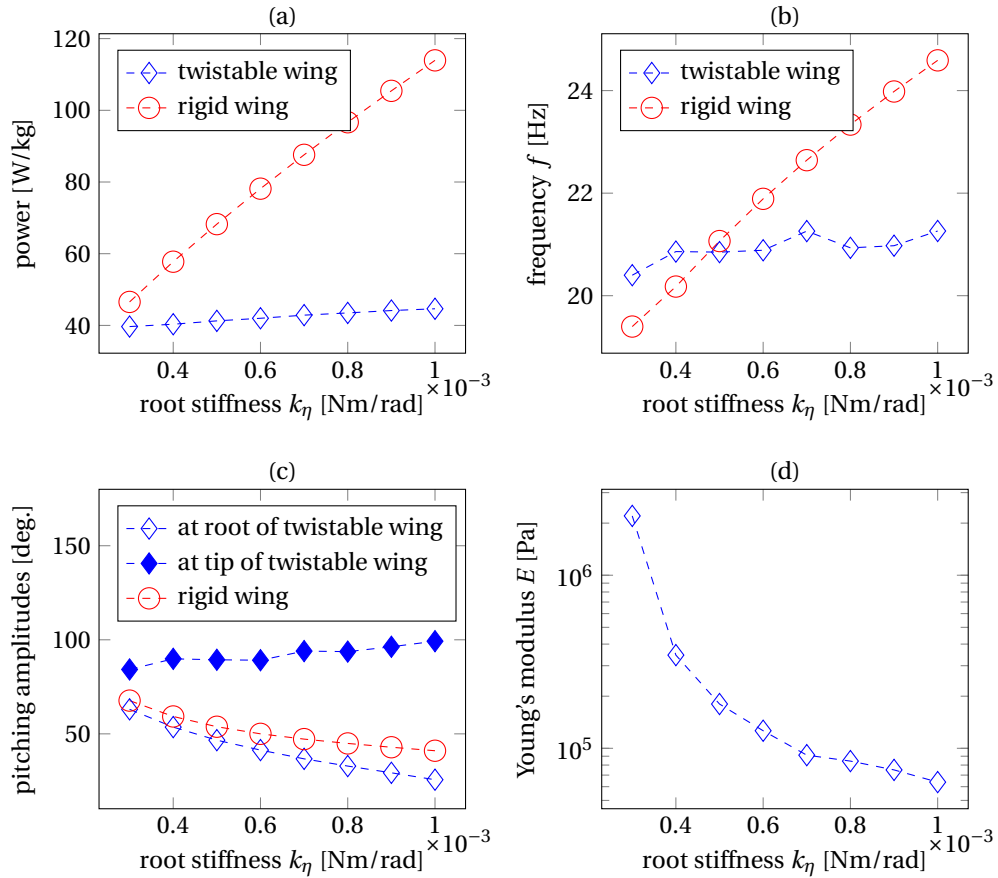
Figure 4.13: Comparison of the optimized twistable and rigid wings when the root stiffness is fixed at different values.

COMPARISON BETWEEN KERS AND NON-KERS

The studies in the previous subsections assumed a KERS drive system. For a non-KERS drive system, the optimal frequencies for fully optimized twistable and rigid wings, similar to the study in Case 1, are 20.65 Hz and 20.70 Hz, respectively. The corresponding power consumptions are 40.47 W/kg and 41.64 W/kg. The improvement in power efficiency by incorporating twist is about only 3 percents, which is close to the value for KERS (about 2 percents). Figure 4.14 shows the sensitivity analysis of the power consumption and lift generation with respect to the flapping frequency when the other parameters are fixed at their optimal values. It can be observed that the power efficiency of twistable wings is getting closer to the rigid wings when the frequency increases from the optimal values. The corresponding increase of lift for twistable wings is marginal, which is different from the effect for the KERS system.

In Fig. 4.15, we compare the power efficiency of optimized wings for KERS and non-KERS when the drive frequency or the root stiffness is prescribed, similar to Cases 2 and
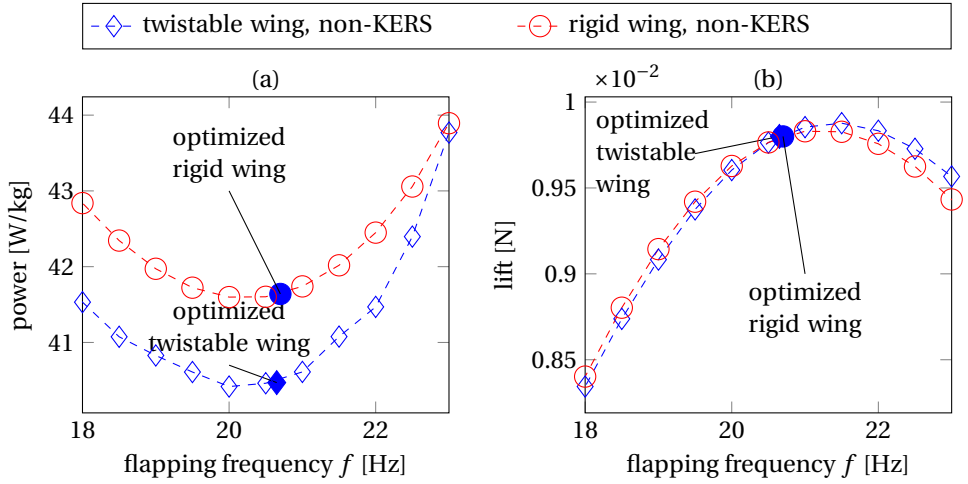
Figure 4.14: Sensitivity of the power consumption and lift generation of twistable and rigid wings with respect to the flapping frequency when the other parameters are fixed at their optimal values. A non-KERS drive system is used.
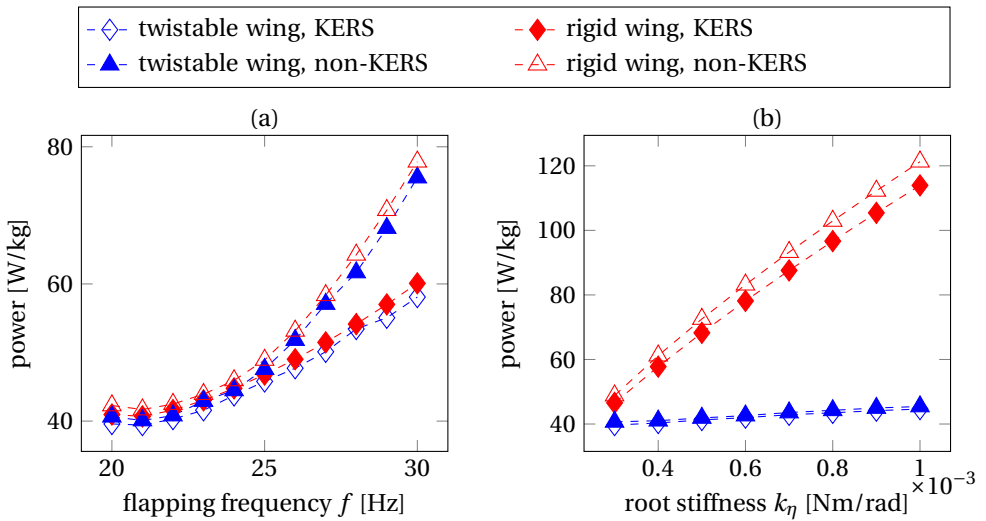
Figure 4.15: Comparison of power efficiency of optimized wing designs for KERS and non-KERS drive systems. (a) The flapping frequency is fixed at different values. (b) The root stiffness is prescribed.

3 as studied in the previous subsections. From Fig. 4.15 (a), it can be observed that KERS and non-KERS show very similar power efficiency when the frequency is close to the optimum (i.e., 20.24 Hz). However, when the drive frequency significantly deviates from the optimum, the difference of the power consumption becomes more considerable. For

instance, when the frequency is fixed at 30 Hz, the optimized twistable wing can save about 23% of the power for KERS as compared to non-KERS. Figure 4.15 (b) shows that, for the optimized twistable wings, the power efficiency does not change significantly with the prescribed root stiffness when a non-KERS system is used. This is similar to the observation for KERS. Meanwhile, the difference between the power consumed for KERS and non-KERS are negligible for all the root stiffness. For optimized rigid wings, the difference between the power consumed by KERS and non-KERS slightly increases with the root stiffness but still not very pronounced.

4.5. CONCLUSIONS

We have proposed a computationally efficient Fluid-Structure Interaction (FSI) model to enable the parametric study and optimization of flapping wing twist and corresponding kinematics. The proposed FSI model relies on an analytical twist model and a quasi-steady aerodynamic model. The twist model uses a polynomial to describe the change of the twist angle along the span. The spanwise shortening effect and the quadratic strain-displacement relations for the wing membrane deformation have been included to guarantee accuracy for large twist. It has been shown for rectangular wings that a quadratic polynomial can accurately model the twist at large amplitudes. Moreover, the proposed twist model and the quasi-steady aerodynamic model enable full FSI analysis in just a few minutes, which demonstrates the computational efficiency of the proposed FSI model.

Based on the proposed FSI model, we have optimized the stiffness and flapping frequency for both rigid and twistable wings to minimize the power consumption for hovering. Comparisons show that the optimized twistable wings exhibit power efficiency close to the optimized rigid wings, unless the pitching amplitude at the wing root is limited. When the pitching amplitude at the root decreases by increasing the root stiffness, the optimized rigid wings need more power for hovering. However, the power efficiencies of optimized twistable wings with different prescribed root stiffness are comparable with the twistable wings with optimal root stiffness. This observation provides an explanation for the different levels of twist demonstrated by insect wings. The computational efficiency of the proposed FSI model allows parametric study and optimization of flapping wings to enhance the understanding of insect wing flexibility and may help the design of flexible artificial wings for FWMAVs.

5

ACTIVE ELASTIC WING HINGE DESIGN BASED ON ELECTROSTATIC STICKING

In previous chapters, we have shown that a proper root stiffness is essential for flapping wings to achieve optimal passive pitching motion. Since the required root stiffness changes with the lift constraint, an elastic hinge with a tunable stiffness is helpful for a wing design to change its pitching motion when the required lift changes.

This chapter studies an elastic hinge design consisting of stacked layers which can be sticked together using electrostatics. After the introduction, the passive pitching flapping motion is described in Sec. 5.2. Next, the voltage-dependent behavior of this elastic hinge during the large pitching motion is described in detail in Sec. 5.3. After that, the equation of motion that governs the passive pitching motion is formulated as a function of the hinge stiffness and the applied control voltage (see Sec. 5.4). In Sec. 5.5, experiments are conducted to study the practical applicability of this method on FWMAVs. The experimental results are compared with the numerical simulations in Sec. 5.6. As concluded in Sec. 5.7, the proposed hinge design is able to change the hinge stiffness, and it is a promising approach for flapping wing flight control with refined fabrication techniques.

5.1. INTRODUCTION

The design and realization of lightweight Flapping Wing Micro Air Vehicles (FWMAVs) have attracted much attention over the last decades. Potential applications of FMWAV designs are in, among others, surveillance (e.g., police and security) and inspection of inaccessible or dangerous locations (e.g., disaster scenes and sewers). The design and realization of FWMAVs is complicated by weight constraints as a result of the limited lift production of the wings. Consequently, designers aim for lightweight, smart and highly integrated systems. This has resulted in several ways of achieving flapping kinematics for sufficient lift production. To decrease the actuation mechanism complexity, some wing designs integrate elastic hinges that allow the wing pitching motion to be passive during the flapping motion (Bolsman *et al.*, 2009, Wood, 2008). Due to the inertial and aerodynamic loads, a properly tuned elastic hinge results in the required pitching motion to achieve enough lift production to stay aloft.

For stable flight and maneuvering, FWMAV designs require some form of control. In fact, constant control will be necessary because of the intrinsic dynamic instability of the designs. Recent work on the Harvard Robobees (i.e., a FWMAV design which exploits passive pitching) applied aerodynamic dampers for stabilization (Teoh *et al.*, 2012), complex mechanisms to induce asymmetric flapping wing kinematics to produce control torques (Finio & Wood, 2012), and separate actuators for each wing (Ma *et al.*, 2012). Additionally, control torques were created by integrating a piezoelectric bimorph actuator in the wing elastic hinge to induce a bias during the wing stroke (Teoh & Wood, 2014). To control lightweight FWMAV designs, actively adjusting the dynamic properties (i.e., structural damping and stiffness) of the wing elastic hinge appears to be a promising, elegant, and integrable approach to change the passive pitching motion during flight and, hence, the stroke-averaged lift force. This control approach is not well established within literature.

To actively change the dynamic properties of the wing elastic hinge, the hinge needs to be replaced by an active hinge which properties change due to some external stimuli (e.g., an electric field). Methods to actively change the dynamic properties of an elastic element are, for example: (1) smart fluids (i.e., magnetorheological or electrorheological fluids) for which the properties transform rapidly upon exposure to an external magnetic or electric field (Majidi & Wood, 2010), (2) piezoelectric polymer films (e.g., PVDF) for which the properties change as a function of the connected electrical circuit (Clark, 2000), and (3) sticking stacked layers using, for example, electrostatics (Bergamini *et al.*, 2006, Tabata *et al.*, 2001).

This chapter investigates the method with the stacked layers for which the conceptual idea is shown in Fig. 5.1. Figure 5.1(a) shows a capacitor-like clamped-free beam which consists of two layers which can slide with respect to each other when deflected by the end-load F. Each layer consists of a conducting layer (e.g., spring steel) and a dielectric layer (e.g., Mylar). Figure 5.1(b) shows that, during deflection, the two layers slip with respect to each other if the applied voltage $V = 0$. For a specific voltage V_{st}, the electrostatic loading causes the layers to stick to each other during deflection, see Fig. 5.1(c). Whenever these layers stick, the second moment of area increases, which effectively increases the bending stiffness of the beam.

This chapter aims to actively control the wing's passive pitching motion by sticking
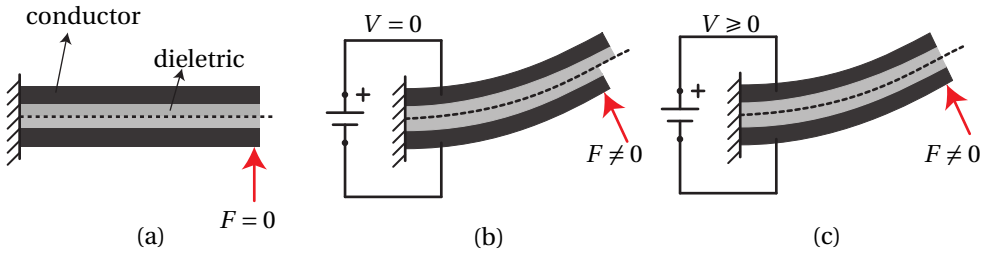
Figure 5.1: Conceptual idea to change the bending stiffness of stacked layers. (a) Capacitor-like clamped-free beam with end-load F. (b) For $V = 0$, the layers slip with respect to each other during deflection. (c) For $V \geq V_{st}$, the layers stick together which effectively increases the bending stiffness.

stacked layers using electrostatics. These stacked layers need to be integrated into a lightweight wing design (i.e., total wing design is about 200 mg) and should allow for large passive pitching deflections. This study investigates the influence of electrostatics on the dynamic properties of this active hinge during these large deflections. The wing is assumed to be a thin, rigid plate for simplicity. This work uses a quasi-steady aerodynamic model to obtain the equation of motion of the passive pitching motion as a function of the elastic hinge properties. Experiments are conducted to study the practical applicability of this active element for small-scale and lightweight FWMAV applications.

5.2. PASSIVE PITCHING FLAPPING MOTION

5.2.1. FLAPPING WING DESIGN

Both insects and FWMAVs show flapping wings with different outlines, stiffness distributions and materials. Generally, the pitching motion is partly generated passively with the help of wing flexibility. This wing flexibility can, for instance, be realized with: (1) a flexible veins-membrane structure as known from insect wings (Dudley, 2002), (2) a carbon-fiber-reinforced polymer film as commonly used in FWMAV wing designs (de Croon *et al.*, 2009), or (3) an elastic hinge at the wing root to represent the wing stiffness (Wood, 2007). This work uses the latter approach which is generally used for experimental studies.

Figure 5.2 shows the wing design as studied in the present work, consisting of a rectangular, thin plate which is assumed to be rigid. The mass distribution over the wing surface is assumed to be uniform. Since the focus of the current work is primarily on the active hinge design, such a simple wing layout design is justified. The wingspan and chord length are denoted by R and c, respectively. The elastic hinge is located at the wing root and has width b, length L and thickness t. This elastic hinge is essentially a compliant hinge, which is primarily loaded in bending. The effective rotational stiffness can, consequently, be given by (Howell, 2001)

$$k_\eta = \frac{E^h I^h}{L},$$ (5.1)

where E^h and I^h are the Young's modulus and second moment of area of the hinge, re-
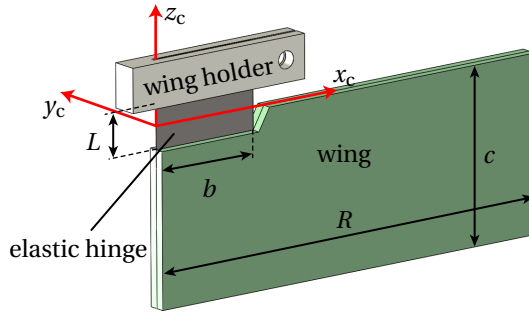
Figure 5.2: Schematic drawing of the wing design for a zero pitching angle with the elastic hinge connecting the wing holder to the wing.

spectively. Figure 5.3 shows a schematic side-view of the wing design which is rotated through an angle η to visualize the result of replacing the compliant elastic hinge with length L by a rotational spring with stiffness k_η. For pure bending, this simple equation is accurate for large deflections. Although the loading of the elastic hinge is more complex during the flapping motion, Eq. 5.1 is assumed to hold during the entire flapping cycle.
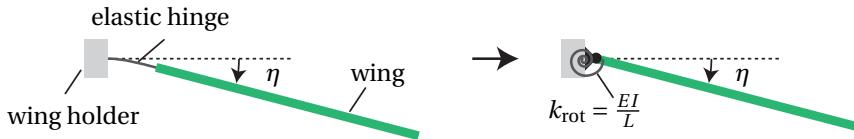

Figure 5.3: Side-view sketch of the wing design, rotated through an angle η, showing the replacement of the compliant elastic hinge with length L by a rotational spring with stiffness k_η.

5.2.2. PASSIVE PITCHING AND WING KINEMATICS

The flapping wing motion is a spatial wing movement that can be decomposed into three successive motions, namely sweeping motion (yaw), pitching motion (pitch), and heaving motion (roll). The sweeping motion drives the wing to sweep reciprocally in a stroke plane with a specified stroke amplitude. The pitching motion controls the geometrical angle of attack (AOA) of the flapping wings. For flapping wings, the highest AOA (i.e., 90°) is, generally, experienced during wing reversal phases while the lowest AOA shows up during the middle of the strokes. The heaving motion represents the out-of-stroke-plane movement which amplitude is generally one order smaller than for the other two motions. Hence, it is ignored in this study. Therefore, the flapping kinematics can be fully determined by the sweeping motion and the pitching motion.

Two Euler angles are used to quantify the wing kinematics: the sweeping angle ϕ, and the pitching angle η. The pitching angle η is visualized in Fig. 5.3. Additionally, two coordinate frames are specified which are of particular interest for the study of flapping

wing motion: the fixed inertial frame $x_i y_i z_i$ and the co-rotating frame $x_c y_c z_c$ which co-rotates with the wing (see Fig. 5.2). The angular velocity and acceleration of a flapping wing in the co-rotating frame can be expressed by

$$\boldsymbol{\omega}_c = \left[\dot{\eta}, \dot{\phi}\sin(\eta), \dot{\phi}\cos(\eta)\right]^T \tag{5.2}$$

and

$$\boldsymbol{\alpha}_c = \dot{\boldsymbol{\omega}}_c = \left[\ddot{\eta}, \dot{\phi}\dot{\eta}\cos(\eta) + \ddot{\phi}\sin(\eta), \ddot{\phi}\cos(\eta) - \dot{\phi}\dot{\eta}\sin(\eta)\right]^T, \tag{5.3}$$

respectively. The AOA can be simply obtained by $\left|90° - \eta\right|$. The inertial and aerodynamic load can be fully determined if Eqs. 5.2 and 5.3 are known. For a given prescribed sweeping motion $\phi(t)$, the tuned elastic hinge stiffness fully determines the (passive) pitching motion and, therefore, the aerodynamic load generation (e.g., lift force). Consequently, changing the elastic hinge stiffness in an active manner would lead to changes in the aerodynamic load generation and, hence, to a way to control FWMAV flight.

5.3. ELECTROSTATICALLY CONTROLLED HINGE THEORY

This section discusses a model to electrostatically control the dynamic properties of the active hinge. First, it presents the proposed hinge design followed by a description of the voltage-induced normal stress between the stacked layers. Subsequently, it describes the voltage-dependent behavior during the flapping motion (i.e., whether the layers slip or stick). After that, the voltage-dependent properties of the active hinge (i.e., its rotational stiffness and power dissipation) during the flapping motion are presented.

5.3.1. PROPOSED ELASTIC HINGE DESIGN

The elastic hinge in the wing design of Fig. 5.2 is replaced by an active hinge for which an enlarged side-view is shown in Fig. 5.4 (a). The hinge is symmetric in thickness direction. The hinge has length L and width b. It consists of a conducting core which is covered on both sides by dielectric layers and two conducting facings. The core connects the wing holder to the wing while the two facings are attached to the wing holder only. The two facings can slide with respect to the core. The thickness of the core, the dielectric layers, and the facings are denoted by t_c, t_d, and t_f, respectively (see Fig. 5.4 (b)). Two clamps are attached to the wing to prevent the layers from separating during the pitching motion. Hence, all layers will always contribute to the resulting bending stiffness. The facings are assumed to slip freely with respect to the clamps.

5.3.2. VOLTAGE-INDUCED STRESSES BETWEEN STACKED LAYERS

By applying a voltage V to the conducting facings of the active hinge while connecting the conducting core to ground, an electric field is created over the dielectric layers, see Fig. 5.5 (a). This electric field induces a normal stress at the interface between the facings and the dielectric layers, see Fig. 5.5 (b), which is given by (Bergamini *et al.*, 2006)

$$\sigma_N(V) = \frac{1}{2}\frac{\varepsilon_0 \varepsilon_r V^2}{t_d^2}, \tag{5.4}$$

where ε_0 represents the vacuum permittivity and ε_r is the material-dependent relative permittivity. The normal stress depends quadratically on the applied voltage V and
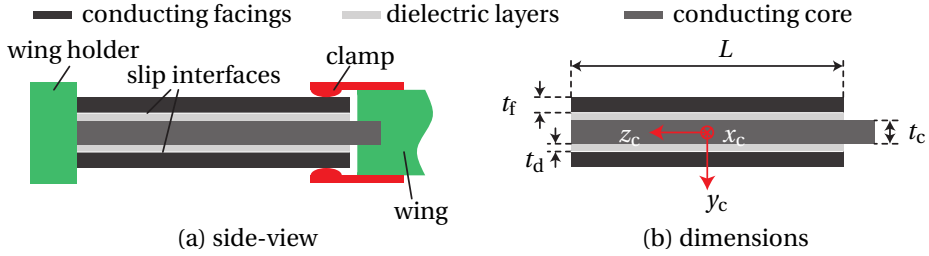
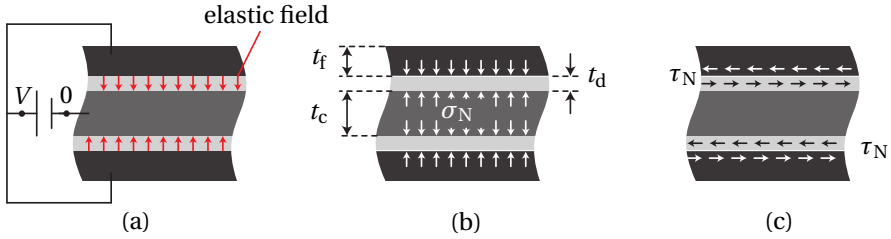**Figure 5.4:** Symmetric active hinge design.

Figure 5.5: Zoom-in of the active hinge during electrostatic loading. (a) Electric field over dielectric layer due to applied voltage V. (b) Normal stress σ_N due to the electrostatic loading. (c) Shear stress distribution τ_N at the interface.

inversely quadratic on the gap between the conducting layers (i.e., the dielectric layer thickness t_d). The normal stress introduces friction between the stacked layers to resist slip during deflection. The shear stress that can be transferred from one layer to the other due to this friction, see Fig. 5.5 (c), is given by

$$\tau_N(V) = \mu \sigma_N(V), \tag{5.5}$$

where μ represents the material-dependent friction coefficient at the interface which depends on whether there is relative displacement at the interface (i.e., dynamic friction) or not (i.e., static friction). The sticked layers start to slip with respect to each other if the shear stress at the interface due to deflection becomes higher than the friction-induced shear stress of Eq. 5.5. Thus, Eq. 5.5 determines the threshold value at which the transition from stick to slip at the interface takes place. This work assumes the static and dynamic friction coefficient to be equal to improve the understanding of the active hinge behavior.

5.3.3. BEHAVIOR OF THE ACTIVE HINGE DURING LARGE DEFLECTIONS

This section describes the stick-slip phenomena of the active hinge as a function of the applied voltage V during large deflections to understand its rather complex behavior (i.e., the active hinge is not a simple spring anymore). The hinge deflects according to the wing pitching motion $\eta(t)$ and it is assumed that the stacked layers slip over the entire interface without restriction for $V = 0$. For $V > 0$, the voltage-induced normal stress tries to prevent slip by introducing friction. The required friction to prevent slip increases if

the hinge deflection increases. The required voltage to stick the layers together up to the maximal deflection is denoted by V_{st} (i.e., the layers do, in that case, not slip throughout the entire pitching motion). In the following, two phases are distinguished: the layers either completely slip or completely stick over the entire interface.

Figure 5.6 shows conceptual steady-state stick-slip behavior of the hinge layers during a pitching motion $\eta(t)$ for a voltage $0 < V < V_{st}$. The essential step in understanding the hinge behavior is the investigation of the interface shear stress τ_{in} during the pitching motion. It is assumed that, at the start of the graph, η increases (i.e., deflection increases) and the layers slip. During slip, the interface shear stress τ_{in} is constant and equal to the friction-induced threshold shear stress (i.e., τ_N). The constant interface shear stress results in a constant shear deformation of the layers, see State 1 in Fig. 5.7. The layers continue to slip until the maximum pitching angle (i.e., maximum hinge deflection) is reached, resulting in a hinge layer off-set, see Configuration 1 in Fig. 5.6.

There is no relative motion at the interface at the maximal pitching angle, which initiates stick between the layers. At the start of the reversal motion (i.e., η decreases), the layers remain sticking since the interface shear stress τ_{in} becomes lower than the friction-induced threshold shear stress τ_N. The interface shear stress decreases during this reversal until $\tau_{in} = -\tau_N$ (i.e., until the maximum friction-induced shear stress τ_N is reached again). At that point, the layers have not slipped yet as illustrated by Configurations 1 & 2 in Fig. 5.6 where the layer off-set did not change. The shear deformation of the layers changes according to the changing interface shear stress as represented by States 1 - 5 in Fig. 5.7. During the remainder of the reversal motion (i.e, until the maximum negative η), the layers slip and result in a layer off-set opposite to the one at the start of the pitching reversal, see Configuration 1 to 3 in Fig. 5.6. During this slip, the interface shear stress and, hence, the shear deformation is constant, see States 5 - 7 in Fig. 5.7.

Thereafter, a similar but opposite cycle starts followed by identical consecutive cycles. If the layers stick, the off-set between the layers remains the same (see, for example, Configuration 3 & 4 in Fig. 5.6) while the interface shear stress and, consequently, the layer shear deformation changes (e.g., States 7 - 10 in Fig. 5.7). On the other hand, if the layers slip, the off-set changes (e.g., from Configuration 4 to 5 in Fig. 5.6) while the interface shear stress and, consequently, the layer shear deformation, is constant. The complexity that might be caused by the marginal off-set between stacked layers (e.g., buckling), is neglected.

During sticking, the interface shear stress τ_{in} changes with an amplitude of $\Delta\tau_{in} = 2\tau_N$ before the layers start to slip again as shown by the difference between the horizontal dashed threshold lines in Fig. 5.7. The pitch-duration for which the layers stick is denoted by $\Delta\eta^*$, see Fig. 5.6. To determine $\Delta\eta^*$, the relation between the change of the pitching angle η (i.e., $\Delta\eta$) and the known change of the interface shear stress (i.e., $\Delta\tau_{in}$) is used. This relation is clarified in the following based on the flowchart of Fig. 5.8 and the sketches of Fig. 5.9.

Firstly, the change of the pitching angle $\Delta\eta$ is discussed. During flapping flight, the wing loading can be captured by an external load P which is assumed to remain perpendicular to the wing surface (see Fig. 5.9 (a)) for all angles of attack. This assumption is justified since the strength of the bound circulation at a post-stall angle of attack, that
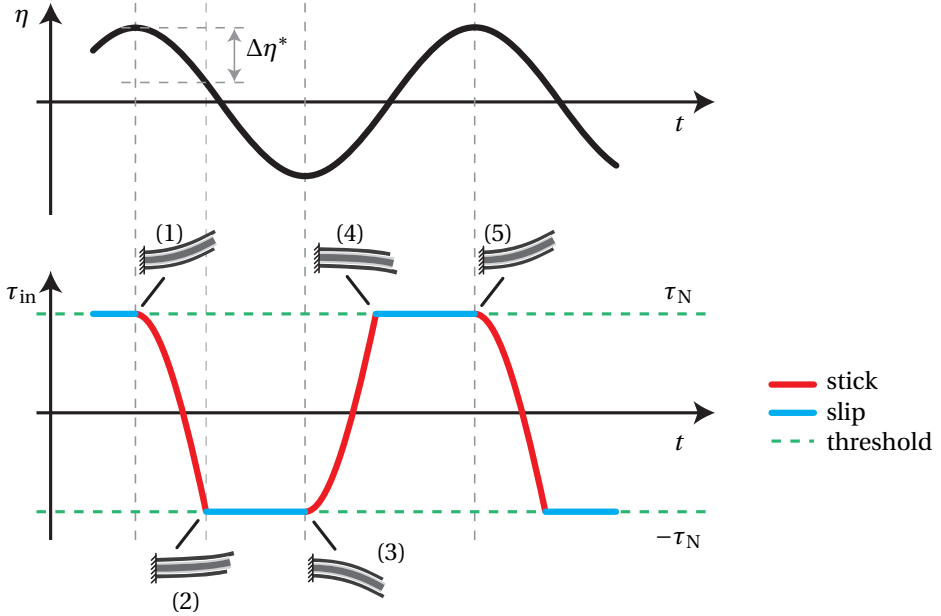
Figure 5.6: Conceptual steady-state stick-slip behavior of the voltage-controlled active hinge during the pitching motion $\eta(t)$ for a voltage $0 < V < V_{st}$ with the corresponding interface shear stress τ_{in}. Additionally, it shows the pitch-duration $\Delta \eta^*$ for which the layers stick together. The dotted green line represents the friction-induced threshold shear stress τ_N. Characteristic layer off-set configurations are indicated by Configurations 1 - 5.

results in a net force perpendicular to the incoming flow, is negligible as compared to the vorticity-induced circulation that results in the load perpendicular to the wing surface (Ford & Babinsky, 2014). Although the location of the center of load (COL) varies slightly during a flapping cycle we assume it to be constant at a distance $l_{COL} = 0.5L + 0.5c$ from the wing holder (Zhao *et al.*, 2010), where L is the hinge length and c is the chord length (see Fig. 5.2). The load P causes the wing to pitch through an angle η. The change of the pitching angle $\Delta \eta$ due to a change of the external load ΔP is, using a linear spring model, given by

$$\Delta \eta = \frac{\Delta P l_{COL}}{k_\eta}, \tag{5.6}$$

where k_η represents the effective rotational stiffness (see Eq. 5.1).

Secondly, the change of the interface shear stress $\Delta \tau_{in}$ is discussed. The external load P results in a moment M and a shear force Q (i.e., $Q = P$) at the cross-section of the sticked layers (see Fig. 5.9 (b)). Q is assumed to be constant along the length of the hinge L. From ordinary sandwich beam theory, the change of the shear stress $\Delta \tau_{in}$ at a depth $y_i = 0.5t_c + t_d$ (i.e., at the interface) due to a change of the shear force ΔQ at the
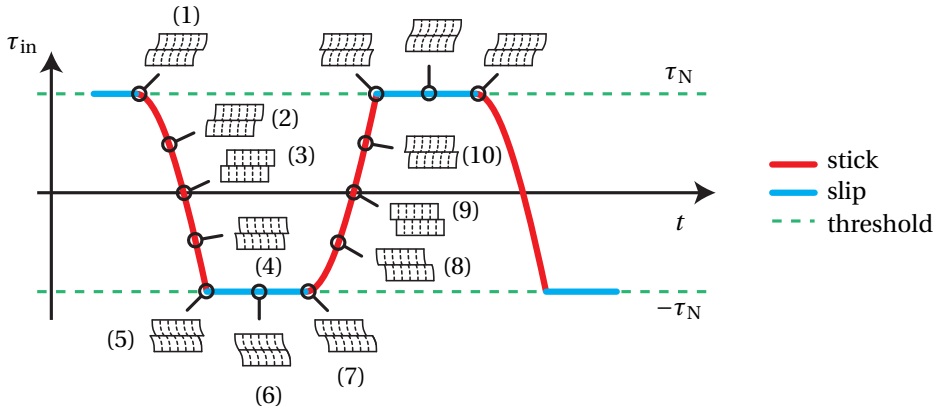
Figure 5.7: Sketches of the shear deformation of two layers of the voltage-controlled active hinge during the pitching motion $\eta(t)$ for a voltage $0 < V < V_{st}$ at different interface shear stress values τ_{in}. States 1 - 10 represent characteristic shear deformation sketches.

Figure 5.8: Graphical interpretation of the relation between the change of the pitching angle $\Delta\eta$ and the interface shear stress $\Delta\tau_{in}$. ΔP and ΔQ represent the change of the external load on the wing and the shear force at the cross-section, respectively.

cross-section, is given by Allen (1969)

$$\Delta\tau_{in}\left(y_i\right) = \frac{\Delta Q}{Db} \sum (SE), \tag{5.7}$$

where D represents the flexural rigidity of the entire cross section, b gives the width of the active hinge at the interface, and $\sum (SE)$ represents the sum of the products of the first moment of area S and the Young's modulus E of all parts of the cross section for which $y_c > y_i$. Due to symmetry in the thickness direction, the shear stress at the other interface (i.e., $y_c = -y_i$) is identical.

Finally, given the known voltage-induced $\Delta\tau_{in}$, the change of the shear force ΔQ can be obtained from Eq. 5.7. Since $\Delta P = \Delta Q$, the change of the pitching angle $\Delta\eta$ can be determined from Eq. 5.6. This change of the pitching angle gives, consequently, the pitch-duration $\Delta\eta^*$ for which the layers stick.

In conclusion, stick and slip alternate during the pitching motion. The properties of the hinge depend on whether the layers stick or slip as discussed in the next section. Hence, it is important to know the pitch-duration $\Delta\eta^*$ for which the layers stick. This pitch-duration is, in this work, directly related to the change of the friction-induced shear stress $\Delta\tau_{in}$ using the external load P. Hence, this enables the determination of the
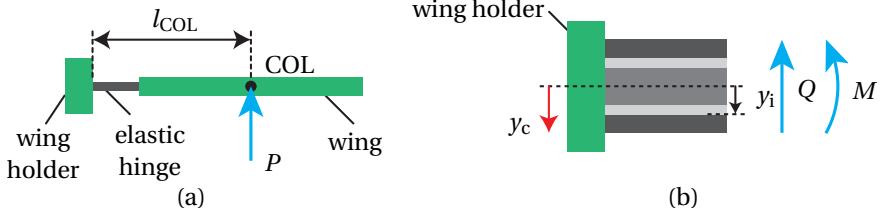
Figure 5.9: Side-view sketches of the wing design to determine the interface shear stress, τ_{in}, and pitch angle, η, due to the external load P. (a) center of load (COL) with the external load P. (b) zoom-in of the active hinge with moment M and shear force Q at the cross-section due to load P.

stick-slip behavior of the active hinge during large deflections.

5.3.4. VOLTAGE-DEPENDENT HINGE PROPERTIES

The property changes of the active hinge as a function of the applied voltage are twofold: (1) rotational stiffness changes, and (2) energy dissipation changes due to friction at the interfaces. Both influence the passive pitching response.

Depending on whether the layers stick or slip, the tangent rotational stiffness is denoted by

- k_η^{st} if the layers stick. In this case, the active hinge consists, basically, of one single bending element, and

- k_η^{sl} if the layers slip. In this case, the active hinge consists, basically, of three individually bending layers.

The tangent rotational stiffness of the sticking layers is significantly higher compared to the slipping layers case. For example, for a beam consisting of n stacked layers with width b and thickness t, the ratio between the second moments of area for sticking and slipping cases is n^2 (i.e., $I_{\text{stick}}/I_{\text{slip}} = (n^3 bh^3/12)/(nbh^3/12)$). Subsequently, the tangent rotational stiffness is n^2 times higher if the layers stick.

For $0 < V < V_{\text{st}}$, the layers sequentially stick and slip during the pitching motion. Whenever the layers slip, energy is dissipated due to friction which leads to mechanical damping. The resulting dissipated power due to friction between the layers (i.e., there are two sliding interfaces in the current hinge design) can be given by

$$P^{\text{fr}}(V, t) = \mu_{\text{d}} \sigma_{\text{N}}(V) b \int_0^L (\nu_1(\xi, t) + \nu_2(\xi, t)) \, d\xi, \tag{5.8}$$

where ξ represents a coordinate along the active hinge and $\nu_1(\xi, t)$ and $\nu_2(\xi, t)$ represent the relative velocity between the slipping layers at the upper interface (i.e., at $y_c = -y_i$, see Fig. 5.9 (b)) and lower interface (i.e., at $y_c = y_i$), respectively. The relative velocity along the hinge is determined by the pitching motion $\eta(t)$ and the thickness of the layers. It is assumed that the relative velocity at the interface increases linearly from zero at the wing holder (i.e., at $\xi = 0$) to its maximal value at the end of the hinge (i.e., at $\xi = L$)

although the velocity distribution might be more complex in reality. During slip, the counteracting moment due to the friction can, subsequently, be obtained by

$$M_{x_c}^{fr} = \begin{cases} 0 & \text{for} \quad V = 0, \\ P^{fr}(V, t)/\dot{\eta} & \text{for} \quad V \neq 0. \end{cases} \tag{5.9}$$

Equation 5.9 explicitly assumes that the dissipated power is equal to zero for $V = 0$ although this assumption oversimplifies the occurring slip behavior due to the inevitable normal stress between slipping layers which are jointly bending. This description allows, despite the limitations, to study the influence of an electrostatically controlled active hinge on the passive pitching motion of a flapping wing.

5.4. Equation of motion of passive pitching motion

Since the sweeping motion $\phi(t)$ is prescribed, the rigid wing model involves only one degree of freedom, the pitching angle η. The equation of motion that governs η can be obtained by applying Euler's second law of motion. That is,

$$M_{x_c}^{applied} + M_{x_c}^{iner} = 0, \tag{5.10}$$

where the inertial torque, $M_{x_c}^{iner}$, in the co-rotating frame is given by

$$M_{x_c}^{iner} = I_{x_c x_c} \left[\frac{1}{2} \sin(2\eta)\dot{\phi}^2 - \ddot{\eta} \right] - I_{x_c z_c} \ddot{\phi} \cos(\eta), \tag{5.11}$$

where $I_{x_c x_c}$ and $I_{x_c z_c}$ are moment of inertia terms. The applied torque, $M_{x_c}^{applied}$, acting around the pitching axis consists of three components: (1) the elastic torque from the active hinge, $M_{x_c}^{elas}$, (2) the voltage-dependent torque due to the friction between the layers, $M_{x_c}^{fr}$, as calculated by Eq. 5.9, and (3) the aerodynamic torque $M_{x_c}^{aero}$.

A quasi-steady aerodynamic model is used to calculate the transient aerodynamic loads. This chapter only shows the terms relevant for this work without going into much detail on the specific terms. For more details the reader is referred to Wang *et al.* (2016). The aerodynamic model assumes the resultant aerodynamic load acting on the wing to be always perpendicular to the chord over the entire stroke (i.e., in y_c-direction). For thin plates, this assumption is justified due to a negligible leading-edge suction load and wing surface viscous drag compared to the dominant pressure load. The loads are decomposed into four components which originate from different sources: (1) from the wing translational velocity, leading to $F_{y_c}^{trans}$ and $M_{y_c}^{trans}$ (Sane & Dickinson, 2002), (2) from the coupling effect between wing translational and rotational effect, leading to $F_{y_c}^{coupl}$ and $M_{y_c}^{coupl}$, (3) from the pure rotational velocity, leading to $F_{y_c}^{rot}$ and $M_{y_c}^{rot}$, and (4) from the added mass effect, leading to $F_{y_c}^{am}$ and $M_{y_c}^{am}$ (Newman, 1977). The resultant aerodynamic

loads can be calculated by

$$
F_{y_c}^{\text{aero}} = \underbrace{-\text{sgn}(\omega_{z_c})\frac{1}{6}\rho_f c R^3 c_{F_{y_c}^{\text{trans}}}(\omega_{y_c}^2 + \omega_{z_c}^2)}_{F_{y_c}^{\text{trans}}} + \underbrace{\frac{3}{8}\pi\rho_f c^2 R^2 \omega_{x_c}\omega_{y_c}}_{F_{y_c}^{\text{coupl}}}
$$
$$
\underbrace{-\frac{1}{6}\rho_f c^3 R C^{\text{rot}}\omega_{x_c}|\omega_{x_c}|}_{F_{y_c}^{\text{rot}}} + \underbrace{\frac{\pi}{8}\rho_f c^2 R \left[-R(\alpha_{z_c} + \omega_{x_c}\omega_{yc}) - c\alpha_{x_c}\right]}_{F_{y_c}^{\text{am}}} \tag{5.12}
$$

and

$$
M_{y_c}^{\text{aero}} = \underbrace{-\text{sgn}(\omega_{z_c})\frac{1}{6}\rho_f c^2 R^3 c_{F_{y_c}^{\text{trans}}}\hat{z}_{cp}^{\text{trans}}(\omega_{y_c}^2 + \omega_{z_c}^2)}_{M_{y_c}^{\text{trans}}} + \underbrace{\frac{3}{32}\pi\rho_f c^3 R^2 \omega_{x_c}\omega_{y_c}}_{M_{y_c}^{\text{coupl}}}
$$
$$
\underbrace{-\frac{1}{8}\rho_f c^4 R C^{\text{rot}}\omega_{x_c}|\omega_{x_c}|}_{M_{y_c}^{\text{rot}}} + \underbrace{\frac{\pi}{16}\rho_f c^3 R \left[-R(\alpha_{z_c} + \omega_{x_c}\omega_{yc}) - \frac{9}{8}c\alpha_{x_c}\right]}_{M_{y_c}^{\text{am}}} \tag{5.13}
$$

respectively, where ρ_f is the density of the fluid, $\hat{z}_{cp}^{\text{trans}}$ is the position of the center of pressure due to the translational force which is calculated using an empirical formula (i.e., $\hat{z}_{cp}^{\text{trans}} = 0.261\,(\text{AOA}) + 0.05$), and C^{rot} is the drag coefficient for a plate revolving at an AOA of $90°$. An analytical model proposed by Taha *et al.* (2014) is used to calculate the lift coefficient $c_{F_{y_c}^{\text{trans}}}$ due to the wing translational velocity. This analytical formula provides a good prediction of the lift coefficients of translational flapping wings with different aspect ratios according to the comparison with experimental data from bumble bees, fruit flies and hawk moths.

Eventually, the voltage-dependent equation of motion of the wing passive pitching can be expressed as

$$
I_{x_c x_c}\ddot{\eta} + k_\eta \eta = M_{y_c}^{\text{aero}} + f(\eta, \dot{\eta}) + M_{x_c}^{\text{fr}}\left(\dot{\eta}, V\right), \tag{5.14}
$$

where the inertial drive torque $f(\eta, \dot{\eta})$ is given by

$$
f(\eta, \dot{\eta}) = \frac{1}{2}I_{x_c x_c}\dot{\phi}^2 \sin(2\eta) - I_{x_c z_c}\ddot{\phi}\cos(\eta). \tag{5.15}
$$

Finally, Eq. 5.13 will be used to determine the average lift generated by the flapping wing with the actively controlled elastic hinge. It should be mentioned that the introduced quasi-steady model cannot capture some unsteady effects (e.g., wake capture effect and Wagner effect). Rather good agreements can, however, be found between the results from the quasi-steady model and experiments (Wang *et al.*, 2016) since the most important unsteady effect (i.e., the prolonged attached of the leading edge vortex) is captured. As such, the model is adequate for this work.

5.5. Experimental analysis
To validate the presented approach on changing the dynamic properties of wing hinges, experiments are done. First, the manufactured wing equipped with an active hinge is
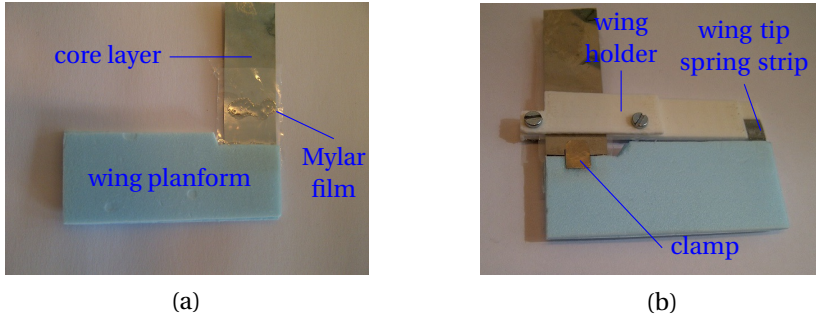
Figure 5.10: Wing design consisting of a wing planform, a active hinge, and a wing holder. (a) Planform with core layer covered by Mylar film. (b) Realized wing design.

discussed together with the experimental setup. After that, the change of the passive pitching motion due to different applied voltages is shown. Finally, the experimentally and analytically obtained results are compared.

5.5.1. WING REALIZATION

The wing design consists of three parts: (1) the wing planform, (2) the active hinge at the wing root, and (3) the wing holder (see Fig. 5.10). The first part, the wing planform, is composed by gluing two rectangular, 1 mm thick sheets of blue foam (i.e., Expanded PolyStyrene (EPS) with Young's modulus $E_{\mathrm{EPS}} = 3$ GPa) on top of each other. The wingspan $R = 50$ mm and its chord length $c = 20$ mm. The core layer of the active hinge is clamped between these two sheets. The second part, the active hinge, consists of a conducting core which is on both sides covered by, consecutively, a dielectric layer and a conducting facing. For all conducting layers, spring steel strips are used (i.e., Young's modulus $E_s = 210$ GPa). These spring steel strips are tough and allow for a large number of cyclic, large deflections. The strips have a width b of 12.7 mm and the thickness of the core and the facings is 20 μm and 5 μm, respectively. For the dielectric layers two different approaches can be followed: (1) spin coat a thin polymeric film onto the conducting layer(s) (e.g., the photo-resist SU-8), or (2) use thin sheets of dielectric polymer film (e.g., Mylar). In this work, 5 μm thick Mylar films are tightly attached to the core conducting layer by gluing its two edges to the spring steel while squeezing the air layer out, see Fig. 5.10 (a). For the Mylar, the Young's modulus $E_{\mathrm{d}} = 4.25$ GPa, the dielectric constant $\varepsilon_{\mathrm{r}} = 3.25$, the static and dynamic friction coefficients with respect to steel are assumed to be equal, that is, $\mu_s = \mu_{\mathrm{d}} = 0.2$ [1], and the dielectric strength is $V_{\mathrm{d}} = 500$ V/μm (Free Flight Supplies, 2015, Toolbox, 2015). The total length of the active hinge $L = 5$ mm. To prevent the layer from separating during the pitching motion, clamps are added on both sides. The bending stiffness EI of the blue EPS plate is about 1000× higher in chordwise direction compared to that of the hinge. Therefore, the wing planform can be regarded

---

[1]Since no appropriate information was found about the friction coefficient between Mylar (PET, Polyethylene terephthalate) and spring steel, the friction coefficient between the similar material PE (Polyethylene) and steel was used instead.
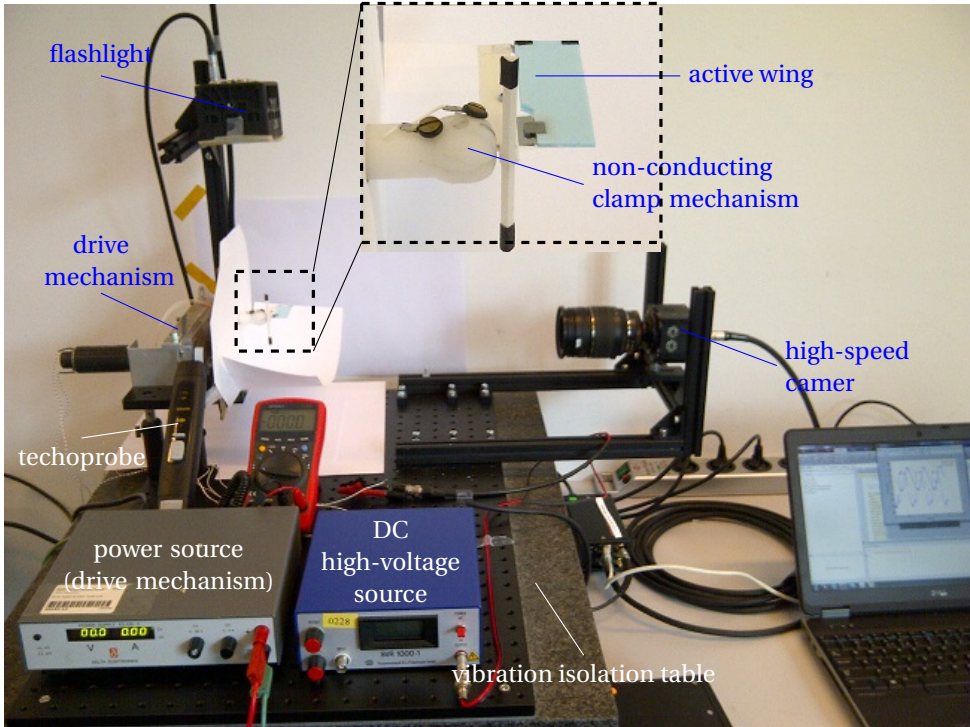
Figure 5.11: Experimental setup indicating the key components.

as a rigid plate.

The third part, the wing holder, is made from 3D-printed plastic. The wing holder is extended over the entire wing span to constrain the movement of the wing tip via a strip of spring steel with a relatively high bending compliance. This constraint prevents warping of the active hinge during large deflections which would lead to undesired large deflections in spanwise direction. The resulting wing design is shown in Fig. 5.10(b).

The total mass of the realized wing (excluding the wing holder) is around 300 mg which is relatively high compared to wings found in nature with similar dimensions (e.g., 50 mg) due to glue and the additional clamps. With the currently used layer thicknesses, the ratio between the bending stiffness of the sticked layers, k_η^{st}, and the slipping layers, k_η^{sl}, is $(t_c + 2t_d + 2t_f)^3 / (t_c^3 + 2t_f^3) = 2.34$.

5.5.2. EXPERIMENTAL SETUP

Figure 5.11 shows a picture of the experimental setup as positioned on a vibration-isolating table. The key components of this setup are: (1) the active wing, (2) a non-conducting clamping mechanism to apply the voltage to the facings and to ground the core layer, (3) a DC high-voltage source to apply the voltage to the active hinge, (4) a driving mechanism to enforce a harmonic sweeping motion $\phi(t)$ to the wing, (5) a tachoprobe to measure the driving frequency, and (6) a high-speed camera with a flashlight to capture

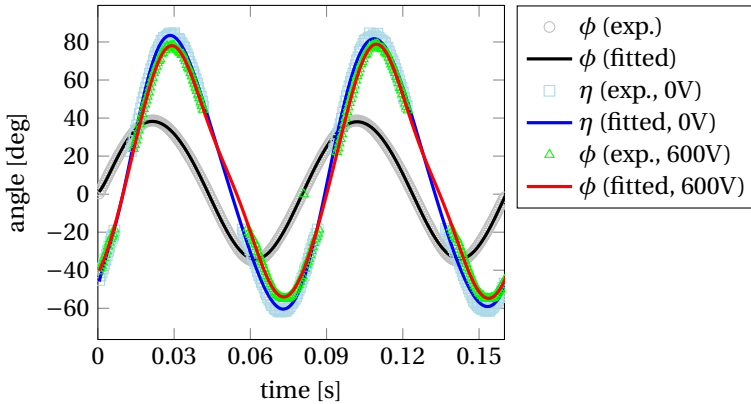**Figure 5.12:** Flapping kinematics of a passive pitching wing design for which the pitching amplitude decreases if the applied voltage to the active hinge increases.

the flapping motion.

To capture the pitching motion, two black markers are glued onto the wing tip of the wing design in chord-wise direction. The distance on the captured image between these markers when the wing planform is perpendicular to the optical axis of the camera, is taken as the reference length and denoted by d_b. The high-speed camera (2000fps) captures images and, thus, the distance between the black markers during the flapping motion. By relating this distance to the reference length d_b, the pitching angle $\eta(t)$ can be calculated.

5.5.3. EXPERIMENTAL RESULTS

This section shows experimental results of one specific wing design. Although similar trends were found for other wing designs, this design shows the trend most clearly over a large range of applied voltages. Due to wing fabrication difficulties it was hard to compare different designs over a large range of applied voltages. These difficulties were, among others, handling the extremely thin spring steel and Mylar sheets (i.e., $5\,\mu$m) and preventing a remaining air layer between the stacked layers. This air layer has a negative influence on the voltage-induced normal stress (see Eq. 5.4). Hence, the number of well succeeded wing designs was limited.

The driving frequency was constant for all experiments and restricted to 12.5 Hz to prevent excessive pitching amplitudes (i.e., $\eta(t) > 90°$). Figure 5.12 shows the resulting flapping kinematics: the sweeping motion $\phi(t)$ and the passive pitching motion $\eta(t)$. The passive pitching motion lags behind the sweeping motion by about 30°. The amplitude of the sweeping motion is 37.5°. The maximum passive pitching angle decreases if the applied voltage to the active hinge increases (i.e., the maximum pitching angle decreases from about 84° for 0 V to about 78° for 600 V) and the phase lag becomes slightly bigger (i.e., a few degrees). The asymmetry of the passive pitching motion is caused by inaccuracies of the realized flapping wing design. The small irregularities or disappearance of measurement points for the pitching motion is caused by the difficulties in tracking the markers on the flapping wing, especially around $\eta(t) = 0°$.
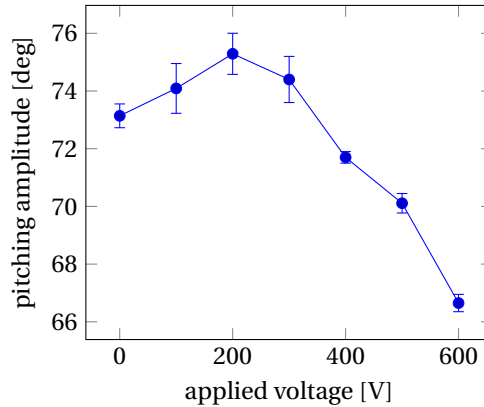
Figure 5.13: Average pitching amplitude as a function of the applied voltage V. The error bars indicate the measurement uncertainty as determined by the non-smoothness of the measured pitching motion $\eta(t)$.

Figure 5.13 shows the change of the average pitching amplitude (using both the maximum and minimum pitching angle) as a function of the applied voltage to the active hinge. To get these results, the flapping frequency was fixed to 12.5 Hz and the applied voltage was increased in steps of 100 V to the maximum of 600 V. For each measurement point, a wait of a couple of seconds was introduced to be assured of steady-state motion before taking images. For some images, the exact location of the black markers was hard to identify. This resulted in a non-smooth pitching angle $\eta(t)$ as shown by some outliers in Fig. 5.12. This, consequently, complicates the determination of the maximum pitching angle. The error bars indicate the uncertainty of the maximum pitching angle as determined by the spread in the measurements. Figure 5.13 also shows an increase of the average passive pitching amplitude up to 200 V followed by a monotonic decrease of this amplitude for higher voltages. A possible explanation for this initial amplitude increase is the presence of the clamps on the wings to keep the layers from separating. The friction between these clamps and the outer facings decreases if the voltage-induced sticking of the stacked layers increases. The reduction of friction reduces the energy loss and, hence, increases the average pitching amplitude.

The targeted gap between the core conducting layer and the outer facings was 5 μm as determined by the thickness of the Mylar sheet. Since the electric strength of Mylar is 500 V/μm, the maximum possible applied voltage to the active hinge is, theoretically, restricted to 2500 V. Figures 5.12 and 5.13 show only results up to 600 V since the hinge failed for higher voltages. This could have several reasons, for example: (1) due to Mylar sheet irregularities (e.g., a small scratch) the practical dielectric strength is lower than the theoretical value, or (2) due to the presence of the very thin air gap between the conducting layers and the dielectric sheet. If the breakthrough voltage of the air gap is reached, a current is going to flow which might locally burn the dielectric Mylar layer.
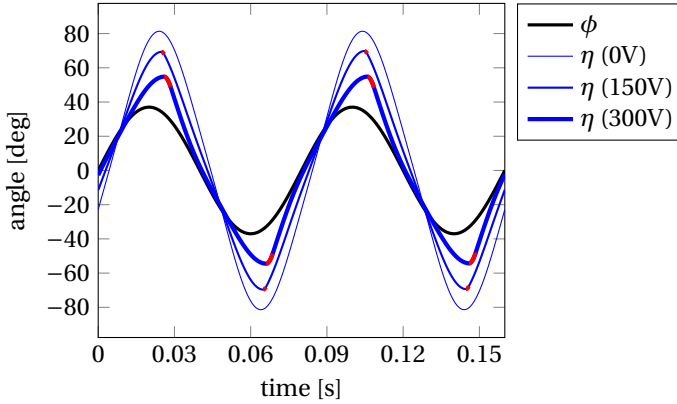
Figure 5.14: Numerical results of the flapping kinematics for different applied voltages to the active hinge. Segments in red show the pitch-duration $\Delta\eta^*$ (i.e., just after the maximum pitching angle) for which the layers stick.

5.6. NUMERICAL ANALYSIS AND COMPARISON TO EXPERIMENTAL RESULTS

The numerical analysis to determine the passive pitching motion is complicated by the abrupt jump in the hinge stiffness if the layers of the active hinge change from stick to slip, or visa versa. To solve this problem the jump of the hinge stiffness is smoothed by a C^∞ function, and the ode15s solver from MATLAB® is used to solve this stiff problem. Figure 5.14 shows the sweeping motion $\phi(t)$ and numerical steady-state passive pitching $\eta(t)$ for different applied voltages V to the active hinge. The figure clearly shows the decrease in the pitching amplitude for an increase of the voltage. The passive pitching motion without voltage (i.e., 0 V) lags behind the sweeping motion by about 30°, which is comparable to the experimental results. The phase lag increases slightly if the voltage increases. Additionally, the figure indicates the locations at which the layers stick (i.e., just after the maximum pitching angle). The pitch-duration $\Delta\eta^*$ for which the layers stick increases if the applied voltage increases although it remains relatively short with respect to the entire flapping cycle.

Figure 5.15 (a) shows the numerical change of the average pitching amplitudes as a function of the applied voltages. The average pitching angle decreases monotonically, almost linearly, if the voltage increases. The cycle-average lift force decreases accordingly, see Fig. 5.15 (b). The average lift force decreases by about 31% if the voltage is increased from 0 V to 250 V, which is sufficient in controlling lightweight FWMAV designs. The maximum applied voltage is set to 250 V. For voltages higher than 250 V, the passive pitching motion $\eta(t)$, as shown in Fig. 5.14, starts to deviate significantly from being harmonic. Additionally, the convergence becomes poor such that a steady-state solution can not be found.

The numerical passive pitching amplitude change due to the applied voltage (i.e., Figs. 5.14 and 5.15 (a)) is more significant compared to the experimental results of Figs. 5.12 and 5.13 although the trend is similar (i.e., decreasing amplitude and increasing
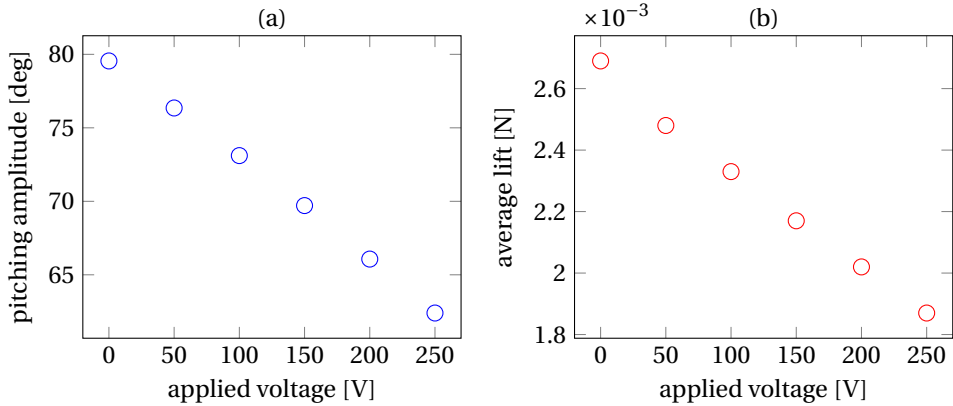
Figure 5.15: Results of analytical analysis as a function of the applied voltages. (a) Analytical average passive pitching amplitudes as a function of the applied voltages. (b) Analytical average lift force as a function of the applied voltages.

phase lag when the applied voltage increases). The discrepancy can be explained by: (1) the simplifying assumptions in the theoretical model, (2) the difficulties in the manufacturing process, and (3) the presence of additional air between the conducting layers and the Mylar.

5.7. CONCLUSIONS

This chapter presents a method to actively control the passive pitching motion of a flapping wing using electrostatic sticking of stacked layers. These stacked layers constitute the elastic hinge at the wing root in a FWMAV design. Actively modifying the structural properties of that hinge (e.g., damping and stiffness) results in significant changes of the wing' passive pitching motion and, hence, of its lift production. The hinge in this work consists of three conducting spring steel layers which are separated from each other by dielectric Mylar films.

During the pitching motion, the layers, consecutively, stick and slip with respect to each other. The layers stick due to the voltage-induced normal stress between the layers. Whenever the layers stick, the bending stiffness of the hinge is significantly higher compared to the case when the layers slip (i.e., 2.34 × for our hinge). If the layers slip, power is dissipated due to friction which is induced by the normal stress between the layers. This friction results in an additional moment that dampens the passive pitching motion.

Numerical simulations show significant changes of the pitching amplitude if the applied voltage to the active hinge increases. The pitch-duration for which the layers stick increases with the applied voltage, although it remains relatively short compared to the duration for which the layers slip. The resulting average lift force changes corresponding to the different applied voltages are sufficient for control purposes of lightweight FWMAV designs. The theoretical model gives, despite the introduced limitations, a clear insight into the voltage-controlled stick-slip behavior of the active hinge during large deflections.

Experiments are conducted to study the practical applicability of this active elastic hinge for small-scale and lightweight FWMAV applications. To obtain experimental results, several fabrication difficulties have been tackled, for example, the handling of the very thin Mylar films (i.e., $5\,\mu$m). The experimental results show, although suppressed, the same trends compared to the numerical simulations. The results are less significant, mainly due to: (1) the presence of an air layer between the conducting layers and the dielectric layers, (2) the presence of Mylar film irregularities. Despite of these shortcomings, the results clearly show a decrease of the pitching amplitude as a function of the applied voltage. Hence, it shows the potential of this method to control FWMAVs.

In future work, the numerical model might be improved to model the stick-slip behavior of the active hinge more accurately (e.g., the friction between the layers in the absence of a control voltage). Additionally, long lasting experiments need to be conducted to study the influence of wear due to friction between the Mylar and the conducting sheets. Alternatively, it is interesting to change the applied voltage during a flapping cycle and study the occurring transient behavior. The fabrication process can be optimized by preparing jigs or well-designed tools.

5

6

RETROSPECTION AND DISCUSSION

Chapters 2 - 5 presented the modeling, design and optimization of flapping wings for efficient hovering flight from different perspectives. In this chapter, these work are retrospected from a bird's-eye view, and the highlights and pitfalls of new designs are discussed. Preliminary investigations on other aspects of flapping wings are also introduced. At the end, the techniques and approaches we have used for wing fabrication and measurement are presented.

6.1. FLAPPING WING MODELING

From Chapter 2 to Chapter 5, flapping wings were modeled from different aspects, including the morphology, kinematics, flexibility, aerodynamics, aeroelasticity and the power consumption. These models played an important role in the design of energy-efficient flapping wings.

6.1.1. MORPHOLOGY

In order to design and optimize flapping wings, the shape and mass distribution were parameterized. From the work of Ellington (1984a), we know that the spanwise area distribution of insect wings can be approximately quantified by a single parameter $\hat{r}_{s_1}$, which represents the spanwise distance between the root and the centroid. Since the wing in the chord wise is divided into two parts by the pitching axis (PA), it is natural to use the location of the PA to describe the chordwise area distribution. We introduced a dimensionless parameter $\hat{d}$ to represent the chord-length-normalized distance between the leading edge (LE) and the PA. We assumed that $\hat{d}$ changes linearly from the wing root to tip. Thus, the chordwise area distribution can be quantified by only two parameters, e.g., the value of $\hat{d}$ at the root and the tip (i.e., $\hat{d}_r$ and $\hat{d}_t$). Therefore, the insect wing shapes used in Chapters 3 - 5 were quantified by only three shape parameters. For those wings with a specific spanwise area distribution (see Chapter 3), the chordwise area distribution based on $\hat{d}_r$ and $\hat{d}_t$ is also used.

The wing mass distribution was modeled in Chapter 3. Span wise, the mass was modeled to decrease exponentially from the root to the tip. The spanwise location of mass center predicted by this model is very close to the measured values on wings of four different insects (errors are less than 6%). Two chordwise mass distribution were used, one assuming a uniform distribution and another assuming a distribution with a kite profile.

It can be seen that both the shape and mass distribution models mimic insect wings. Therefore, we were able to directly study the influence of some morphological features of insect wings on flight performance and to apply the findings in the artificial wing design. Meanwhile, insect wings are the natural references to compare with for the optimal wing designs. Modeling flapping wing in this way might cause fabrication difficulties. Nevertheless, the rapidly developing addictive manufacturing techniques become more and more promising to fabricate cm- and mm-scale flexible wing structures.

6.1.2. KINEMATICS

In this work, we focus on the kinematics with passive pitching motion. In Chapter 2, the quasi-steady aerodynamic model was proposed because existing quasi-steady models either can not be used or have conspicuous shortcomings for studying the passive pitching motion. The proposed model shows that the PA location has a big influence on the passive pitching motion, the aerodynamic force generation and the power consumption. Therefore, Chapter 3 was dedicated to the optimization of the PA location for different wings. In Chapter 4, we investigated the passive pitching behavior while incorporating wing twist. To actively change the passive pitching motion for the flight control of FWMAVs, we introduced an active elastic hinge design in Chapter 5 to allow the tuning of the hinge stiffness.

The passive pitching wing design can dramatically simplify the drive mechanisms of

FWMAVs. Simple drive mechanisms can increase the system reliability and save space and weight for other components of FWMAVs (e.g., battery/fuel, payloads). In contrast, the pitching mechanism used by insect wings is more complicated. First, the motion of insect wings is typically driven and controlled by two types of muscles, namely the power muscles and steering muscles (Walker *et al.*, 2014). A small torque applied by the steering muscles on the PA can significantly change the pitching motion considering the small amplitude of the external torques applied on insect wings (e.g., at the order of 10^{-6} Nm for Drosophila wings (see Fig. 2.18)). The active control of pitching motion can be another explanation for the fast maneuvering of insects in addition to the control of sweeping motion. For example, Muijres *et al.* (2014) experimentally showed the fast evasive maneuvering of flies by subtle changes in wing motion which consists of the slight change of pitching motion. Second, the chordwise bending stiffness of insect wings can be a nonlinear function of the pitching angle. The nonlinearity arises from the asymmetric wing structure between dorsal and ventral sides (Willmott & Ellington, 1997*b*) and the resilins and spikes at venation joints (Donoughe *et al.*, 2011, Appel & Gorb, 2011). These morphological features can inspire engineering realizations for the control of pitching motion for FWMAVs.

6.1.3. FLEXIBILITY

The passive pitching motion and spanwise twist are directly related to the wing flexibility. In Chapters 2, 3 and 4, the wing planform is assumed to be rigid, and the wing stiffness is represented by the concentrated stiffness of the elastic element at the root (e.g., elastic hinge, torsional spring). In Chapter 5, the wing stiffness is represented by a combination of a concentrated stiffness and a distributed stiffness of the wing which is modeled as a plate with a uniform thickness. For the plate wing model, the distributed stiffness is related to both the Young's modulus of the wing material and the wing twist.

Throughout this work, the concentrated stiffness is assumed to be a constant, i.e., the elastic torque is linear to the pitching angle of the wing. In fact, the accuracy of this assumption depends on many factors, including the design of the elastic element, the loads on the wing and the pitching amplitude. There are many ways to realize the elastic element (Howell, 2001, Trease *et al.*, 2005). Among them, the designs using a flexible hinge, which is made of polyimide film (Whitney & Wood, 2010) or spring steel (Bolsman *et al.*, 2009), are the most frequently used for the artificial wing designs. The hinge is essentially a cantilever beam. Therefore, if the hinge is purely loaded by an external torque, its bending stiffness does not change with the increase of the deformation. In this case, the linear elastic assumption for the hinge is justified. However, the force and torque applied on the wing result from the time-varying aerodynamic and inertial loads. This complex loading condition complicates the modeling of the hinge stiffness. Particularly when the wing has a large pitching amplitude, a more accurate model of the hinge bending stiffness might be necessary.

Insect wings normally have a slender root (i.e., a revolute joint) to connect the wing planform with the thorax (a typical example: crane fly wing). Therefore, the pitching motion of these insect wings depends on both the rotational stiffness of the joint and planform. For artificial wings, it is advantageous to use this type of revolute joint for two reasons. First, it helps the integration of the elastic element into the rest of the wing

structure, which can increase the reliability and manufacturability of artificial wings. Second, the ratio of the rotational stiffness to the out-of-plane bending stiffness of the revolute joint can be easily controlled by changing the joint cross-section. Generally, the rotational stiffness is much smaller than the bending stiffness such that the wing can have sufficient pitching but very limited heaving motion. For this purpose, the revolute joint based on a split-tube (Goldfarb & Speich, 1999) is well suited and worth further study.

6.1.4. AERODYNAMICS AND AEROELASTICITY

The aerodynamic and aeroelasticity models are pillars for the wing design and optimization. To ensure the applicability, their accuracy, predictability and computational efficiency need to be guaranteed.

In Chapter 2, we proposed a predictive quasi-steady model to calculate the aerodynamic loads on flapping wings. This model has been used throughout the wing design process. In Chapter 5, a computationally efficient fluid-structure interaction (FSI) model was proposed to study the aeroelasticity of twistable wings. The proposed FSI model uses an analytical twist model and the quasi-steady aerodynamic model to do the structural and aerodynamic analysis, respectively. The wing twist was modeled by just a few degrees of freedom since that the contribution from high-order twist modes is very marginal for a highly damped flapping wing system.

Undoubtedly, the computationally efficient quasi-steady aerodynamic and FSI models are important for the design of artificial flapping wings. However, we need to know the inherent drawbacks of these models arising from the quasi-steady assumption and the blade element method. One of the important aerodynamic characteristics of hovering flight is the unsteadiness. However, it is "averaged" both spatially and temporally by most quasi-steady models. Although these models can provide an acceptable (average) aerodynamic force estimation, they can not reflect some unsteady mechanisms, such as the fast pitching-up rotation effect (Meng & Sun, 2015) and the wing-wake interaction (Lehmann, 2008). In the context of the quasi-steady analysis, one common way to improve quasi-steady models is to introduce empirical corrections. Another one is to include additional terms to model the sources of unsteadiness. For example, the idea of including the pure rotational term and reformulating the coupling term in the quasi-steady model proposed in Chapter 2 is to better represent the unsteady phenomena caused by the pitching rotation. However, the resulting is the overlap between different terms which might cause an overestimation of aerodynamic loads on flapping wings. Although it is still valuable to keep improving existing quasi-steady models, it might be more helpful to use quasi-steady models to guide the preliminary design of artificial flapping wings or study insect wings and then implement experimental approaches to verify and concretize the preliminary findings.

6.1.5. POWER CONSUMPTION

The power consumed by a flapping wing system was calculated from both the perspectives of power output and input. In Chapter 3, we calculated the total power consumption based on three outputs, i.e., the aerodynamic power, inertial power and the elastic power. In contrast, the total power consumption was calculated by multiplying the drive

torque applied on flapping wings with the corresponding wing angular velocity in Chapter 4. Essentially, there is no difference between these two methods. However, they can serve us for different purposes. The method based on the power output can show details of the power consumed by the aerodynamic force, inertial force and elastic force. This information is useful to interpret the power efficiency of specific flapping wing designs. If only the net power consumption is of interest, the method based on the power input might be preferable.

Two extreme cases of the power consumption were studied. For a drive system with the capacity of kinetic energy recovery (KERS), the cycle-averaged elastic and inertia power is zero. Therefore, the total average power consumption is equal to the average aerodynamic power. For a drive system without the capacity of kinetic energy recovery (non-KERS), the wing kinetic energy and the elastic potential energy can be transferred into the work to overcome the drag. However, the extra energy after the transfer will be dissipated as heat. These two extreme cases lead to the minimal and maximal power consumption, respectively. It is difficult to model the exact power consumption of a FWMAV considering the complex energy conversion process as introduced in Chapter 1. However, the optimal wing designs corresponding to these extreme cases can provide the lower and upper bounds of the optimal flapping wing configurations for insects and FWMAVs.

In this work, the term "power consumption" specifically represents the power corresponding to the work done by flapping wings (either positive or negative). It is just a part of the total power that is consumed by the entire insects and FWMAVs. It is complicated to model the total power consumption considering the fact the energy losses due to frictions heavily depend on the design of the drive mechanism. If the energy conversion path is clear, more practical flapping wing designs might can be achieved based on the total power consumption model.

6.2. FLAPPING WING DESIGN AND OPTIMIZATION

6.2.1. DESIGN PARAMETERS

For flapping wings with passive pitching motion, the flight performance is collaboratively determined by the drive kinematics, wing morphology and wing flexibility. Therefore, there are many kinematic and morphological parameters related to the flight performance. Based on the importance comparison of design parameters in response to the lift and power consumption (Wang *et al.*, 2014*a*), design parameters with high importance but not well studied in literature were selected and studied in this work. These parameters include the flapping frequency f, the PA location (represented by $\hat{d}_r$ and $\hat{d}_t$), the hinge stiffness k_η and the Young's modulus E of the wing material.

In Chapter 3, four design parameters, i.e., f, $\hat{d}_r$, $\hat{d}_t$ and k_η, were optimized to search for the optimal PA location for flapping wings to hover more efficiently. Chapter 4 was focused on the study of flapping wing twist. Therefore, three design parameters, i.e., f, k_η and E, were investigated. Chapter 5 was dedicated to the design of the active hinge to tune the hinge stiffness k_η for the control of passive pitching motion.

Many interesting phenomena can be found by changing the values of these parameters. One example is the influence of the flapping frequency on the passive pitching be-

havior. It is obvious that the increase of flapping frequency can effectively increase the lift production when the kinematics are fully prescribed. However, for flapping wings using passive pitching motion, the relation between the flapping frequency and the lift generation as well as the power consumption becomes much more complicated. If we define a quantity r_f to represent the ratio of the drive frequency to the undamped eigen-frequency of the flapping wing system, the behavior of the passive pitching motion (e.g., the pitching amplitude, the phase lag from the sweeping motion, and the deviation of the pitching motion from a harmonic function) will dramatically change with the value of r_f. Taking the passive pitching behavior of a rectangular wing as an example, simulation results show that the pitching motion is quite wavy (a signature of higher order harmonics) at low values of r_f (0.2 ~ 0.5). Then, it becomes less wavy and beneficial for the lift production at medium r_f (0.5 ~ 1). Thereafter, the pitching motion experiences a quick change of the phase difference between the sweeping and pitching motion at $1 < r_f < 1.1$. At higher values of r_f, it alternates between chaotic motions and complex periodic motions. However, the frequency of those periodic motions is just a fraction of the drive frequency. The complex behavior originates from both the nonlinear inertial and aerodynamic loads. This nonlinear behavior was also observed in the experiments we have carried out. Many kinematic and morphological parameters can influence the value of r_f by changing the undamped eigen-frequency of the flapping wing system. For instance, the shift of the PA location can significantly change the passive pitching motion, as shown in Chapter 3. This triggered the optimization of the PA location. Therefore, the nonlinear behavior needs to be kept in mind during the design of flapping wings with passive pitching motion.

Another example is the relation between the parameter similarity and the flapping wing diversity. Taking the group of shape parameters $\hat{d}_r$ and $\hat{d}_t$ as an example, flapping wings can have fairly close power efficiency during hovering flight when $\hat{d}_r$ and $\hat{d}_t$ are selected from the diagonal area in the space expanded by these two parameters (Wang *et al.*, 2014*b*). This might be one of the explanations for the diversity of insect wing shapes, and this also gives flexibility to the shape design for artificial wings. In fact, as shown in Fig. 6 of Chapter 4, the group of stiffness-related parameters k_η and E also implies similar information. These findings are based on the analysis of the lift generation and power consumption for hovering flight. Therefore, it would be interesting to verify the findings for forward flight as well in the future.

6.2.2. NEW DESIGNS

In this work, flapping wings were redesigned from the perspectives of the pitching axis (PA) location, twist and the elastic hinge.

In Chapter 3, we found that wings with the PA located between the leading edge (LE) and the mid-chord line can save up to 33% of power during hovering flight when compared to traditional wings which use the straight LE as the PA. The optimized PA also provides the elastic drive system higher potential to recycle energy during the deceleration phases. This observation is particularly useful for the wing design of FWMAVs that use an elastic drive mechanism. Chapter 4 investigated the optimal wing stiffness. Results showed that a rectangular wing with an optimal twist can save about 5 percents of power during hovering flight as compared the optimal design based on a rigid wing planform.
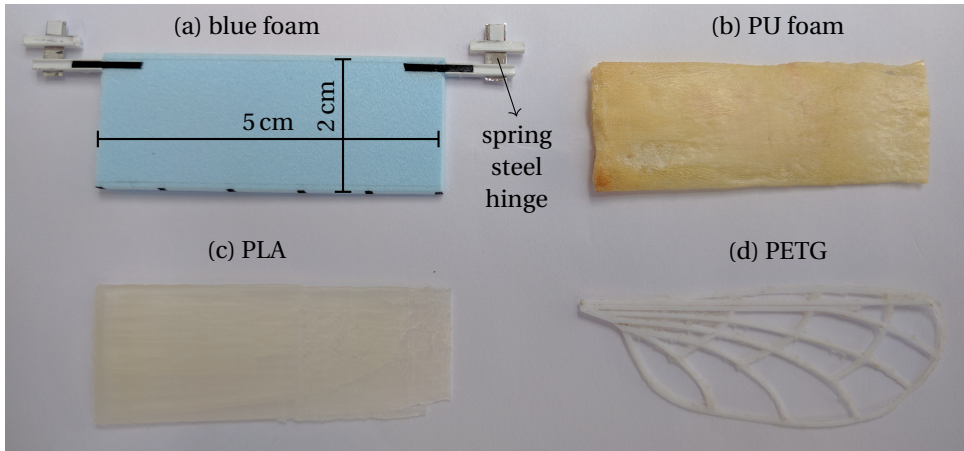
Figure 6.1: Four wings made of different materials. All of their wing roots are at the left side.

In Chapter 5, we studied the elastic hinge design consisting of stacked layers which can be stuck together using electrostatic loads. As demonstrated by the experimental results, the change of the active hinge stiffness can induce a considerable change of the pitching amplitude. Therefore, it is a promising approach for flapping wing flight control with refined fabrication techniques. The wing designs presented in Chapters 3, 4 and 5 can be classified as the component-level designs. Therefore, an integrated design which simultaneously includes all these aspects might be helpful for a more practical flapping wing.

6.3. FLAPPING WING FABRICATION AND MEASUREMENTS

6.3.1. FABRICATION

In Chapter 5, we used wings made of blue foam (i.e., Expanded Polystyrene with a Young's modulus 3 GPa) and spring steel hinges to validate the active hinge design. The blue foam is a lightweight material with a density of around $60 \, \text{kg/m}^3$ which is close to the average density of the hawkmoth wing (about $50 \, \text{kg/m}^3$). The spring steel has the advantage of long fatigue life when subjected to cyclic loading, which is important for flapping wing tests. However, there exists residual stress in the spring steel due to the spooling process during packaging. The residual stress leads to asymmetric bending stiffness, which causes unexpected asymmetric downstroke and upstroke, as observed from the experiment presented in Chapter 5.

Wings made of other materials, as shown in Fig. 6.1, have been fabricated using different approaches. Figure 6.1(b) shows a wing made of polyurethane foam (PU foam), which was fabricated using silicon rubber molds Ideally, the density of PU foam (about $35 \, \text{kg/m}^3$) is lower than the blue foam. However, the surface of the wing based on the fabrication method we use is much denser than inside. Consequently, the average density of this wing is more than three times of the blue foam wing. The damping coefficient of the PU foam wing is also much higher than the blue foam wing, which can cause extra

energy loss. The wing shown in Fig. 6.1(c) was printed in polylactic acid (PLA), which is fairly rigid and heavy (about 1.6 g). The rigidity is helpful for experiments which expect to get rid of the influence from wing flexibility, for instance, to validate the influence of the PA location on the passive pitching behavior, as presented in Chapter 3. The 3D printing techniques give freedom to the wing design in terms of shape and mass distribution. To introduce flexibility to the printed wing, instead of using PLA, polyethylene terephthalate glycol-modified (PETG) was used to print the wing venation as shown in Fig. 6.1(d). The venation is lightweight (about 0.12 g) and flexible as a result of the favorable properties of PETG. If combined with proper methods to integrate membrane with the printed venation, it is a very promising approach to fabricate artificial wings with complex morphology.

The artificial wings we have fabricated are all full-scale (close to the adult hawkmoth wing). This is because of the difficulty in using dynamically scaled wing to mimic the FSI behavior of flexible flapping wings during hovering flight. Dimensional analysis (Kang *et al.*, 2011) shows that four dimensionless parameters have to be kept identical between the real wing and the dynamically-scaled wing. These dimensionless parameters include the Reynolds number, reduced frequency, effective stiffness and the density ratio. Reynolds number represents the ratio between inertial forces and viscous forces of the fluid and governs the laminar or turbulent state of the fluid. Induced frequency compares the reference length of the wing with the spatial wavelength of the flow disturbance. Effective stiffness describes the ratio between flexural stiffness of the wing and moment of the fluid dynamic forces. Density ratio represents the ratio between the inertial force of wing and the fluid dynamic force. The same Reynolds number and reduced frequency are easy to realize. However, the effective stiffness and density ratio are difficult to keep simultaneously with the Reynolds number and induced frequency. Consequently, the flexible wings in real scale are preferred for studying the interaction between flexible wing structures and surrounding fluid.

6.3.2. Measurements

To validate new wing designs, we need to measure the corresponding wing kinematics, aerodynamic force and torque as well as the power consumption.

In Chapter 5, we measured the passive pitching motions with respect to different voltages applied on the active hinge. In this experiment, a single high-speed camera was used, and its position and orientation were fixed such that the optical axis of the camera is perpendicular to the stroke plane of the tested wings (see Fig. 5.12). The distance of two chordwise markers, which changes over time on images due to the pitching motion, was used to calculate the pitching angles. However, it was hard to see the markers on images when the chord line becomes parallel to the optical axis. This caused data loss at small pitching angles. To overcome this shortcoming, we used two cameras shooting from different directions in another experiment, which aimed to check the influence of PA location on the behavior of the passive pitching motion. The camera calibrations and error estimation (Zhang, 2000, Hedrick, 2008) were done before measuring the wing kinematics. Due to the asymmetry introduced by the elastic hinge, there existed a dramatic difference between the pitching motion during upstroke and downstroke. Since it was hard to model the hinge asymmetry, we were not able to compare the experimental

and numerical results. For this reason, this part is not included in the thesis.

In order to measure the forces and torques applied on the full-scale flapping wings of our interest, rough specifications for the experimental setup were proposed. These specifications include:

- the servo motor can directly flap a wing with a length of 5 cm and a mass of 50 mg at a frequency of 30 Hz (this wing can generate about 10 mN cycle-averaged lift force),
- the setup can measure a force (include both the aerodynamic and inertial forces) in the range of -100 mN to 100 mN with a resolution of 0.2 mN to identify the non-smooth performance,
- and the setup can measure a torque in the range of -3 μNm to 3 μNm with a resolution of 10 nNm.

To our knowledge, no commercial transducers are available to measure the targeted force and torque. Therefore, the setup, as shown in Fig. 6.2, was designed. The idea is to indirectly measure the external force and torque applied on flapping wings by measuring the deflection of the wing root. In order to measure the deflection, two mirrors are fixed at the top and side of the wing root. Two laser beams from laser pointers are shot onto the mirrors and reflected to two white boards, as illustrated by the red and green laser beams in Fig. 6.2. The movements of the laser spots on the white boards as a result of the wing root deflection are read out by two cameras. During the measurement, the positions and orientations of the laser pointers, the white boards and the cameras are fixed after the calibration. Therefore, it is impossible to measure the time-vary force and torque from a single flapping cycle. The solution is to do measurements in different flapping cycles by continuously shifting the centerline of the circular sector formed by the wing sweeping by a small angle. To ensure the accuracy, the motion of the shifted flapping wing has to be stable before doing each measurement.

The experimental setup as shown in Fig. 6.2 is the first prototype and has not been calibrated and tested yet. Therefore, more work needs to be done before it can be used in the following projects.

6
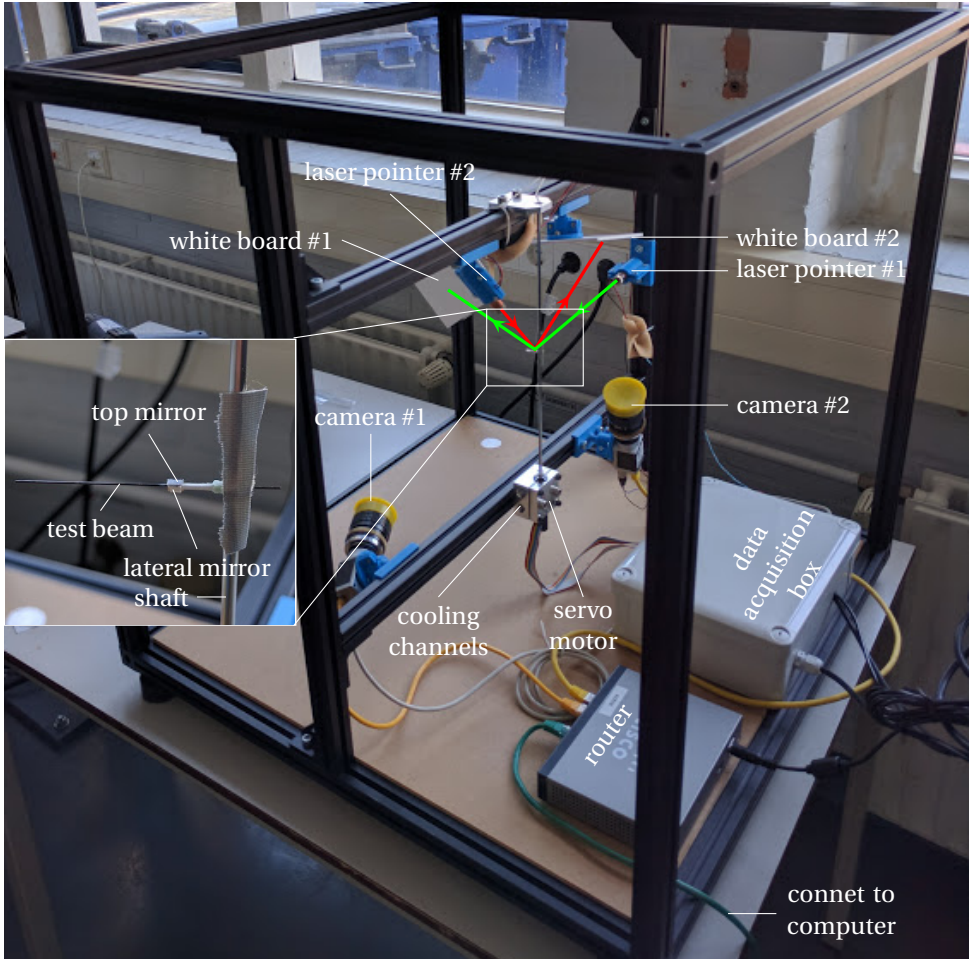
Figure 6.2: Experimental setup for measuring the force and torque applied on flapping wings. The blue and red lines illustrate two laser beams that are shot from two laser pointers onto the top and lateral mirrors, respectively, and then reflected to two white boards. The movements of the laser spots on the white boards are read out by two cameras.

7

GENERAL CONCLUSIONS AND RECOMMENDATIONS

The previous chapter retrospected and discussed the most important aspects related to the modeling, design and optimization of flapping wings for efficient hovering flight. In this chapter, the overall conclusions will be drawn and recommendations for further study will be provided.

7.1. CONCLUSIONS

In this thesis, we have worked towards more power-efficient flapping wing designs for hovering flight as compared to most existing wing designs. Progress has been made on the wing modeling, design and optimization.

We have proposed a quasi-steady aerodynamic model for flapping wings, particularly for wings with passive pitching motion. The quasi-steady model can accurately predict both the aerodynamic loads and the corresponding center of pressure. The model does not rely on any empirical parameters and can be used to evaluate the aerodynamic performance of wings with different shapes and kinematics. To further enable the parametric study and optimization of twistable flapping wings, a computationally efficient fluid-structure interaction model was also proposed by using the quasi-steady aerodynamic model and an analytical twist model. It has been shown that a quadratic polynomial can accurately model the twist of a rectangular wing with large twist amplitudes.

It has been shown that, for wings with passive pitching motion, the pitching axis location plays a very important role for power efficiency of hovering flight. Comparisons show that an optimal pitching axis can save up to 33% of power when compared to traditional wings with optimal kinematics but a straight leading edge as the pitching axis. With the optimized pitching axis, flapping wings show high pitching amplitudes and start the pitching reversal in advance of the sweeping reversal. These phenomena lead to high lift-to-drag ratios and explain the low power consumption. In addition, the optimized pitching axis provides the drive system higher potential to recycle kinetic energy during the deceleration phases as compared to traditional wings. This is because the aerodynamic power before pitching reversals is negligible for wings with optimal PA, while the traditional wings still experience a significant amount of aerodynamic power consumption before reversals. This observation underlines the particular importance of the wing pitching axis location for power-efficient FWMAVs when using kinetic energy recovery drive systems.

We have also shown that the optimized twistable wings can not dramatically outperform the optimized rigid wings in terms of the power efficiency, unless the pitching amplitude at the wing root is limited. With the decrease of the pitching amplitude at the root, the optimized rigid wings need more power for hovering. However, the optimized twistable wings can always maintain high power efficiency by introducing a certain amount of twist to increase the overall pitching amplitude. Moreover, the high computational efficiency of the proposed FSI model allows to study the flexibility of insect wings and help the wing design for FWMAVs.

A promising method to actively control the passive pitching motion of a flapping wing has also been presented by using electrostatic control of the stiffness of the wing elastic hinge. The hinge is realized by stacking three conducting spring steel layers which are separated by dielectric Mylar films. Our theoretical model shows that the stacked layers can switch from slipping with respect to each other to sticking together when the electrostatic load between layers, which can be controlled by the applied voltage, is above a threshold value. The switch can result in a dramatic increase of the hinge stiffness (about 9×) such that a short duration of the sticking still can lead to a considerable change of the passive pitching motion. Experimental results successfully confirmed the decrease of the pitching amplitude with the increase of the applied voltages. Moreover,

flight control based on electrostatically controlled hinges can be very power-efficient since there is, ideally, no power consumption associated with the control operations.

7.2. RECOMMENDATIONS

As retrospected, we have provided some approaches to achieve power-efficient flapping wing designs for hovering flight. However, there are still many open questions and challenges concerning the wing modeling, design, optimization, fabrication and testing.

The proposed quasi-steady aerodynamic model was validated for rigid wings. However, how to integrate the influence of wing camber and bending into the model needs to be investigated. In addition, the clap-and-fling phenomenon exists for the four-winged Atalanta FWMAV. Therefore, it is also useful to include the clap-and-fling mechanism into the model to reflect the interactions between adjacent wings. The challenge is how to integrate these extra terms into the model using as less empirical parameters as possible.

The proposed FSI model generally overestimates the wing stiffness as a result of the assumptions used by the analytical twist model. The overestimation can be reduced by using more accurate formulations to describe the spanwise wing displacement and allowing the chord length to change with the twist angle. In addition, the FSI model has two limitations. First, the model is limited to wings with uniform thickness. This limitation can be eliminated by updating the plate model by including the influence of the thickness variation. Second, for extremely large twist, the accuracy of the proposed FSI model can not be guaranteed since the plate theory for a moderate deformation is used. To overcome this limitation, one cheap solution is to divide the whole wing into finite parts and virtually connect adjacent parts with torsional springs. The proposed FSI model can be applied to each part separately. As a consequence, the wing displacement at the connection edges will be not differentiable, which might introduce some artificial stiffness. However, this extended model can be very useful to study the twist of insect wings that consist of a fore-wing and a hind-wing, like hawkmoth wings. With the extended quasi-steady aerodynamic model, we can extend the proposed FSI model as well. To do so, the elastic deformation needs to be updated to take the camber and bending into consideration.

The dynamic behavior of the passive pitching motion can vary dramatically for different values of the undamped frequency ratio of the flapping wing system. The changes of the pitching motion can be reflected by the pitching amplitude, output frequency, status of convergence, phase lag between the pitching and sweeping motion. The frequency ratio is influenced by many factors, including the drive frequency, the wing stiffness, the wing pitching axis location and the mass distribution. It is useful to further study (1) how to achieve a robust wing design by keeping the wing working in a range where the pitching motion is the least sensitive to the influential factors, and (2) how to make use of the sensitivity of the passive pitching motion with respect to the influential factors for control purposes.

In this work, we assume that both the sweeping motion and the wing stiffness when bended to both sides are symmetric. Therefore, the passive pitching motion is also symmetric. However, it is quite common to have asymmetric sweeping motion, pitching motion and wing stiffness for insect wings. More complex descriptions of the sweeping

motion and the wing stiffness should be introduced to better study insect wings. For instance, two harmonic functions with a same frequency but different amplitudes can be used to describe the sweeping motion in two half-strokes, respectively. A quadratic polynomial can be used to achieve asymmetric wing root stiffness, while the cubic polynomial term can introduce extra nonlinear effect to the wing root stiffness.

An interesting phenomenon was observed during the wing shape and stiffness optimization when two of the design variables are of similar characteristics (e.g., $\hat{d}_r$ and $\hat{d}_t$, k_η and E). If we plot the contour lines corresponding to the lift constraint function and the power consumption on the plane expanded by these two variables, it can be observed that the zero lift contour line is approximately parallel to the nearby power contour lines. Therefore, different combinations of these two variables can result in similar power efficiency. It would be interesting to investigate the relation between this phenomenon with the diversity of the wing morphology in nature.

The models proposed in this thesis can provide an optimal wing shape and stiffness corresponding to minimal power consumption. However, there is still a gap between these optimal wing designs and the realization of these wings. To bridge the gap, an integrated design which considers both the wing shape and stiffness is required, and more advanced structural design or optimization techniques need to be applied. For instance, if a carbon-fiber-reinforced-membrane wing is expected for the final wing design, an integrated optimization need to be conducted by directly using an appropriate wing stiffness model for this type of wing. If a freeform wing structure is wanted, topology optimization technique can be used to automate the wing structural design.

For the active hinge design, the fabrication process needs to be optimized by using well-designed tools to reduce manufacturing inaccuracies. It is also interesting to conduct long-lasting experiments to study the influence of wear between the Mylar and conducting sheets. The ultimate aim of the wing design is to realize workable flapping wings. Therefore, the testing of the designed wings is very important. The testing should include the aerodynamic force generation, the power efficiency and the strength of the fabricated wing.

A

DERIVATION OF RELATION BETWEEN 2D AND 3D LIFT COEFFICIENTS

Based on the discretized wing using the blade element method (BEM), the resultant lift on a rigid flapping wing can be calculated by

$$L^{\text{trans}} = \int_0^R \frac{1}{2} \rho^{\text{f}} v^2 C_l^{\text{trans}} c \, dx_c, \tag{A.1}$$

where the 2D lift coefficient C_l^{trans} is a constant for a given angle of attack. Considering the fact that along the span $v = \omega_{z_i} x_c$, above equation can be rewritten as

$$L^{\text{trans}} = \frac{1}{2} \rho^{\text{f}} \omega_{z_i}^2 R^2 \hat{r}_2^2 C_l^{\text{trans}} S, \tag{A.2}$$

where S is the wing area ($= \int_0^R c \, dx_c$), and $\hat{r}_2$ is the span-normalized distance from the root chord to the gyradius which is given by

$$\hat{r}_2 = \sqrt{\frac{1}{SR^2} \int_0^R x_c^2 c \, dx_c}. \tag{A.3}$$

When the translation velocity at the gyradius is taken as the reference velocity, the lift force based on 3D lift coefficient C_L^{trans} can be written as

$$L^{\text{trans}} = \frac{1}{2} \rho^{\text{f}} \left(\hat{r}_2 R \omega_{z_i} \right)^2 C_L^{\text{trans}} S. \tag{A.4}$$

By comparing Eqs. A.2 and A.4, it can be seen found that C_L^{trans} can be used directly as the 2D lift coefficient C_l^{trans} for the BEM as long as the reference velocity is at gyration.

B

DERIVATION OF AERODYNAMIC LOAD ON A UNIFORMLY ROTATING PLATE IMMERSED IN AN INCOMING FLOW

To derive the loads experienced by a plate uniformly rotating around its pitching axis at zero angle of attack (AOA) when immersed in an incoming flow with a velocity of v_{z_c}, the acceleration potential method is used (Fung, 1993). Assuming that the rotational angle is infinitesimal and the velocity of the incoming flow is much higher than the rotational velocity, the horizontal offset of the plate due to the rotation is negligible. Setting the time with respect to zero AOA to be $t = 0$, the plate position can be described as a function of time

$$y_{\mathrm{w}} = \omega_{x_c} t \left(x_{\mathrm{w}} + c\hat{d} - \frac{c}{2} \right), \quad -\frac{c}{2} \le x_{\mathrm{w}} \le \frac{c}{2}, \tag{B.1}$$

where x_{w} and y_{w} are axes of the introduced frame as shown in Fig. B.1.

The fluid surrounding the plate needs to satisfy three boundary conditions (BCs): (1) the flow on its surface must be tangent to the plate both in the velocity and acceleration field; (2) the Kutta condition has to be satisfied at the trailing edge (TE); (3) the fluid acceleration at infinity should be zero. For inviscid and incompressible flow, the momentum equation can be written as

$$\boldsymbol{a}^{\mathrm{f}} = \nabla (\Phi), \tag{B.2}$$

where $\boldsymbol{a}^{\mathrm{f}}$ represents the fluid acceleration, and Φ is the acceleration potential which is equal to $-p/\rho^{\mathrm{f}}$. This implies that the static pressure p is proportional to the acceleration potential Φ. Meanwhile, there exists a conjugate function Ψ orthogonal to Φ and satisfying

$$\frac{\partial \Phi}{\partial x_{\mathrm{w}}} = \frac{\partial \Psi}{\partial y_{\mathrm{w}}} = v_{x_{\mathrm{w}}}, \qquad \frac{\partial \Phi}{\partial y_{\mathrm{w}}} = -\frac{\partial \Psi}{\partial x_{\mathrm{w}}} = v_{y_{\mathrm{w}}}. \tag{B.3}$$
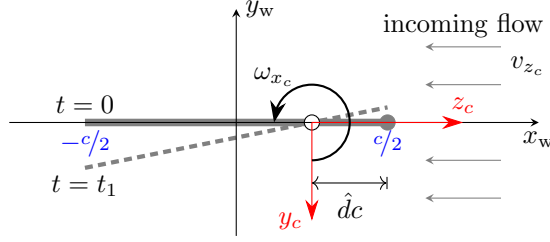
115

Figure B.1: Illustration of a plate uniformly rotating around its pitching axis within an infinitesimal time interval t_1 when immersed horizontally in an incoming flow at velocity of v_{z_c}.

Then, a complex acceleration potential W can be constructed as

$$W(z) = \Phi + j\Psi, \tag{B.4}$$

where z is a complex variable (i.e., $z = x_w + j y_w$) on the complex plane. Instead of searching for Φ that satisfies all the BCs, it is easier to construct the corresponding complex acceleration potential W. According to the linearized theory, for a plate at infinitesimal AOA, BCs can be applied to the projection of the plate on the x_w axis. The plate on the initial complex plane is mapped to a circle on the ζ complex plane with conformal transformation

$$z = \frac{1}{2}\left(\zeta + \frac{c^2}{4\zeta}\right). \tag{B.5}$$

On the ζ plane, the flow field described by the following complex acceleration potential

$$W(\zeta) = \frac{jA_0}{\zeta - c/2} + \frac{jA_1}{\zeta} \tag{B.6}$$

has the potential to satisfy all three BCs. Firstly, it is continuous at the TE, which means that the Kutta condition is satisfied. Secondly, $W(\zeta)$ tends to be zero at infinity which implies that the acceleration also tends to zero. Therefore, the flow field automatically satisfies the BC at infinity. Thirdly, the coefficients A_0 and A_1 can be determined by applying the velocity and acceleration BCs on the plate surface. Their boundary values are

$$v_{y_w} = \frac{Dy_w}{Dt} = -v_{z_c}\omega_{x_c}t + \omega_{x_c}\left(x_w + c\hat{d} - \frac{c}{2}\right), \tag{B.7}$$

$$a_{y_w} = \frac{D^2 y_w}{Dt^2} = -2v_{z_c}\omega_{x_c}. \tag{B.8}$$

The normal component of the fluid acceleration on the circle (ζ plane) can be calculated by

$$a_r^f\Big|_{|\zeta|=c/2} = \frac{\partial\Re(W)}{\partial r}\Big|_{|\zeta|=c/2} = -\frac{4}{c^2}A_1\sin\gamma, \tag{B.9}$$

where r ($r = c/2$ on the circle) and γ are polar coordinates on the ζ plane. $a_r^f\big|_{|\zeta|=c/2}$ should be equal to $a_{y_w}\sin\gamma$ in order to satisfy the acceleration BC on the plate surface,

whereby the coefficient A_1 is obtained as

$$A_1 = \frac{1}{2} v_{z_c} \omega_{x_c} c^2. \tag{B.10}$$

The velocity BC can be used to calculate the coefficient A_0. The fluid velocity $v^{\mathrm{f}}_{y_\mathrm{w}}$ on the plate in the ζ plane can be calculated by solving the partial differentiation equation

$$\frac{\partial v^{\mathrm{f}}_{y_\mathrm{w}}}{\partial t} - v_{z_c} \frac{\partial v^{\mathrm{f}}_{y_\mathrm{w}}}{\partial x_\mathrm{w}} = a^{\mathrm{f}}_{y_\mathrm{w}} = -\frac{\partial \Psi}{\partial x_\mathrm{w}}. \tag{B.11}$$

The fluid velocity on the plate can be obtained as

$$v^{\mathrm{f}}_{y_\mathrm{w}} = \frac{\Psi}{v_{z_c}} + h(v_{z_c} t + x_\mathrm{w}), \tag{B.12}$$

where $h(\cdot)$ can be an arbitrary function of the expression $v_{z_c} t + x_\mathrm{w}$, and Ψ is equal to $2 v_{z_c} \omega_{x_c} x_\mathrm{w} - A_0/c$ which is obtained from Eq. B.6 by substituting ζ with z which is determined by x_w and y_w. If we let $h(v_{z_c} t + x_\mathrm{w})$ be $-\omega(v_{z_c} t + x_\mathrm{w})$, and apply the velocity BC that the fluid velocity $v^{\mathrm{f}}_{y_\mathrm{w}}$ is equal to the boundary value of the velocity given in Eq. B.7 over the plate except for the singular point at the LE, we get

$$A_0 = v_{z_c} \omega_{x_c} c^2 \left(\frac{1}{2} - \hat{d} \right). \tag{B.13}$$

Substituting Eqs. B.10 and B.13 into B.6, the acceleration potential Φ can be obtained as

$$\Phi = v_{z_c} \omega_{x_c} c \sin(\gamma) - \frac{2 v_{z_c} \omega_{x_c} \sin(\gamma) c (\hat{d} - \frac{1}{2})}{(1 - \cos(\gamma))^2 + \sin^2(\gamma)} \tag{B.14}$$

with which the pressure distribution can be calculated. Eventually, the lift L and torque τ about the pitching axis due to the coupling effect on a plate with unity span can be obtained by integrating the pressure over the entire circle on the ζ plane, resulting in,

$$L = \pi \rho^{\mathrm{f}} v_{z_c} \omega_{x_c} c^2 \left(\frac{3}{4} - \hat{d} \right) + \frac{1}{4} \pi \rho v_{z_c} \omega_{x_c} c^2, \tag{B.15}$$

$$\tau = \pi \rho^{\mathrm{f}} v_{z_c} \omega_{x_c} c^3 \left(\frac{3}{4} - \hat{d} \right) \left(\frac{1}{4} - \hat{d} \right) + \frac{1}{4} \pi \rho v_{z_c} \omega_{x_c} c^3 \left(\frac{3}{4} - \hat{d} \right), \tag{B.16}$$

from which it can be seen that the lift consists of two components which act at the 1/4 chord and 3/4 chord, respectively. The first component can be regarded as a result of a wing rotation-induced vorticity concentrated at the 1/4 chord while satisfying the boundary condition for the downwash at the 3/4 chord location, and the second component is a result of Coriolis effect experienced by the fluid with equivalent mass of $\frac{1}{4} \pi \rho^{\mathrm{f}} c^2$ while flowing on a rotating wing. It should be noted that τ is, by convention, considered to be positive when it acts to pitch the plate in the nose-up direction.

C

DERIVATION OF GOVERNING EQUATION FOR PASSIVE PITCHING MOTION OF A RIGID WING

In this Appendix, the equation of motion that governs the passive pitching motion of flapping wings is derived.

Generally, the passive pitching motion is achieved by connecting the wing to the drive mechanism with an elastic hinge while the drive mechanism applies a sweeping torque. Then, the wing is forced to pitch about the pitching axis by the wing inertia and aerodynamic loads. Since the out-of-plane motion is not completely constrained, a slight heaving motion might be observed, as shown in the second validation case. Indeed, the heaving motion has a small contribution to the drive torque and the passive pitching motion. The contribution of gravity to the passive pitching motion is ignored due to the small wing mass and the fact that the centre of mass is not far away from the pitching axis.

Since the moment of inertia I of the wing is constant in the co-rotating frame, Euler's second law of motion for a rigid body is applied about the pitching axis of the wing (i.e., x_c axis), namely,

$$\tau_{x_c}^{\text{applied}} + \tau_{x_c}^{\text{iner}} = 0, \tag{C.1}$$

where $\tau_{x_c}^{\text{applied}}$ consists of the elastic torque $\tau_{x_c}^{\text{elas}}$ $(= -k_\eta \eta)$ from the hinge and the aerodynamic torque $\tau_{x_c}^{\text{aero}}$ which includes four parts as presented in Section 2.2.2. The inertial torque in the co-rotating frame can be calculated by

$$\boldsymbol{\tau}^{\text{iner}} = -I\boldsymbol{\alpha}_c - \boldsymbol{\omega_c} \times (I\boldsymbol{\omega}_c), \tag{C.2}$$

where $\boldsymbol{\omega}_c$ and $\boldsymbol{\alpha}_c$ are the angular velocity and acceleration in the co-rotating frame, and the two components are the torque due to Euler and Coriolis forces, respectively. The

component of $\boldsymbol{\tau}^{\text{iner}}$ on x_c axis can be divided into the term $-I_{x_c x_c}\ddot{\eta}$ and the inertial drive torque $\tau_{x_c}^{\text{drive}}$ which can be expressed as

$$\tau_{x_c}^{\text{drive}} = I_{x_c x_c}\left[\frac{1}{2}\dot{\phi}^2\cos^2\theta\sin(2\eta) - \frac{1}{2}\dot{\theta}^2\sin(2\eta) + 2\dot{\phi}\dot{\theta}\cos\theta\cos^2\eta + \ddot{\phi}\sin\theta\right] +$$
$$I_{x_c z_c}\left[\ddot{\theta}\sin\eta + \frac{1}{2}\dot{\phi}^2\sin(2\theta)\sin\eta - \ddot{\phi}\cos\theta\cos\eta + 2\dot{\phi}\dot{\theta}\sin\theta\cos\eta\right]. \quad \text{(C.3)}$$

Eventually, the equation of motion of the wing pitching can be expressed as

$$I_{x_c x_c}\ddot{\eta} + k_\eta\eta = \tau_{x_c}^{\text{aero}} + \tau_{x_c}^{\text{drive}}. \quad \text{(C.4)}$$

REFERENCES

ALLEN, H. G. 1969 *Analysis and design of structural sandwich panels*. Pergamon.

ANDERSEN, A., PESAVENTO, U. & WANG, Z. J. 2005 Unsteady aerodynamics of fluttering and tumbling plates. *Journal of Fluid Mechanics* **541**, 65–90.

ANDERSON, J. 2010 *Fundamentals of Aerodynamics*. McGraw-Hill Education.

ANSARI, S. A. 2004 A nonlinear, unsteady, aerodynamic model for insect-like flapping wings in the hover with micro air vehicle applications. Phd thesis, Cranfield University.

ANSARI, S. A., BIKOWSKI, R. & KNOWLES, K. 2006 Aerodynamic modelling of insect-like flapping flight for micro air vehicles. *Progress in Aerospace Sciences* **42** (2), 129–172.

ANSARI, S. A., KNOWLES, K. & ZBIKOWSKI, R. 2008 Insectlike Flapping Wings in the Hover Part II: Effect of Wing Geometry. *Journal of Aircraft* **45** (6), 1976–1990.

APPEL, E. & GORB, S. N. 2011 Resilin-bearing wing vein joints in the dragonfly Epiophlebia superstes. *Bioinspiration & biomimetics* **6**, 046006.

BERGAMINI, A., CHRISTEN, R., MAAG, B. & MOTAVALLI, M. 2006 A sandwich beam with electrostatically tunable bending stiffness. *Smart Materials and Structures* **15** (3), 678–686.

BERGOU, A. J., XU, S. & WANG, Z. J. 2007 Passive wing pitch reversal in insect flight. *Journal of Fluid Mechanics* **591**, 321–337.

BERMAN, G. J. & WANG, Z. J. 2007 Energy-minimizing kinematics in hovering insect flight. *Journal of Fluid Mechanics* **582**, 153–168.

BETTS, C. R. & WOOTTON, R. J. 1988 Wing shape and flight behaviour in butterflies (Lepidoptera: Papilionoidea and Hesperioidea): a preliminary analysis. *Journal of Experimental Biology* **288** (1), 271–288.

BIRCH, J. M. & DICKINSON, M. H. 2001 Spanwise flow and the attachment of the leading-edge vortex on insect wings. *Nature* **412** (6848), 729–733.

BOLSMAN, C. T. 2010 Flapping wing actuation using resonant compliant mechanisms, an insect inspired design. Doctoral thesis, Technische Universiteit Delft.

BOLSMAN, C. T., GOOSEN, J. F. L. & VAN KEULEN, F. 2009 Design overview of a resonant wing actuation mechanism for application in flapping wing MAVs. *International Journal of Micro Air Vehicles* **1** (4), 263–272.

BRENNEN, C. E. 1982 A review of added mass and fluid inertial forces. *Tech. Rep.*. Naval Civil Engineering Laboratory, Port Hueneme, California.

CHABRIER, J. 1822 *Essai sur le vol des insectes, et observations*. Kessinger Publishing.

CHANUTE, O. 1894 *Progress in Flying Machines*. Courier Corporation.

CHAUDHURI, A., HAFTKA, R., IFJU, P. G., VILLANUEVA, D., CHANG, K. & RUE, J. 2013 Experimental Optimization and Uncertainty Quantification of Flapping Wing of a Micro Air Vehicle. In *10th World Congress on Structural and Multidisciplinary Optimization*, pp. 1–10. Orlando, Florida, USA.

CHEN, Y., SKOTE, M., ZHAO, Y. & HUANG, W. 2013 Dragonfly (Sympetrum flaveolum) flight: Kinematic measurement and modelling. *Journal of Fluids and Structures* **40**, 115–126.

CLARK, W. W. 2000 Vibration Control with State-Switched Piezoelectric Materials. *Journal of Intelligent Material Systems and Structures* **11** (4), 263–271.

COMBES, S. A. & DANIEL, T. L. 2003 Flexural stiffness in insect wings. II. Spatial distribution and dynamic wing bending. *The Journal of experimental biology* **206**, 2989–2997.

DE CROON, G. C. H. E., DE CLERCQ, K. M. E., RUIJSINK, R., REMES, B. & DE WAGTER, C. 2009 Design, aerodynamics, and vision-based control of the DelFly. *International Journal of Micro Air Vehicles* **1** (2), 71–98.

DAI, H., LUO, H. & DOYLE, J. F. 2012 Dynamic pitching of an elastic rectangular wing in hovering motion. *Journal of Fluid Mechanics* **693**, 473–499.

DICKINSON, M. H. & GÖTZ, K. G. 1993 Unsteady aerodynamic performance of model wings at low Reynolds numbers. *Journal of Experimental Biology* **64**, 45–64.

DICKINSON, M. H., LEHMANN, F. O. & SANE, S. P. 1999 Wing rotation and the aerodynamic basis of insect flight. *Science* **284** (5422), 1954–1960.

DICKSON, W. B., STRAW, A. D., POELMA, C. & DICKINSON, M. H. 2006 An integrative model of insect flight control. In *Proceedings of the AIAA Aerospace Sciences Meeting and Exhibit*, pp. 1–19. Reno, NV.

DONOUGHE, S., CRALL, J. D., MERZ, R. A. & COMBES, S. A. 2011 Resilin in dragonfly and damselfly wings and its implications for wing flexibility. *Journal of morphology* **272** (12), 1409–21.

DU, G. & SUN, M. 2008 Effects of unsteady deformation of flapping wing on its aerodynamic forces. *Applied Mathematics and Mechanics* **29** (6), 731–743.

DU, G. & SUN, M. 2010 Effects of wing deformation on aerodynamic forces in hovering hoverflies. *The Journal of experimental biology* **213**, 2273–2283.

DUDLEY, R. 2002 *The biomechanics of insect flight: form, function, evolution*. Princeton University Press.

DUDLEY, R. & ELLINGTON, C. P. 1990 Mechanics of Forward Flight in Bumblebees: I. Kinematics and Morphology. *Journal of Experimental Biology* **148** (1), 19–52.

ELDREDGE, J. D., WANG, C. & OL, M. V. 2009 A computational study of a canonical pitch-up, pitch-down wing maneuver. In *39th AIAA Fluid Dynamics Conference*, pp. 1–14. San Antonio, Texas.

ELLINGTON, C. P. 1984*a* The Aerodynamics of Hovering Insect Flight. II. Morphological Parameters. *Philosophical Transactions of the Royal Society B: Biological Sciences* **305** (1122), 17–40.

ELLINGTON, C. P. 1984*b* The Aerodynamics of Hovering Insect Flight. III. Kinematics. *Philosophical Transactions of the Royal Society B: Biological Sciences* **305** (1122), 145–181.

ELLINGTON, C. P. 1984*c* The aerodynamics of hovering insect flight. IV. aerodynamic mechanisms. *Philosophical Transactions of the Royal Society B: Biological Sciences* **305** (1122), 79–113.

ELLINGTON, C. P. 1984*d* The aerodynamics of hovering insect flight. V. a vortex theory. *Philosophical Transactions of the Royal Society B: Biological Sciences* **305** (1122), 115–144.

ELLINGTON, C. P. 1999 The novel aerodynamics of insect flight: applications to micro-air vehicles. *The Journal of experimental biology* **202**, 3439–3448.

ELLINGTON, C. P., VAN DEN BERG, C., WILLMOTT, A. P. & THOMAS, A. L. R. 1996 Leading-edge vortices in insect flight. *Nature* **384** (6610), 626–630.

ENNOS, A. R. 1989 Inertial and aerodynamic torques on the wings of diptera in flight. *J. Exp. Biol.* **142** (1), 87–95.

FINIO, B. M. & WOOD, R. J. 2012 Open-loop roll, pitch and yaw torques for a robotic bee. In *2012 IEEE/RSJ International Conference on Intelligent Robots and Systems*, pp. 113–119. Vilamoura, Algarve, Portugal: IEEE.

FLOREANO, D. & WOOD, R. J. 2015 Science, technology and the future of small autonomous drones. *Nature* **521** (7553), 460–466.

FORD, C. W. P. & BABINSKY, H. 2014 Impulsively started flat plate circulation. *AIAA Journal* **52** (8), 1800–1802.

FREE FLIGHT SUPPLIES 2015 www.freeflightsupplies.co.uk/mylarspec.pdf.

FUNG, Y. C. 1993 *An introduction to the theory of aeroelasticity*. Courier Dover Publications.

GOLDFARB, M. & SPEICH, J. E. 1999 A Well-Behaved Revolute Flexure Joint for Compliant Mechanism Design. *Journal of Mechanical Design* **121** (3), 424.

GRAY, C. 2003 Leonardo da Vinci, http://www.flyingmachines.org/davi.html.

HA, N. S., TRUONG, Q. T., PHAN, H. V., GOO, N. S. & PARK, H. C. 2014 Structural Characteristics of Allomyrina Dichotoma Beetle's Hind Wings for Flapping Wing Micro Air Vehicle. *Journal of Bionic Engineering* **11** (2), 226–235.

HAN, J. S., KIM, J. K., CHANG, J. W. & HAN, J. H. 2015 An improved quasi-steady aerodynamic model for insect wings that considers movement of the center of pressure. *Bioinspiration & Biomimetics* **10**, 046014.

HARBIG, R. R., SHERIDAN, J. & THOMPSON, M. C. 2014 The role of advance ratio and aspect ratio in determining leading-edge vortex stability for flapping flight. *Journal of Fluid Mechanics* **751**, 71–105.

HEDRICK, T. L. 2008 Software techniques for two- and three-dimensional kinematic measurements of biological and biomimetic systems. *Bioinspiration & biomimetics* **3**, 034001.

VAN DEN HEUVEL, H. 2015 Conceptual Development of a Catalytic Expansion Actuator for a Resonating-body Flapping-wing Micro Air Vehicle. Master's thesis.

HOFF, W. 1919 Der flug der insekten und der vögel. *Die Naturwissenschaften* **7** (10), 159–162.

HOU, D., YIN, Y., ZHAO, H. & ZHONG, Z. 2015 Effects of blood in veins of dragonfly wing on the vibration characteristics. *Computers in Biology and Medicine* **58**, 14–19.

HOWELL, L. L. 2001 *Compliant mechanisms*. John Wiley & Sons.

ISHIHARA, D., HORIE, T. & DENDA, M. 2009 A two-dimensional computational study on the fluid–structure interaction cause of wing pitch changes in dipteran flapping flight. *Journal of Experimental Biology* **212**, 1–10.

JOHANSSON, L. C., ENGEL, S., KELBER, A., HEERENBRINK, M. K. & HEDENSTRÖM, A. 2013 Multiple leading edge vortices of unexpected strength in freely flying hawkmoth. *Scientific reports* **3**, 3264.

JONES, R. T. 1940 The unsteady lift of a wing of finite aspect ratio. *Tech. Rep.*.

JUDY, J. W. 2001 Microelectromechanical systems (MEMS): fabrication, design and applications. *Smart Materials and Structures* **10** (6), 1115–1134.

KANG, C. K., AONO, H., CESNIK, C. E. S. & SHYY, W. 2011 Effects of Flexibility on the Aerodynamic Performance of Flapping Wings. In *6th AIAA Theoretical Fluid Mechanics Conference*, pp. 1–46. Honolulu, Hawaii.

KEENNON, M., KLINGEBIEL, K. & WON, H. 2012 Development of the Nano Hummingbird: A Tailless Flapping Wing Micro Air Vehicle. In *50th AIAA Aerospace Sciences Meeting including the New Horizons Forum and Aerospace Exposition*, pp. 1–24. Nashville, Tennessee.

KELLY, M. 2006 *Steam in the Air: The Application of Steam Power in Aviation During the 19th and 20th Centuries*. Casemate Publishers.

LAU, G. K., CHIN, Y. W., GOH, J. T. W. & WOOD, R. J. 2014 Dipteran-insect-inspired thoracic mechanism with nonlinear stiffness to save inertial power of flapping-wing flight. *IEEE Transactions on Robotics* **30** (5), 1187–1197.

LEE, J., CHOI, H. & KIM, H. Y. 2015 A scaling law for the lift of hovering insects. *Journal of Fluid Mechanics* **782**, 479–490.

LEHMANN, F. O. 2008 When wings touch wakes: understanding locomotor force control by wake wing interference in insect wings. *The Journal of experimental biology* **211**, 224–233.

LEHMANN, F. O. & PICK, S. 2007 The aerodynamic benefit of wing-wing interaction depends on stroke trajectory in flapping insect wings. *The Journal of experimental biology* **210**, 1362–1377.

LI, H.-S. & AU, S.-K. 2010 Design optimization using Subset Simulation algorithm. *Structural Safety* **32** (6), 384–392.

LILIENTHAL, O. 1895 lilienthal.

MA, K. Y., CHIRARATTANANON, P., FULLER, S. B. & WOOD, R. J. 2013 Controlled flight of a biologically inspired, insect-scale robot. *Science* **340** (6132), 603–607.

MA, K. Y., FELTON, S. M. & WOOD, R. J. 2012 Design, fabrication, and modeling of the split actuator microrobotic bee. In *2012 IEEE/RSJ International Conference on Intelligent Robots and Systems*, pp. 1133–1140. Vilamoura, Algarve, Portugal.

MAJIDI, C. & WOOD, R. J. 2010 Tunable elastic stiffness with microconfined magnetorheological domains at low magnetic field. *Applied Physics Letters* **97**, 164104.

MARTÍ-CAMPOY, A., ÁVALOS, J. A., SOTO, A., RODRÍGUEZ-BALLESTER, F., MARTÍNEZ-BLAY, V. & MALUMBRES, M. P. 2016 Design of a Computerised Flight Mill Device to Measure the Flight Potential of Different Insects. *Sensors* **16** (485), 1–21.

MENG, X. G. & SUN, M. 2015 Aerodynamics and vortical structures in hovering fruitflies. *Physics of Fluids* **27** (031901), 1–22.

MUIJRES, F. T., ELZINGA, M. J., MELIS, J. M. & DICKINSON, M. H. 2014 Flies evade looming targets by executing rapid visually directed banked turns. *Science* **344**, 172–177.

NABAWY, M. R. A. & CROWTHER, W. J. 2014 On the quasi-steady aerodynamics of normal hovering flight part II: model implementation and evaluation. *Journal of the Royal Society Interface* **11** (20131197), 1–9.

NAKATA, T. & LIU, H. 2012*a* A fluid–structure interaction model of insect flight with flexible wings. *Journal of Computational Physics* **231** (4), 1822–1847.

NAKATA, T. & LIU, H. 2012*b* Aerodynamic performance of a hovering hawkmoth with flexible wings: a computational approach. *Proceedings of the Royal Society B: Biological Sciences* **279**, 722–731.

NEWMAN, J. N. 1977 *Marine hydrodynamics*. The MIT Press.

NGUYEN, Q.-V., CHAN, W. L. & DEBIASI, M. 2015 An insect-inspired flapping wing micro air vehicle with double wing clap-fling effects and capability of sustained hovering. In *Proc. SPIE 9429, Bioinspiration, Biomimetics, and Bioreplication* (ed. A. Lakhtakia, M. Knez & R. J. Martín-Palma), pp. 1–11. San Diego, California, United States.

OSBORNE, M. F. M. 1951 Aerodynamics of flapping flight with application to insects. *Journal of Experimental Biology* **28**, 221–245.

PERCIN, M. & VAN OUDHEUSDEN, B. W. 2015 Three-dimensional flow structures and unsteady forces on pitching and surging revolving flat plates. *Experiments in Fluids* **56** (47), 1–19.

PETERS, H. J., GOOSEN, J. F. L. & VAN KEULEN, F. 2016 Methods to actively modify the dynamic response of cm-scale FWMAV designs. *Smart Materials and Structures* **25** (5), 055027.

PETERS, H. J., WANG, Q., GOOSEN, J. F. L. & VAN KEULEN, F. 2015 Active control of the passive pitching of a flapping wing with electrostatic clamping. In *7th ECCOMAS Thematic Conference on Smart Structures and Materials (SMART 2015)*, pp. 1–19. Azores, Portugal.

PITT FORD, C. W. & BABINSKY, H. 2013 Lift and the leading-edge vortex. *Journal of Fluid Mechanics* **720**, 280–313.

RISTROPH, L. & CHILDRESS, S. 2014 Stable hovering of a jellyfish-like flying machine. *Journal of the Royal Society, Interface* **11** (20130992), 1–7.

SANE, S. P. 2003 The aerodynamics of insect flight. *Journal of Experimental Biology* **206** (23), 4191–4208.

SANE, S. P. & DICKINSON, M. H. 2002 The aerodynamic effects of wing rotation and a revised quasi-steady model of flapping flight. *J. Exp. Biol.* **205** (8), 1087–1096.

SCHLICHTING, H. & TRUCKENBRODT, E. A. 1979 *Aerodynamics of the aeroplane*, 2nd edn. McGraw Hill Higher Education.

SCHWAB, A. L. & MEIJAARD, J. P. 2006 How to draw Euler angles and utilize Euler parameters. In *Proceedings of IDETC/CIE ASME 2006 International Design Engineering Technical Conferences & Computers and Information in Engineering Conference*, pp. 1–7. Philadelphia, Pennsylvania, USA.

SELVAN, A. 2014 Simulation of optic flow based flight control for a flapping wing micro aerial vehicle. Master's thesis.

SESHADRI, P., BENEDICT, M. & CHOPRA, I. 2013 Understanding Micro Air Vehicle Flapping-Wing Aerodynamics Using Force and Flowfield Measurements. *Journal of Aircraft* **50** (4), 1070–1087.

SHAHZAD, A., TIAN, F.-B., YOUNG, J. & LAI, J. C. S. 2016 Effects of wing shape, aspect ratio and deviation angle on aerodynamic performance of flapping wings in hover. *Physics of Fluids* **28** (111901), 1–36.

SHAW, W. H. & RUHEN, O. 1977 *Lawrence Hargrave: explorer, inventor & aviation experimenter*. Cassell Australia Ltd.

SHYY, W., AONO, H., CHIMAKURTHI, S. K., TRIZILA, P., KANG, C. K., CESNIK, C. E. S. & LIU, H. 2010 Recent progress in flapping wing aerodynamics and aeroelasticity. *Progress in Aerospace Sciences* **46** (7), 284–327.

SREETHARAN, P. S., WHITNEY, J. P., STRAUSS, M. D. & WOOD, R. J. 2012 Monolithic fabrication of millimeter-scale machines. *Journal of Micromechanics and Microengineering* **22** (055027), 1–6.

STEWART, E., PATIL, M., CANFIELD, R. & SNYDER, R. 2013 Shape Optimization of a Flapping Wing. In *54th AIAA/ASME/ASCE/AHS/ASC Structures, Structural Dynamics, and Materials Conference*, pp. 1–11. Boston, Massachusetts.

SUN, M. 2014 Insect flight dynamics: Stability and control. *Reviews of Modern Physics* **86** (2), 615–646.

TABATA, O., KONISHI, S., CUSIN, P., ITO, Y., KAWAI, F., HIRAI, S. & KAWAMURA, S. 2001 Micro fabricated tunable bending stiffness devices. *Sensors and Actuators A: Physical* **89**, 119–123.

TAHA, H. E., HAJJ, M. R. & BERAN, P. S. 2014 State-space representation of the unsteady aerodynamics of flapping flight. *Aerospace Science and Technology* **34** (1), 1–11.

TANAKA, H. 2012 Flexible wing structures of simplified insect-sized flapping MAVs. In *Proceedings of 2012 ICME International Conference on Complex Medical Engineering*, pp. 397–401. Kobe, Japa.

TANAKA, H. & WOOD, R. J. 2010 Fabrication of corrugated artificial insect wings using laser micromachined molds. *Journal of Micromechanics and Microengineering* **20** (075008), 1–8.

TEOH, Z. E., FULLER, S. B., CHIRARATTANANON, P., PREZ-ARANCIBIA, N. O., GREENBERG, J. D. & WOOD, R. J. 2012 A hovering flapping-wing microrobot with altitude control and passive upright stability. In *2012 IEEE/RSJ International Conference on Intelligent Robots and Systems*, pp. 3209–3216. Vilamoura, Algarve, Portugal.

TEOH, Z. E. & WOOD, R. J. 2014 A bioinspired approach to torque control in an insect-sized flapping-wing robot. In *5th IEEE RAS/EMBS International Conference on Biomedical Robotics and Biomechatronics (BioRob)*, pp. 911–917. São Paulo, Brazil.

TOOLBOX, T. 2015 http://www.engineeringtoolbox.com.

TRAHAIR, N. S. 2005 Nonlinear Elastic Nonuniform Torsion. *Journal of Structural Engineering* **131** (7), 1135–1142.

TREASE, B. P., MOON, Y.-M. & KOTA, S. 2005 Design of Large-Displacement Compliant Joints. *Journal of Mechanical Design* **127**, 788–798.

TRIMMER, W. 1989 Microrobots and micromechanical systems. *Sensors and Actuators* **19** (3), 267–287.

USHERWOOD, J. R. & ELLINGTON, C. P. 2002*a* The aerodynamics of revolving wings I. Model hawkmoth wings. *The Journal of experimental biology* **205**, 1547–1564.

USHERWOOD, J. R. & ELLINGTON, C. P. 2002*b* The aerodynamics of revolving wings II. Propeller force coefficients from mayfly to quail. *The Journal of experimental biology* **205**, 1565–1576.

VAN WAGENINGEN, T. 2012 Design of a small scale high power density engine for micro air vehicle. Master's thesis.

WAGNER, H. 1925 Über die entstehung des dynamischen auftriebes von tragflügeln. *Zeitschrift für Angewandte Mathematik und Mechanik* **5**, 17–35.

WALKER, P. B. 1931 Experiments on the growth of circulation about a wing and an apparatus for measuring fluid motion. *Tech. Rep.*.

WALKER, S. M., SCHWYN, D. A., MOKSO, R., WICKLEIN, M., MÜLLER, T., DOUBE, M., STAMPANONI, M., KRAPP, H. G. & TAYLOR, G. K. 2014 In Vivo Time-Resolved Microtomography Reveals the Mechanics of the Blowfly Flight Motor. *PLoS Biology* **12** (3), e1001823.

WANG, Q., GOOSEN, J. F. L. & VAN KEULEN, F. 2013 Optimal hovering kinematics with respect to various flapping-wing shapes. In *International Micro Air Vehicle Conference and Flight Competition (IMAV2013)*, pp. 1–12. Toulouse, France.

WANG, Q., GOOSEN, J. F. L. & VAN KEULEN, F. 2014*a* Study of design parameters of flapping-wings. In *International Micro Air Vehicle Conference and Flight Competition (IMAV2014)*, pp. 1–10. Delft, The Netherlands.

WANG, Q., GOOSEN, J. F. L. & VAN KEULEN, F. 2016 A predictive quasi-steady model of aerodynamic loads on flapping wings. *Journal of Fluid Mechanics* **800**, 688–719.

WANG, Q., GOOSEN, J. F. L. & VAN KEULEN, F. 2014*b* Optimal pitching axis of flapping-wings for hovering flight. In *The 4th international conference on engineering optimization*, pp. 1–6. Lisbon, Portugal.

WANG, Z. J., BIRCH, J. M. & DICKINSON, M. H. 2004 Unsteady forces and flows in low Reynolds number hovering flight: two-dimensional computations vs robotic wing experiments. *The Journal of Experimental Biology* **207**, 449–460.

WEI, S., LIAN, Y., TANG, J., VIIERU, D. & LIU, H. 2008 *Aerodynamics of low Reynolds number flyers*. Cambridge University Press.

WEIS-FOGH, T. 1972 Energetics of hovering flight in hummingbirds and in Drosophila. *Journal of Experimental Biology* **56**, 79–104.

WHITNEY, J. P. & WOOD, R. J. 2010 Aeromechanics of passive rotation in flapping flight. *Journal of Fluid Mechanics* **660**, 197–220.

WILLMOTT, A. P. & ELLINGTON, C. P. 1997*a* The mechanics of flight in the hawkmoth Manduca sexta. I. Kinematics of hovering and forward flight. *The Journal of experimental biology* **200** (21), 2705–2722.

WILLMOTT, A. P. & ELLINGTON, C. P. 1997*b* The mechanics of flight in the hawkmoth Manduca sexta. II. Aerodynamic consequences of kinematic and morphological variation. *Journal of Experimental Biology* **200** (21), 2723–2745.

WOOD, R. 2008 The First Takeoff of a Biologically Inspired At-Scale Robotic Insect. *IEEE Transactions on Robotics* **24** (2), 341–347.

WOOD, R., FINIO, B., KARPELSON, M., MA, K., PEREZ-ARANCIBIA, N., SREETHARAN, P., TANAKA, H. & WHITNEY, J. 2012 Progress on 'pico' air vehicles. *The International Journal of Robotics Research* **31** (11), 1292–1302.

WOOD, R. J. 2007 Design, fabrication, and analysis of a 3DOF, 3cm flapping-wing MAV. In *Proceeding of the 2007 IEEE/RSJ International Conference on Intelligent Robots and Systems*, pp. 1576–1581. San Diego, CA, USA.

WOOTTON, R. J. 1981 Support and deformability in insect wings. *Journal of Zoology* **193** (4), 447–468.

XIA, X. & MOHSENI, K. 2013 Lift evaluation of a two-dimensional pitching flat plate. *Physics of Fluids* **25** (091901), 1–27.

ZHANG, Z. 2000 A flexible new technique for camera calibration. *IEEE Transactions on Pattern Analysis and Machine Intelligence* **22** (11), 1330–1334.

ZHAO, L., HUANG, Q., DENG, X. & SANE, S. P. 2010 Aerodynamic effects of flexibility in flapping wings. *Journal of The Royal Society Interface* **7** (44), 485–497.

ZHENG, L., HEDRICK, T. L. & MITTAL, R. 2013 Time-varying wing-twist improves aerodynamic efficiency of forward flight in butterflies. *PloS one* **8** (1), e53060.

CURRICULUM VITÆ

Qi WANG

1988.06.01	Born in Anhui Province, China.

EDUCATION

2017.01–2018.12	Postdoc in Dept. of Precision and Microsystems Engineering Delft University of Technology, Delft, The Netherlands research project: *Active smart structures*
2012.09–2016.09	Ph. D. in Dept. of Precision and Microsystems Engineering Delft University of Technology, Delft, The Netherlands
2009.09–2012.03	Postgraduate in the major of Flight Vehicle Design Northwestern Polytechnical University, Xi'an, China Master's thesis: *Reliability Based Structural Topology Optimization*
2005.09–2009.07	Undergraduate in the major of Aircraft Design Engineering Northwestern Polytechnical University, Xi'an, China
2002.09–2005.07	Anhui Lingbi First Middle School Lingbi, Anhui Province, China

AWARDS

2014.10	Best poster prize Seventeenth EM symposium, Arnhem, The Netherlands
2012.03	Outstanding postgraduate Northwestern Polytechnical University, Xi'an, China

MORE INFO

LIST OF PUBLICATIONS

JOURNAL PAPERS

1. **Wang, Q**., Goosen, J. F. L., & van Keulen, F. (2017). An Efficient Fluid-Structure Interaction Model for Optimizing Twistable Flapping Wings. 1-23. (submitted to *Journal of Fluids and Structures*).

2. **Wang, Q**., Goosen, J. F. L., & van Keulen, F. (2017). Optimal pitching axis location of flapping wings for power-efficient hovering flight. 1-23. (submitted to *Bioinspiration & Biomimetics*).

3. **Wang, Q**., Goosen, J. F. L., & van Keulen, F. (2016). A predictive quasi-steady model of aerodynamic loads on flapping wings. *Journal of Fluid Mechanics*, 800, 688-719.

BOOK CHAPTER

1. Peters, H. J., **Wang, Q.**, Goosen, J. F. L., & van Keulen, F., 2017. Active control of the hinge of a flapping wing with electrostatic sticking to modify the passive pitching motion. *In: A. L. Araujo and C. A. Mota Soares (Eds.), Smart Structures and Materials, Computational Methods in Applied Sciences 43*, Springer International Publishing Switzerland.

CONFERENCE PAPERS

1. **Wang, Q**., Goosen, J. F. L., & van Keulen, F. (2014). Study of design parameters of flapping-wings. *In International Micro Air Vehicle Conference and Flight Competition (IMAV2014)*. Delft, The Netherlands.

2. **Wang, Q.**, Goosen, J. F. L., & van Keulen, F. (2014). Optimal pitching axis of flapping-wings for hovering flight. *In The 4th international conference on engineering optimization (EngOpt2014)*. Lisbon, Portugal.

3. **Wang, Q.**, Goosen, J. F. L., & van Keulen, F. (2013). Optimal hovering kinematics with respect to various flapping-wing shapes. *In International Micro Air Vehicle Conference and Flight Competition (IMAV2013)*. Toulouse, France.

4. Goosen, J. F. L., Peters, H. J., **Wang, Q.**, Tiso, P., & van Keulen, F. (2013). Resonance based flapping wing micro air vehicle. *In International Micro Air Vehicle Conference and Flight Competition (IMAV2013)*. Toulouse, France.

ACKNOWLEDGEMENTS

To my family:

常言道："父母在，不远行。"十余年他乡漂泊让陪在父母身边的日子屈指可数，而电话那头他们的牵挂却从未间断。为人父方知父母不易。如今父母虽已年迈，却仍需为生计辛劳，作为儿子深感惭愧。谨以此文献给一直默默奉献的爸爸妈妈。同时，感谢哥哥和妹妹这么多年对整个家庭不懈的付出。

虽身处异国，我却未曾孤独。潘虹，因为有你，我们的小家虽然一直漂泊却始终温暖舒适；因为有你，我越来越从容，不管是面对现在还是将来；因为有你，才会有宝贝们梦中的笑容。王简和王羿，你们兄弟俩的到来，让生活每天都充满了惊喜，让我多了份永远的牵挂。

To my colleagues and friends:

I would like to give my thanks to Prof. *Zhenzhou Lü*, my master's thesis supervisor, and China scholarship council (CSC). I probably could not have the chance to experience such a surprising and fruitful four-year's life in Delft without the encouragement and support from Prof. *Lü* during the preparation for studying abroad and the sponsorship from CSC.

In September of 2012, I started my Ph. D. journey in the group of Structural Optimization and Mechanics (SOM) under the supervision of Prof. *Fred van Keulen* and Prof. *Hans Goosen*. In this journey, I had confusions, impatience and nervousness. However, most of the journal was accompanied by the enthusiasm, happiness and inspiration. More important, I received numerous patience, encouragement, guidance and scientific freedom from both *Fred* and *Hans*. Due to their quite distinct personalities, I learned different lessons from them. From *Fred*, I learned how rigorous and direct we should be as a scientific researcher, while I learned the strategies of solving problems in research and life from *Hans*. In addition, their solid and broad knowledge motivates me to keep learning for ever.

Undoubtedly, my Ph. D. can not be so impressive without the company of all the SOMers including *Alejandro, Alex, Banafsheh, Can, Deepak, Evert, Floris, Gijs, Jian Zhang, Laura, Long Wu, Marco, Matthijs, Max, Renato, Rob Dedden, Roy, Selman, Samee, Sanne, Sasan, Yabin Yang, Yi Zhang* and *Yong Zhang*. Particularly, the close cooperation with *Hugo* on the Atalanta project is a very valuable experience. I am also very lucky to have chance to work with so many nice and brilliant colleagues like *Anil, Hassan, Ivan, Just, Kai Wu, Marcel, Minchang Wang, Murali, Paolo, Paul, Rob Eling, Ruijun Deng, Shouen Zhu, Stijn, Sufang Fu, Urs* and Yueting Liu. The supports from secretaries and technical staff, including *Birgit, Corinne, Eveline, Gaby, Harry, Lisette, Jos, Marianne, Marli, Patrick* and *Rob Luttjeboer*, are very important for me to work efficiently and finish this thesis. I appreciate the inspiring discussions or cooperations with *Florian* from WUR, *Gih-Keong Lau* from NTU, *Mao Sun* from BUAA, *Mustafa* and *Shuanghou Deng* from TU Delft, *Wei-Bang Tay* from NUS and *Yanhai Nan* from ULB. I would like to express my deep gratitude to all of you. I also want to give my special thanks to *Lex* from DevLab for

his unique feedbacks during Atalanta meetings and his coordination of developing the experiment setup.

I will never forget the wonderful time when *Likun Ma, Lin Liu* and *Guoguo* were living upstairs. I feel so lucky to have this precious experience and friendship in my life. I would also like to give my sincere thanks to *Guiming Song, Jan Fienieg, Jun Zhang, Peng Lu, Saulo Meirelles, Wuyuan Zhang, Xin Wang, Xu Huang, Yuan Yang* and their families as well. They have brought numerous happiness to my family, which made the life abroad much easier. Thanks are also extended to *Bo Hou, Feifei Wang, Guangming Chen, Peijian Lü, Tao Lü, Weichen Mao, Xi Zhang, Xuezhou Wang, Yageng Li, Yannian Yang, Ye Zhang,* and *Zilong Wei* for their friendship during the stay in the Netherlands.

Qi Wang (王奇)
February 2017 in Delft